UNIVERSITA' DEGLI STUDI DI SALERNO

*Dipartimento di Fisica "E. R. Caianiello"*

**Scuola Dottorale in Scienze Matematiche, Fisiche, Naturali**

**Corso di Dottorato in Fisica**
**XIV Ciclo**

# A study on iron-chalcogenides superconductors: from samples preparation to physical properties

*Chiarasole Fiamozzi Zignani*

Coordinator: Prof. Canio Noce

Tutor: Prof. Sandro Pace

Co-tutor: Dr. Gaia Grimaldi

Gennaio 2017

*To my Family*

*Amicus Socrates, sed magis amica veritas (Plato)*

I modelli scientifici non sono veri, ed è proprio questo che li rende utili. Essi raccontano storie semplici che le nostre menti possono afferrare. Sono bugie per bambini, storie semplificate per insegnare, e non c'è nulla di male. Il progresso della scienza consiste nel raccontare bugie sempre più convincenti a bambini sempre più sofisticati (Sir Terry Pratchett)

La scienza non ha patria (Louis Pasteur)

# Abstract

In the scientific community there is a great interest to explore new superconducting materials suitable for high field applications in order to meet the needs of industrial claims. In this framework, newly discovered Fe-Based Superconductors (IBSC) are a promising choice, especially due to their critical temperature intermediate between low and high $T_c$ materials, as well as an extremely high upper critical field.
The aim of this work has been the preparation and the study of physical properties of iron-chalcogenides superconducting samples, in particular polycrystalline FeSe and FeSeTe. The iron-chalcogenides family has been choosen mostly because of its interesting superconducting properties and also due to its simple crystalline structure and to the lack of poisonous elements in its composition.

Opening a completely new research field at the ENEA CR Frascati, several routes of samples production have been carried out. I achieved part of the necessary know-how working also in other laboratories that have great experience on iron-based superconductors preparation, in particular the National Institute for Materials Science (NIMS) laboratories of Tsukuba in Japan, where I worked at the Nano Frontier Materials Group, under the leadership of Prof. Dr. Takano. I also had the chance to spend a brief period at the laboratories of CNR SPIN Genova and the Physics and Chemistry Departments at University of Genova, where I could meet researchers skilled in the production of iron-based samples. Most of the know-how was achieved by direct experience. Even if some of the routes for samples preparation did not brought to the expected results, some of these techniques gave interesting results, other routes deserve further optimization.
Concerning the FeSe compound, two preparation processes have been implemented: the electrochemical deposition on iron substrate, and the solid state reactive synthesis. The former gave FeSe thin films containing the right tetragonal $\beta$-phase, but the optimization of the superconducting properties in these samples would be very challenging and time-consuming. The solid state reactive sintering lead to the preparation of superconducting samples with good $T_c$ onset but containing several impurities, which compromised the steepness of transition and the current carrying capability. This route requires further optimization, which can be achieved keeping cleaner all the process steps.

Three routes were implemented for the preparation of FeSeTe samples, the solid state reactive synthesis, the mechano-chemical synthesis and the synthesis by fusion. The first two routes, as happened for FeSe samples, need further optimization.
The third route brought to the preparation of several very good polycrystalline samples by a melting process, with heat treatment (HT) at temperatures of about 970 °C followed by cooldown to about 400 °C. It was verified that, as a consequence of the fusion process, impurities and spurious phases between grains are mostly removed, a preferential orientation of the samples is promoted and the critical current is enhanced. Therefore this fabrication route is recommended in view of applications, even if further efforts are needed to develop the material ready to use for example as a target for films deposition or eventually for the preparation of actual strands.
In this work the main physical characterizations performed on all kinds of produced samples are shown. The reproducibility of the superconducting properties of samples

prepared with the same procedure has been verified and only the representative samples for each group have been shown for clarity and readability.
In particular the performing samples have been object of an extensive characterization, carried out in different superconducting labs at ENEA CR Frascati, at Master lab of CNR-SPIN Salerno and Physics Department of University of Salerno. Beside structural, magnetic, transport and calorimetric measurements, several analysis concerning the pinning mechanisms acting and competing inside the produced samples have been performed, within the framework of several literature models. As expected, pinning properties strongly depend on the preparation procedures which induces the defect structure into the samples. Magnetic relaxation measurements have supported this analysis, giving a corroborating possible interpretation of the measured peak effect, if present, and to the behaviour of the effective energy barrier as a function of the current density.
In conclusion, despite the undeniable polycrystalline nature of the FeSeTe samples, those obtained by melting process present superconducting properties closely resembling the single crystals ones, with onset temperatures of about 15 K and quite steep transitions. Best performing samples have large hysteresis cycles well opened up to 12 T (at about 9 K) and up to 18 T (at about 7 K) with a robust critical current density weakly dependent on the applied field in the high field range.

# Contents

# Introduction

The scientific community got surprised when in 2006 a new completely different family of superconductors was discovered by the group of Hideo Hosono. The Japanese group reported observation of a superconducting transition in LaFePO at a relatively low temperature of ~4 K. This original discovery received a limited attention from the community. The general excitement came 2 years later, when the same group reported superconductivity at a temperature of 26 K, higher than that of most conventional superconductors, in a closely related compound $LaFeAsO_{1-x}F_x$ at a doping level of $x = 0.12$ [1],[2] with the parent compound LaFeAsO being non-superconducting at routinely attainable cryogenic temperatures. This latter discovery gave rise to the explosive growth of research on these materials all over the world, which led to discovery of superconductivity in several new classes of compounds such as for example $SmFeAsO_{0.9}F_{0.1}$ [3] ($T_c \approx 55$ K) and $Ba_{0.6}K_{0.4}Fe_2As_2$ [4] ($T_c \approx 38$ K).

In short time many other Fe-based superconductors families were discovered, characterized by different layered structure, but always with Fe planes as constituting elements. In few months, by changing the way of doping or by applying external pressure, $T_c$ has raised up to 55K in $SmFeAsO_{0.8}F_{0.20}$, which still remains the upper limit for this class of compounds.

The scientific impact of the discovery of superconductivity in iron-based materials has been remarkable, with more than 500 theoretical and 2000 experimental papers published or posted on the preprint server arXiv in little more than two years. Among these publications, in July 2008 Hsu *et al*. reported superconductivity in the anti-PbO type FeSe at 8K [9], quickly followed by the reports of $FeTe_{1-x}Se_x$ ($T_c$ ~ 14 K) by Fang *et al*. [10] on 30$^{th}$ July 2008 and of $FeTe_{1-x}S_x$ ($T_c$ ~10 K) [11].

These compounds belong to the "11" family which is, from the structural point of view, the simplest family among Fe-based superconductors, on which the work of this thesis is focused. Since its discovery, the family of iron chalcogenides attracted much attention both from theorists and experimentalists, thanks to its simple crystal structure, which makes it apparently simpler to study. Moreover, these systems do not contain As, and then the compounds can be synthesized and handled more safely.

Working at the ENEA CR Frascati, in the Superconductivity Labs, the interest for superconducting materials which have high performances in high magnetic fields is continuously present, especially for cables and magnet applications. In this context the discovery of a new class of superconductors pushes the research activities to be more active in the production field too. Therefore the fabrication and the study of the superconducting performances in iron-based materials started with this thesis.

The purpose of this thesis has been the comparison of transport and magnetic properties among samples produced by several fabrication techniques with the aim of obtaining a scalable route for potential applications.

In particular my activity has been focused on:

- the fabrication of superconducting samples belonging to the iron-based "11" family with several techniques (electrochemical deposition, solid state reactive sintering, mechano-chemical synthesis and melting processes),

- structural and electrical characterization of the produced samples in order to evidence the presence of the right superconducting phase,
- a deeper investigation of the main superconducting properties on the best performing samples in order to study their critical fields, critical current densities and pinning properties and to correlate the superconducting properties with the structural characterizations and the fabrication processes.

Among the different explored fabrication routes, some led to very interesting results, in terms of superconducting properties of the produced samples and also in term of their structural and compositional properties.

This thesis is organized as follows:

In the first Chapter the scientific and technological interest of these materials will be pointed out. Moreover the first Chapter is a review of the state of the art, and presents an introduction on the superconducting Fe-based compounds. An overview of the structural, magnetic and electronic properties and of the materials preparations techniques for the different families is given and their phase diagram is introduced, giving particular emphasis to the "11" family of the iron based-chalcogenides. Superconducting properties relevant for applications are discussed, also in comparison with conventional and other unconventional superconductors.

The second Chapter describes the fabrication techniques developed during the thesis for the production of iron-chalcogenides superconducting samples. The fabrication routes undertaken during the thesis and described here are: the electrochemical deposition of FeSe on iron substrate, the solid state synthesis of FeSe and FeSeTe at several temperatures, the mechano-chemical synthesis of FeSeTe samples and the synthesis by fusion of precursors powders. At the end of this Chapter, I will briefly describe the measurement systems that have been used for samples characterizations. In view of the selection of a fabrication route suitable for applications, the difficulties encountered in the fabrication processes during the work are to be considered, as well as the complexity of the procedure adopted in order to obtain the best performing samples.

In the third Chapter the results obtained for the structural and the superconducting characterization of FeSe samples produced by electrochemical synthesis and solid state reaction are described and commented.

In Chapter 4 the results obtained for FeSeTe samples obtained with three different synthesis techniques are described. Samples have been characterized by their structural and superconducting properties and the best performing ones have been deeply studied in order to understand and evaluate their pinning properties from the analysis of transport, magnetic and calorimetric measurements.

After presenting Conclusions, in Appendix 1 some details on High Energy Ball Milling (HEBM) are given.

CHAPTER 1

# High temperature superconductivity in iron-based materials

Iron is the archetypal ferromagnet and, before 2006, has never been supposed to be compatible with superconductivity. Its locally polarized spins, all pointing in the same direction, create a magnetic field that would wring apart all Cooper pairs that are trying to form. It therefore came as a surprise when, in Febbruary 2008, Hideo Hosono of the Tokyo Institute of Technology published the discovery of a superconductor containing iron: the fluorine-doped LaFeAsO with critical temperature $T_c$=26 K [1]. The exciting discovery of the FeAs based new superconductors with maximum $T_c$ as high as 55 K [1]-[4] has opened a new chapter in the fields of high temperature superconductivity and magnetism. These new superconductors can be described by the general formula *RE*OTmPn, where *RE* is a rare earth element (such as La, Ce, Pr, Sm, Eu, Gd), Tm a transition metal and Pn = P or As. As based compounds exhibit $T_c$ higher than P based systems. The $T_c$ is controlled by the size of the *RE* ion, by the electron doping and either by F substitution in the O sites [1], oxygen deficiency [5] or by hole doping as in the $La_{1-x}Sr_xOFeAs$ [6].

After these discoveries, related to the so called 1111 "family", many researchers have been interested in these iron-pnictide superconductors and owing to a strong competitive research activities, new iron-based superconductors (IBSC) with different crystal structures, such as $(Ba,K)Fe_2As_2$ [7] (122family), LiFeAs [8] (111 family) and $FeSe_{1-x}$ [9]-[11] (11 family) have been discovered within a short period. These materials are classified based on their crystallographic structure and the classes are usually denoted by the chemical formula of the parent compound, often non-superconducting (e.g. 1111 for the parent compounds *RE*FeAsO, or 122 for $BaFe_2As_2$). In the last 8 years, more than 15,000 papers have been published as a result of intensive research on this materials [12],[13]. New iron-based superconducting families and compounds are regularly discovered, such as for example the 112 compounds (Ca, *RE*)$FeAs_2$ with $T_c$ up to ~ 40 K [14],[15], the 42 214 compounds $RE_4Fe_2As_2Te_{1-x}O_4$ with $T_c$ up to ~ 45 K for *RE*=Gd [16],[17], the 21 311 compounds $Sr_2MO_3FeAs$ (M= Sc, V, Cr) with $T_c$ ~37 K [18] and [(Li, Fe)OH]FeSe with $T_c$ up to ~ 40 K [19]. One of the exciting aspects of these new superconductors is that they belong to a comprehensive class of materials where many chemical substitutions are possible. The only problem working with IBSC is the trickier chemistry of the compound and the toxicity and volatility of arsenic.

Differences and similarities are apparent between IBSC and the established exemplars of high $T_c$-superconductivity (HTS), the cuprates. LaFeAsO and the parent compounds of the other subsequently discovered families, all belong to the class of poor conductors known as semimetals; the cuprates' parents are insulators. IBSC share several characteristics with the cuprate superconductors, such as layered structure, the presence of competing orders, low carrier density, small coherence length and unconventional pairing, all of which potentially hinder practical applications, especially due to their influence in exciting large thermal fluctuations and depressed grain boundary superconductivity. On the more positive side, however,

the Fe-based superconductors have metallic parent compounds, their anisotropy is generally smaller and does not strongly depend on the level of doping, and their generally supposed order parameter symmetry is s-wave, which is in principle not so detrimental to current transport across grain boundaries [20],[21],[22].

Antiferromagnetism, or, rather, the weakening of antiferromagnetic order, appears to play a key role in their superconductivity, which is mediated by electron-electron interactions, most likely spin fluctuations. These superconductors captivated, and are still captivating, theorist and experiments alike. The existing challenges, such as optimizing synthesis methods for technological applications, clarifying the ambiguity in the superconducting mechanism and the flexibility of the material for any site substitution, will keep IBSC on the frontiers of research for a long time, in parallel to HTS [23].

In this Chapter of the thesis a work of review has been done, to present a summary on the key properties of the Fe-based superconductors and related compounds. Since the topic of this thesis relates with 11 family, after an initial description of all families, I will enter in more details with the 11 family, its properties and the state of the art regarding the samples described in literature. I will also discuss the reasons why IBSC in general and iron-chalcogenides in particular are promising due to their appealing properties relevant for applications. IBSC have in fact several unique properties such as robustness to impurity, high upper critical field and promising grain boundary nature. These properties are potentially advantageous for wire and film application [20].

## 1.1 Crystal structure

Iron, one of the most common metals on earth, has been known as a useful element since the aptly named Iron Age. However, it was not until recently that, when combined with elements from the group 15 and 16 of the periodic table, named, respectively, pnictogens (*Pn*), and chalcogens (*Ch*), iron-based metals were shown to be protagonists of a new form of high-temperature superconductivity. This general family of materials has quickly grown in size, with well over 50 different compounds identified. So far, several crystallographic structures have been shown to support superconductivity. As shown in Figure 1, these structures all possess tetragonal symmetry at room temperature, and range from the simplest PbO-type binary element structure to more complicated quinternary structures composed of elements that span the entire periodic table [25]. Superconductivity takes place in a corrugate layer made up of Fe and one of two *Pn* (phosphorus, arsenic) or one of the two *Ch* (selenium, tellurium).

The different families incorporate this corrugated layer with a characteristically different interlayer. In the 1111 family, for example, the interlayer consists of a rare earth an oxygen; in the 122 family of an alkaline earth and in the 111 family of an alkali. There is no interlayer in the 11 family, and to preserve the layer's charge balance the pnictogen is replaced by a chalcogen [21]. This layered structure reminds that of HTS, and the terminology related is clearly a reminiscence of that commonly used in cuprates where high mobility and conducting $CuO_2$ planes are alternated with the so called "charge reservoir" layers. In IBSC the iron containing layer is not flat; *Pn* or *Ch* atoms protrude above and below the plane. Because the *Pn* and the *Ch* atoms are much larger than Fe atoms, they pack themselves in edge-sharing tetrahedral. By contrast, the smaller size difference between the copper and oxygen

atoms in a cuprate superconductor leads to corner-sharing octahedral packing. That structural difference is crucial. Thanks to their tetrahedral configuration, the Fe atoms in an IBSC are closer to each other than the Cu atoms are in a cuprate superconductor. Both Fe and Cu occupy the same row of the periodic table and their valence electron occupy 3*d* orbitals. But because of the Fe atoms' closer packing, all five Fe 3*d* orbitals contribute charge carriers, while in the cuprate only one Cu 3*d* orbital contributes [21].

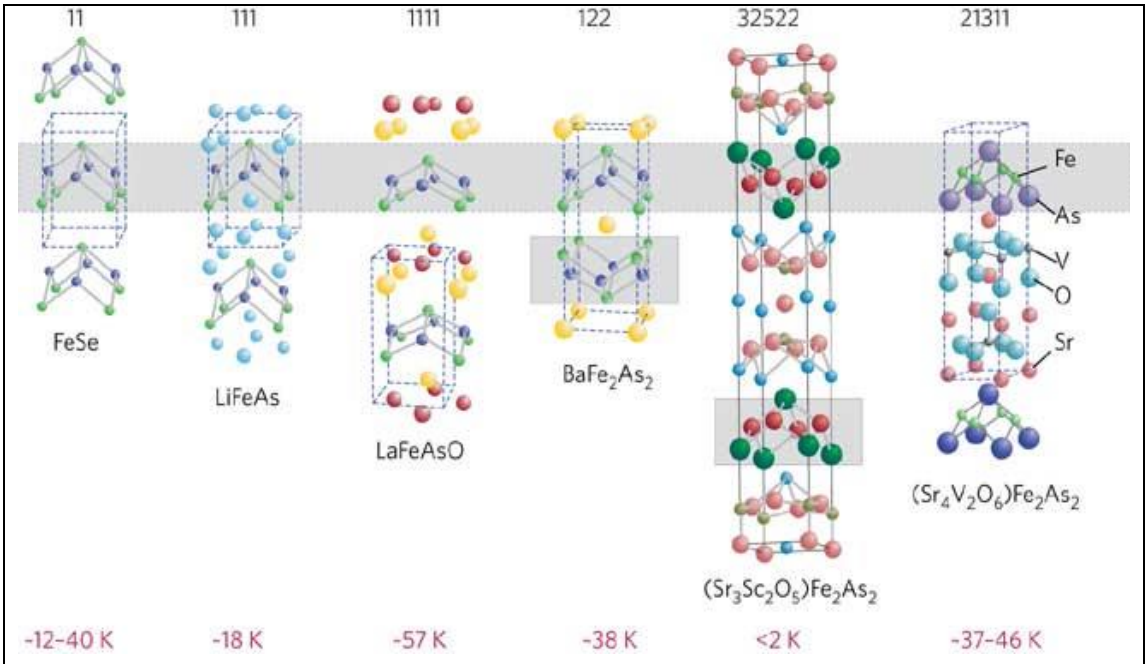


Figure 1: Six phases of iron-based pnictides and chalcogenides. Listed below each structure is the highest achieved $T_c$ [20]

IBSC and cuprates are different also in another aspect, that is chemical substitution. In the 1111 family, for example, dopants can be inserted at any of the four ionic positions, even into the iron layer. By contrast, chemical manipulation of the copper layer in the cuprates proved severely detrimental to their superconductivity.
In the iron-pnictides materials, the common FeAs building block is considered a critical component to stabilizing superconductivity. Because of the combination of strong bonding between Fe-Fe and Fe-As sites (and even interlayer As-As in the 122-type systems), the geometry of the $FeAs_4$ tetrahedra plays a crucial role in determining the electronic and magnetic properties of these systems. For instance, the two As-Fe-As tetrahedral bond angles seem to play a crucial role in optimizing the superconducting transition temperature, with the highest $T_c$ values found only when this geometry is closest to the ideal value of 109.47° [25]-[26].

## 1.2 Electronic structure

A lot of work has been done to determine the magnetic and electronic structures of these materials, as the interplay of magnetic and electronic interactions probably plays an integral role in determining the shape of the phase diagram of all IBSC systems. The connection between structural details of IBSC materials and their seemingly

sensitive electronics is important and has significant implications, both theoretically and in practical terms: a close relationship between structure and superconductivity, direct or indirect, places constraints on both the theoretical understanding of the pairing interaction and the promise of superconductors with higher $T_c$ values.
The electronic band structure has been calculated using the local density approximation [28], showing that the electronic properties are dominated by five Fe *d* states at the Fermi energy ($E_F$), with a Fermi surface (FS) consisting of at least four quasi-2D electron and hole cylinders. The dominant contribution to the electronic density of states at $E_F$ derives from metallic bonding of the iron *d*-electron orbitals in the iron-pnictogen (or chalcogen) layer. These form several bands that cross $E_F$, both electron- and hole-like, resulting in a multiband system dominated by iron *d* character.
The most direct way to determine the Fermi surface of a compound is by means of angle-resolved photoemission spectroscopy (ARPES). By detecting emitted electrons with the energy equal to the Fermi energy, synchrotron-based ARPES is capable of mapping the Fermi surface in the entire Brillouin zone. When carried out in the superconducting state, ARPES measurements provide detailed information about the momentum-dependence of the superconducting gap on all Fermi surfaces where it can be resolved (the ultimate resolution limit is instrument-dependent, with the state-of-the-art experiments discerning superconducting gaps as small as 3 meV). When sufficiently clean single-crystalline materials are available, the Fermi surface can also be probed by various quantum oscillation (QO) measurements [29]. The qualitative agreement between calculations and experiments is remarkably good, as shown by several ARPES and QO measurements [30]-[34]. Instabilities of this electronic structure to both magnetic ordering and superconducting pairing are widely believed to be at the heart of the exotic properties of the iron-based superconducting materials [25].

## 1.3 Magnetic properties, phase diagram and pairing symmetry

The nature of magnetism in the IBSC parent compounds is a hotly debated topic, largely owing to its implications for the pairing mechanism: the electronic structure suggests that the same magnetic interactions that drive the antiferromagnetic (AFM) ordering also produce the pairing interaction for superconductivity [35]. Regardless of the exact nature of magnetic order, it is clear that magnetostructural coupling in the IBSC family has the prevalent form of coupled magnetic and structural transitions. This is generally understood to be driven by magnetic interactions [28],[36]. However, a peculiarity of the coupled transitions is that, aside from the case of the 122-type parent compounds where Neel Temperature ($T_N$) and structural transition temperature ($T_0$) coincide exactly, the structural and magnetic phase transitions are positioned at different temperatures in 1111-type compounds, with the structural transition actually preceding the magnetic transition [37], [25].
Since the Fermi level of each parent compound is primarily governed by Fe five 3*d*-orbitals, iron plays the central role in superconductivity. These compounds have tetragonal symmetry in the superconducting phase, are Pauli para-metals in the normal state and undergo crystallographic/magnetic transition to orthorhombic or monoclinic anti-ferromagnetism at low temperatures. Exception is a 111-type compound with Pauli paramagnetism even at lower temperature [24].

Although the antiferromagnetic phases are quite different in the cuprates and pnictides, one thing is common: the antiferromagnetic and superconducting order parameters appear to compete in their fully ordered forms, but superconductivity is strongest where the antiferromagnetic long-range order has just disappeared completely. In IBSC superconductivity in fact emerges when anti-ferromagnetism disappears or diminishes thanks to carrier doping or structural modification, by applying external pressure or by chemical pressure induced by isovalent substitution. This suggests that, although superconductivity is destroyed by long-range antiferromagnetic order, it is driven by the fluctuations of electron spins, which are strongest (but already weak enough not to give rise to the competing long-range order) at the border with the antiferromagnetic phase. A large body of experimental data strongly supports this conclusion [38]-[41].
In any case, the parent materials are metals having itinerant carriers and the ways to remove the obstacles for emergence of superconductivity were found with experimental approach. Most of the parent materials are anti-ferromagnetic metal, and superconductivity is induced by appropriate carrier doping or structural modification. Although some of the parent phases exhibit superconductivity without doping, the $T_c$ value of such a material is low, as exemplified by LaFePO [2] with $T_c$ = 4 K, implying the occurrence of close relationship between magnetic ordering in the parent phase and resulting $T_c$.

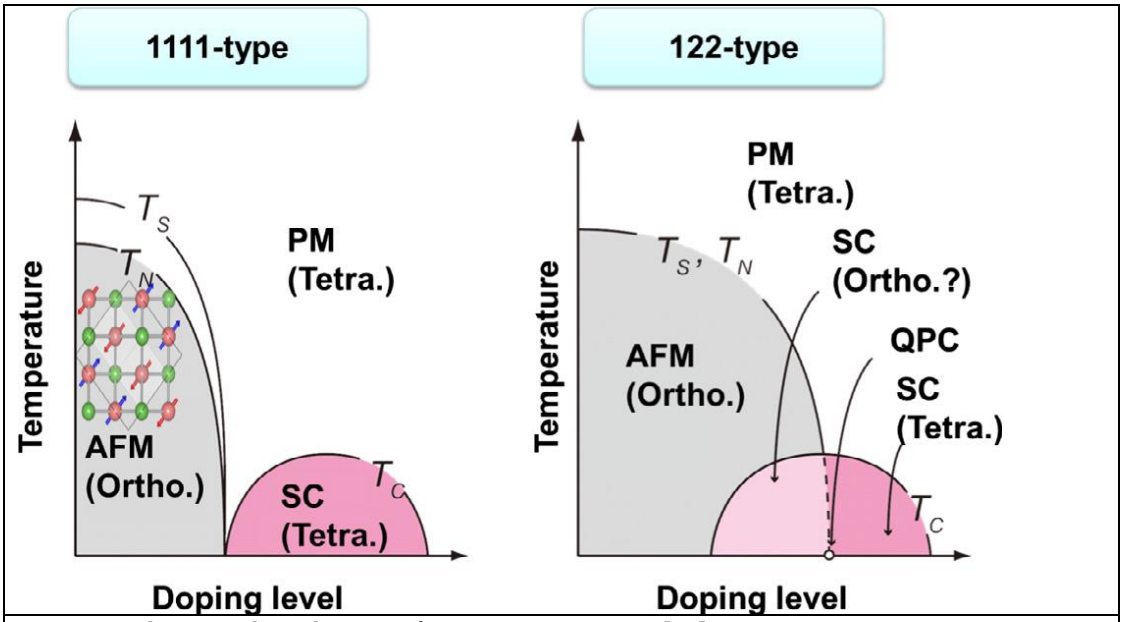


Figure 2: Schematic phase diagram of representative IBSCs [24].

Figure 2 shows the schematic phase diagram of the 1111 and 122 system. For the 1111 system, the $T_c$ appears when the anti-ferromagnetism (AFM) disappears. On the other hand, the AFM and superconductivity coexist in the 122 system and the optimal $T_c$ appears to be obtained at a doping level where $T_N$ reached 0 K, suggesting the close relationship between the optimal $T_c$ and quantum criticality. Electron doping into *RE*-1111 compounds (where *RE* = rare earth metal) by this substitution was very successful, i.e., the maximum $T_c$ was increased from 26 K to 55 K by replacing La with other *RE* ion with smaller ionic radius [42], [24].

As for the high-$T_c$ cuprates, for IBSCs as well the experimental evidence so far favours an unconventional pairing mechanism closely tied to magnetism. Although the exact nature of the pairing is not known in either system at present, many experiments aimed to determine the pairing symmetry have been carried out.
For the cuprates, the experimental evidence favours a singlet *d*-wave symmetry that involves a change in sign of the superconducting order parameter (OP) phase at nodal points situated at the Fermi energy ($E_F$) and directed along ($\pi$; $\pi$) in the simple 2D cuprate band structure.
For the IBSCs, the initial measurements, [43] probing the OP symmetry pointed to a fully gapped OP, consistent with a fully symmetric s-wave symmetry. In comparison to cuprates and other magnetically mediated superconductors, this came as a surprise. However, the OP symmetry of IBSCs was in fact predicted theoretically to have s-wave symmetry, but with a sign change that occurs between different bands in the complex multiband electronic structure. This is the so-called *s* ± state [44],[25]. The mechanism of superconductivity in the IBSC is under debate, and it has been shown theoretically that the electron–phonon coupling in these compounds is very weak and thus unable to account for the observed high superconducting transition temperatures [45]. On the other hand, theoretical treatment has shown that spin fluctuations can, in principle, lead to an *effective* attractive interaction between itinerant electrons and thus to their pairing and the formation of a superconducting condensate [46].
A large body of experimental data obtained on compounds from both the cuprate and the iron-pnictide family of superconductors strongly supports this mechanism of superconductivity [39]–[41],[47], making spin fluctuations the most plausible candidate for the so-called 'superconducting pairing glue' or 'mediating boson'. In contrast, recent experimental results showed that high $T_c$ is revealed when the nesting is degraded, or even in the absence of the nesting by heavy doping of impurities [48]-[52],[53]. The theoretical and experimental evaluation for the superconducting mechanism will of course continue.

## 1.4 Materials preparation in literature

The synthesis methods in general can roughly be divided into several groups: solid state reaction method, high pressure synthesis method, flux method and chemical methods. Solid state reactions yielded polycrystalline samples of all types of IBSC and its parents compounds. This method can be considered the most reasonable one in order to obtain larger or even industrial-scale amounts of substances. Nevertheless the large experience in the synthesis of pnictide compounds [54],[55], the relevant phase diagrams are mostly unknown and the synthesis conditions were optimized by trial and error. Thus the production of homogeneous superconducting samples without contamination with foreign phases has been a challenge for years after the discovery of IBSC and still is. Solid state reaction require elevated temperature up to 1200°C and inert conditions regarding the gas atmosphere and the containing materials. The synthesis procedures for transition metal pnictides and chalcogenides are very different from those widely used for copper oxides, due to the much higher fugacity of pnictide atoms at higher temperatures [12].

High pressure method is more efficient than the ambient pressure (solid state) method for the synthesis of gas releasing compounds, for which drastically improves the superconducting transition temperature. High pressure stabilize the superconducting phase at higher temperature than in the quartz ampoule technique and therefore it

allows to use higher temperature for single crystal growth. In the case of polycrystalline samples high pressure leads to strongly sintered samples with better intergrain connections. The application of high pressure for volatile components prevents evaporation and losses of components. It is not negligible to mention that the high pressure anvil technique is relatively safe, because the sample is confined in a closed container supported by anvils, while with the ampoule techniques explosions of ampoules may lead to a contamination of the laboratory with poisonous elements if safety rules are not applied strictly [12].

Large single crystal of high quality are of fundamental importance to determine the intrinsic properties of the IBSC and allow essential experiments in order to decipher the pairing mechanism (e.g. ARPES). Metal fluxes have been used at the very beginning for the fabrication of large crystals, especially of 122 family [56]. However these large crystals, quickly obtained from tin fluxes, proved to be of very poor quality and contained inclusions of tin metal, which strongly affected their properties [57]. Cleaner crystals grow in fluxes of binary FeAs, which melts around 100°C. This so called "self-flux" method is especially useful for transition-metal doping of 122-compounds [58]. On the other hand, metal flux methods are unsuitable for oxygen-containing 1111-type superconductors, where still rather tiny crystals were obtained from salt fluxes under high pressure conditions [59].

## 1.5 Superconducting properties and application potential

IBSCs, with their very high upper critical fields, relatively low anisotropy and large $J_c$ values, which are only weakly reduced by magnetic fields at low temperatures, suggest considerable potential in large scale applications, particularly at low temperature and high fields [22]. In Table 1-I the main properties of IBSC together with those of YBCO and conventional superconductors are summarized. Large values of the upper critical field $B_{c2}$ for IBSC, correspond to a small coherence length in the *ab* plane ($\xi_{ab}$), of the order of a few nm. The $B_{c2}$ anisotropy $\gamma_H$, defined as $B_{c2}^{\parallel ab} / B_{c2}^{\perp ab}$ in IBSC is particularly affected by the different temperature dependences in the two directions. While it is almost constant and equal to 5 in Nd-1111, in Fe-11 is about 2 close to $T_c$ and drops rapidly to 1 at the lower temperatures. The Ginzburg number $G_i$ quantifies the temperature region $G_iT_c$ where the fluctuations are significant. It is expressed by [22], [51] $G_i = (\pi \lambda_0^2 k_B T_c \mu_0 / 2\xi_c \Phi_0^2)^2$, where $\lambda_0$ is the London penetration depth, $k_B$ is the Boltzman constant and $\Phi_0$ is the flux quantum.

Thanks to the small coherence length of a few nanometers, IBSCs are particularly sensitive to the inclusion of nanoparticles and to local variation of stoichiometry as pinning centers, to enhance the critical current density [60]. For example, the pinning force in 122 films has been enhanced above that of optimized $Nb_3Sn$ at 4.2 K by the introduction of self assembled $BaFeO_2$ nanorods [61], and similar effects were obtained due to local variations of stoichiometry in 11 films [62], [63], [64]. Critical current density ($J_c$) values exceeding $10^5$ A cm$^{-2}$ were measured in IBSCs films of 11, 122 and 1111 families up to very large magnetic fields either parallel or perpendicular to the Fe planes. In particular a $J_c$ above $10^5$ A cm$^{-2}$ was achieved up to 18 T in P-doped $BaFe_2As_2$ films [64], up to 30 T in $FeSe_{0.5}Te_{0.5}$ films [62] and up to 45 T in SmFeAs(O,F) films [65]. Record values of self-field critical current densities up to

6 MA cm$^{-2}$ at 4.2 K were measured in 122 films [64], [66] and up to 20 MA cm$^{-2}$ at 4.2 K in zero field in 1111 single crystals irradiated with heavy ions [67].

| | 1111 | 122 | 11 | YBCO | $MgB_2$ | $Nb_3Sn$ |
|---|---|---|---|---|---|---|
| $T_c$ (K) | 55 | 38 | 16 | 93 | 39 | 18 |
| $B_{c20}$ (T) | >50 | 60 | 55 | >50 | 20-30 | 30 |
| $\xi_{ab}$ (nm) | 2.5 | 3 | 1.5 | 2.2 | 10 | 3 |
| $\gamma_H$ | 5 | 2 | 2-3 | 4-14 | 3-5 | 1 |
| $\lambda_{ab}$ (nm) | 200 | 200 | 490 | 180 | 50-100 | 60 |
| Ginzburg number $G_i$ | $4*10^{-4}$ | $2*10^{-5}$ | $1*10^{-3}$ | $>10^{-3}$ | $<10^{-5}$ | $<10^{-5}$ |
| pairing | Not BCS | Not BCS | Not BCS | Not BCS | BCS | BCS |

Table 1-I: comparison among significant superconducting properties of three IBSC families, YBCO, $MgB_2$ and $Nb_3Sn$.

### 1.5.1 superconducting properties

The performance limit of a superconducting material is defined in terms of temperature, field and critical current. The critical transition temperature, $T_c$, is defined as the temperature up to which superconductivity persists. Applications are anyway restricted to lower temperatures, since superconductivity becomes very weak close to $T_c$. In Table 1-II relevant iron-based compounds and technical superconductors are compared. Generally, the operation temperature ($T_{op}$) is considered about half of $T_c$ or even lower in applications requiring high currents and/or fields. Moreover, strong thermal fluctuations of the vortex lattice reduce the critical currents significantly in highly anisotropic materials, restricting appropriate operation conditions to much lower temperatures. $(Bi,Pb)_2Sr_2Ca_1Cu_2O_x$ (Bi-2212) is an extreme example of superconductor that provides useful current densities only at temperatures below about 20 K, despite its high transition temperature of 85 K [60].

| Compound | Code | max. $T_c$ (K) | $T_{op}$ (K) | |
|---|---|---|---|---|
| $LnFeAsO_{1-x}F_x$ | 1111 | 58 | ≤40 (?) | Ln=Sm, Nd, La, Pr,K. |
| $BaFe_2As_2$ a | 122 | 38 | ≤25 | K, Co, or P doping |
| $FeSe_{1-x}Te_x$ | 11 | 16 | ≤4.2 | |
| Nb-Ti | — | 10 | ≤4.2 | |
| $Nb_3Sn$ | — | 18 | ≤4.2 | |
| $MgB_2$ | — | 39 | ≤25 | |
| RE-$Ba_2Cu_3O_{7-x}$ | RE-123 | 95 | ≤77 | *RE*=Y,Gd, Sm, Nd, Yb,K |
| $Bi_2Sr_2CaCu_2O_{8-x}$ | Bi-2212 | 85 | ≤20 | |
| $Bi_2Sr_2Ca_2Cu_3O_{10-x}$ | Bi-2223 | 110 | ≤77 | |

Table 1-II: Relevant iron-based compounds and technical superconductors. The highest $T_c$ found in each family is given together with $T_{op}$, which refers to the expected operation temperature [60],[68], [4],[10].

All IBSCs discovered so far are obviously not alternative to $REBa_2Cu_3O_7$ (RE-123) coated conductors or $(Bi,Pb)_2Sr_2Ca_2Cu_3O_x$ (Bi-2223) tapes at high temperature (>50 K), in particular for use with nitrogen as the coolant.

Considering a superconductor with an upper critical field $B_{c2}$, usually a field of about 0.75 ·$B_{c2}$ can be effectively achieved in application. Since superconducting wires are used nowadays almost exclusively for magnets, $B_{c2}$ is certainly a key parameter for applications. Magnets based on conventional (niobium- based) technology can be used only up to fields below 25 T, so novel conductors for the next generation of Nuclear Magnetic Resonance (NMR), accelerator, research, and fusion magnets are needed. An important point to underline is the low anisotropy of the upper critical field $B_{c2}$ (ab)/$B_{c2}$ (c) in the IBSCs, which makes flux pinning more efficient than in the highly anisotropic cuprates. In particular, the 11 and 122 families are nearly isotropic at low temperatures [22], [69] and also close to $T_c$ the anisotropy remains well below that of RE-123 coated conductors (≈5) and Bi-tapes (>20) [60].
The critical current density in a superconducting wire is limited both by flux pinning and/or granularity. Flux pinning is an extrinsic property, and can be tuned by generating a suitable defect structure. The maximally achievable loss free currents are dependent from the basic material parameters.
In IBSC efficient pinning can be realized by irradiation [67],[70], by the successful introduction of nanoparticles [66] or nanorods [61],[71] and by the effect of local variation of stoichiometry [62],[63]. Moreover, irradiation with Au ions [72] and neutrons [73] and introduction of artificial *ab* plane pins [74] emphasized that the introduction of pinning defects does not affect $T_c$ appreciably. This indicates that IBSCs tolerate a high density of defects without a significant decrease in $T_c$, which makes them ideal candidates for high field applications, since the number of pinning centres is of crucial importance at high fields [60]. In IBSC not only $B_{c2}$ but also $J_c$ has small anisotropy with respect to the crystal axis. Direct transport measurements in the two main crystallographic directions carried out on Sm-1111 and $Ba(Fe_{1-x}Co_x)_2As_2$ single crystals showed that the ratio obtained for $J_c^{(ab)}/J_c^{(c)}$ ratios were 2.5 and 1.5 respectively [75],[76], much lower than the values of up to 10–50 found in the cuprates [77].
All high-$T_c$ superconductors are subjected to magnetic granularity which limits the macroscopic currents. In $MgB_2$ secondary phases at grain boundaries and voids reduce the cross section over which the current can flows, while in cuprates high angle grain boundaries intrinsically limit the currents in polycrystalline samples. For misalignment angles between adjacent grains above $\theta_c$~3°, $J_c$ drops exponentially [78]. The exponential decay of the current as a function of the misalignment angle between grains measured in IBSC is not as strong as in cuprates. The critical angle for $J_c$ suppression is $\theta_c$~9°, slightly larger than in cuprates, and the suppression itself is less severe, for example for $\theta$ varying from 0° to 24°, $J_c$ decreases by one order of magnitude in $Ba(Fe_{1-x}Co_x)_2As_2$ and by two orders of magnitude in $YBa_2Cu_3O_{7-x}$ [79], [80]. On the whole, the weak link problem seems less serious in IBSCs than in cuprates [81]. The mechanisms that limit current flow at the grain boundaries in IBSCs are still lacking a well-founded explanation. There are both intrinsic and extrinsic reasons: the larger critical angle $\theta_c$, possibly related to the higher robustness of the superconducting s-wave symmetry as compared to d-wave symmetry in cuprates and the metallic nature of underdoped phases that may be present at the grain boundaries, as compared to the insulating nature of cuprate parent compounds [60].

### 1.5.2 application potential

The fabrication of conductors for power applications has been explored since the very beginning of the research activity on IBSCs. The current state-of-the-art is not yet

mature enough to address the systematic fabrication of long length specimens. Anyway very encouraging results have been obtained on short samples fabricated both by the powder-in-tube (PIT) method and by processes which replicate the RE-123 coated conductor technology. The highest transport critical current in IBSC wires and tapes has so far been obtained with the 122 family, namely up to $10^4$–$10^5$ A cm$^{-2}$. Moreover, in 122 wires the $J_c$ field dependence is quite flat, with a decrease of one order of magnitude from a self-field to a field well above 10 T. For the 1111 family, the transport $J_c$ values found in wires and tapes prepared by *ex situ* PIT reach $3.45 \cdot 10^4$ A cm$^{-2}$ [82], but the field dependence of $J_c$ is steeper as compared to 122 wires and tapes [83]. Wires and tapes of the 11 compounds obtained by *in situ* PIT exhibit the lowest transport $J_c$ values, up to $3 \cdot 10^3$ A cm$^{-2}$ [84],[85], but they have the advantages of containing no toxic arsenic and having the simplest crystal structure. From the state-of-the art results, it can be envisaged that iron-based superconductor (122) wires and tapes are promising for magnet applications at 20–30 K, where the niobium-based superconductors cannot play a role owing to their lower $T_c$, and as $J_c$ is rapidly suppressed by the applied field in $MgB_2$ [60].

The application of the coated conductor technology to 122 thin films has been suggested to overcome the weak-link behaviour. For 122 films grown on Ion-beam assisted deposition (IBAD) substrates [86]–[89], in-plane misorientation of 3°–5° was measured and, most importantly, $J_c$ values of $10^5$–$10^6$ A cm$^{-2}$ were achieved. This route turned out to be encouraging for the 11 family as well. Fe(Se,Te) thin films deposited on IBAD-MgO-buffered Hastelloy substrates were able to carry transport critical current up to $2 \cdot 10^5$ A cm$^{-2}$ at low temperature and self-field, still as high as $10^4$ A cm$^{-2}$ at a field of 25 T [90]. Even more remarkable results were obtained for Fe(Se,Te) thin films deposited on RABiTS (rolling assisted biaxially textured substrates), i.e. critical currents up to $2 \cdot 10^6$ A cm$^{-2}$ at low temperature and self-field, still as high as $10^5$ A cm$^{-2}$ at a field of 30 T [62]. The fabrication of coated conductors with 1111 IBSCs was also attempted [91]. NdFeAs(O,F) thin films grown by molecular beam epitaxy on IBAD-MgO-$Y_2O_3$ Hastelloy substrates showed a high *c*-

| IBSC family | self-field $J_c$ (A cm$^{-2}$) | in-field $H_{\perp ab}$ $J_c$ (A cm$^{-2}$) | in-field $H_{\|\|ab}$ $J_c$ (A cm-2) | Type of measurement |
|---|---|---|---|---|
| 122 | $3.5 \cdot 10^6$ | $1.0 \cdot 10^5$ at $\mu_0 H_{\perp ab}$=10 T | $2.0 \cdot 10^5$ at $\mu_0 H_{\|\|ab}$=10 T | transport |
| 1111 | $7 \cdot 10^4$ | $5.0 \cdot 10^3$ at $\mu_0 H_{\perp ab}$=4 T | | magnetic |
| 11 | $2.0 \cdot 10^6$ | $9.0 \cdot 10^5$ at $\mu_0 H_{\perp ab}$=10 T | $1.0 \cdot 10^6$ at $\mu_0 H_{\|\|ab}$=10 T | transport |

Table 1-III: record values of IBSC coated conductors of different families, measured at low temperature (2.5–5 K) in self-field and high magnetic field, either parallel (H||ab) or perpendicular (H⊥ab) to the crystalline ab planes (Fe planes) [87],[91],[62],[60].

axis texture, but not complete in-plane texture. A magnetic $J_c$ of $7 \cdot 10^4$ A cm$^{-2}$ was measured in a self-field at 5 K, which is larger by one order of magnitude than the $J_c$ of 1111 PIT tapes, but significantly smaller than the $J_c$ of 122 and 11 coated conductors. [60]. Record data of $J_c$ values measured in coated conductors are reported in Table 1-III.

In Figure 3, $J_c$ versus field properties at 4.2 K for various IBSC films on single-crystal and IBAD–MgO-buffered metal substrates are compared with those for Nb–Ti and

$Nb_3Sn$ conductors. $Nb_3Sn$ exhibits a steep decrease of $J_c$ at fields near 20 T, which is close to its $H_{c2}$. The Ba-122:P film on MgO fabricated by an MBE method shows $J_c$ ($H$//$c$) over $10^5$ and $10^4$ A cm$^{-2}$ at 20 and 35 T, respectively. The Ba-122:P films with dense $c$-axis-correlated pinning centers [92] or $BaZrO_3$ nanoparticles [93] by a PLD method exhibit even higher $J_c$ values at fields below 9 T and a rather slow decay. The in-field performance of IBSCs, in particular Ba-122, can be remarkably improved by introduced nanometer-size vortex pinning centers, as already demonstrated in REBCO. Fe(Se,Te), films can be grown at lower substrate temperatures and coated conductors with $J_c$ over $10^5$ A cm$^{-2}$ at 30 T [62].
Of course, the development of IBSCs with less toxic elements would stimulate their application. Further continuing research and development is definitely required to realize practical wires or tapes based on IBSCs, discovered only eight years ago. The material variety of IBSCs is the largest among all the superconductor families, and the discovery of new types of superconducting materials has been continuing to date. The intrinsic nature of this materials system provides a wide opportunity in which various degrees of freedom can contribute to the emergence of superconductivity [94].

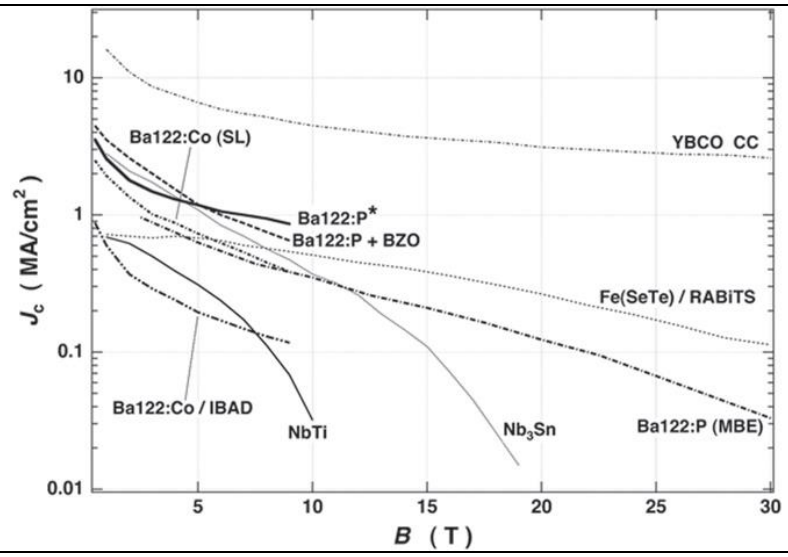


Figure 3. $J_c$ vs. $B$(//$c$) curves at 4.2 K reported for Ba-122 and Fe(Se,Te) films on single-crystal substrates and some technical substrates such as IBAD and RABiTS. The data of Nb–Ti and $Nb_3Sn$ commercial wires and YBCO coated conductors are also shown for comparison [92]-[94],[88],[62].

## 1.6 Iron chalcogenides superconductors

In principle, among the different IBSC families, the 122 compounds with a chemical composition of $AFe_2As_2$ (A = alkaline earth metal) appear to be the most promising. In fact they are the least anisotropic, have reduced thermal fluctuations, have a fairly large $T_c$ of up to 38 K, close to that of $MgB_2$, and exhibit large critical current densities, rather independent of the field at low temperatures. However, 122 compounds contain toxic As and reactive alkaline earth metals, which may be a problem for large scale fabrication processes. In this respect, 1111 compounds with the chemical composition LnFeAsO (Ln=Lanthanides) present problems as well, as they contain As and volatile F and O as well, whose stoichiometry is hardly controlled.
On the other hand, 11 compounds with the chemical composition FeCh (Ch=chalcogen ion) have a lower $T_c$ of up to 16 K, but they contain no toxic or

volatile elements [60], [95]**.** This is one of the reasons why this Thesis is dedicated to the fabrication and the characterization of samples of family 11.
Regarding FeSe, in the last years several groups in China reported the striking news that the monolayer of FeSe deposited on a $SrTiO_3$ substrate showed high $T_c$ (65 K) and they raised $T_c$ to 100 K [49],[50],[96]-[98]. Though this superconductivity emerges so far only for monolayers of FeSe, a new route to high $T_c$ materials is expected to be found [94].
The iron-chalcogenide compounds are much simpler in structure due to the neutrality of the FeSe(Te, S) layer than the Fe–As based compounds. The first discovery of superconductivity with $T_c$~8 K in FeSe compound was reported by Hsu *et al.* [9] on 15th July, 2008, and quickly followed by the reports of $FeTe_{1-x}Se_x$ ($T_c$ ~14 K) by Fang *et al*. [10] on 30th July, 2008.

### 1.6.1 Fe(Te,Se,S) system

Iron selenium binary compounds have several phases with different crystal structures. Superconductivity occurs only in $Fe_{1+\delta}Se$ with the lowest excess Fe [99], the so-called $\beta$ phase, which crystallizes into the anti-PbO tetragonal structure at ambient pressure (tetragonal P4/*nmm* space group) [9] and is considered to be the compound with the simplest structure in the Fe-based superconductors. A key observation is that the clean superconducting phase exists only in those samples prepared with intentional Se deficiency. The key ingredient of superconductivity is a quasi-two-dimensional (2D) layer consisting of a square lattice of iron atoms with tetrahedrally coordinated bonds to the selenium anions, which are staggered above and below the iron lattice, as show in Figure 4(a). These slabs, which are simply stacked and combined together with van der Waals force, are believed to be responsible for the superconductivity in this compound [100].

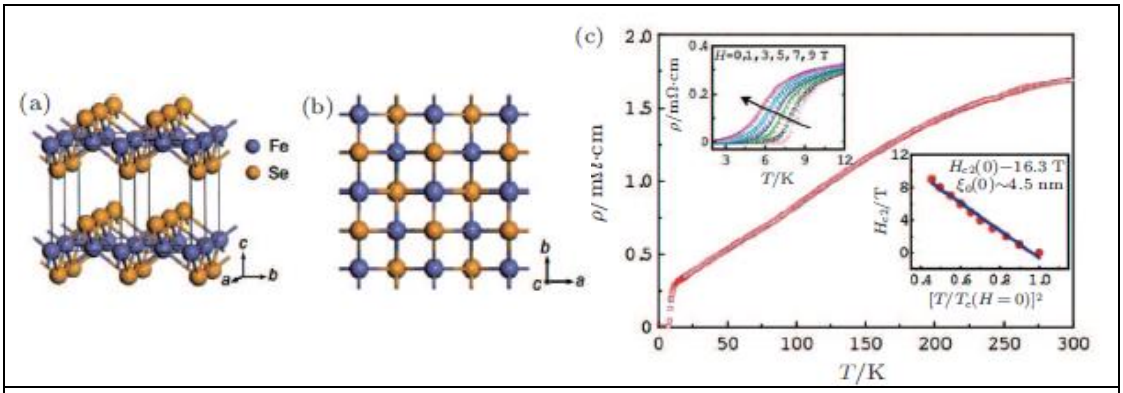


Figure 4: Crystal structure of FeSe; (b) top view from the c axis; (c) temperature dependence of electrical resistivity ρ of $FeSe_{0.88}$. The left inset shows the ρ(T) in the magnetic fields up to 9 T; the right inset displays the temperature dependence of upper critical field $H_{c2}$. From Ref. [9].

In the Fe(Te, Se, S) system, excess iron atoms can partially occupy the interstitial sites between adjacent FeX (X = Te, Se, S) layers [101] as denoted by Fe(2) in Figure 5(a). Generally, the excess $Fe^{1+}$ ions existing in both $Fe_{1+\delta}Te$ and $Fe_{1+\delta}Se$, as well as in $Fe_{1+\delta}$(Te, Se, S) lattices have an effect on their crystal structures and magnetic properties at low temperatures. It has been found that excess Fe is inevitable to stabilize the crystal structure of $Fe_{1+\delta}Se$ and the superconductivity is very sensitive to its stoichiometry. McQueen *et al*. [102] found that $Fe_{1.01}Se$ with less excess Fe atoms

undergoes a structural transition at 90 K from a tetragonal structure to an orthorhombic structure, while there is no structural transition for $Fe_{1.03}Se$ with more excess Fe atoms. This is distinct from many other iron-based parent compounds where the structural transition is usually accompanied by a magnetic phase transition [37]. The excess Fe atoms existing in Fe(Te, Se, S) lattice not only affect the crystal and magnetic structure, but also can suppress their superconductivity [103],[104]. Although FeSe and FeTe have a similar crystal structure, their physical properties are much different. Figure 5(b) shows the temperature dependences of resistivity for FeSe and FeTe. FeSe exhibits metallic behavior and undergoes a superconducting transition at $T_c^{onset}$ = 13 K. In contrast, FeTe exhibits antiferromagnetic ordering around 70K where the anomaly appears in the resistivity–temperature curve, and does not show superconductivity [105],[10],[106].

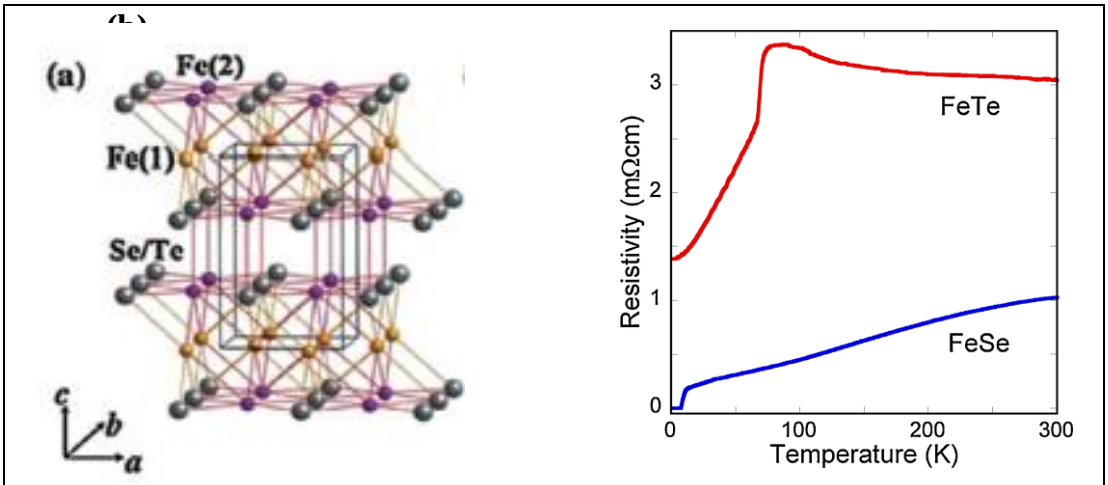


Figure 5: (a) Crystal structure of $Fe_{1+y}Te$ [100]. (b) Temperature dependence of resistivity for FeSe and FeTe. FeSe shows metallic behavior and undergoes superconducting transition. In contrast, FeTe exhibits antiferromagnetic ordering around 70K and does not show superconductivity [106], [107].

Although FeSe forms with the solid-state reaction, a sample synthesized at high temperatures contains the NiAs-type (hexagonal) FeSe phase. To obtain a single phase of PbO-type FeSe, low temperature annealing around 300–400 °C, which transforms the NiAs-type phase to the PbO-type phase, is required [99]. Figure 6(a) shows the sintering temperature dependence of the superconducting transition in the magnetization measurement. Sample (a) was reacted at 1100 °C and then annealed at 400 °C for 200 h. Samples (b) and (c) were reacted at 1100 and 680 °C, respectively, and these compounds contain the NiAs phase. The superconducting transition for sample (a) is the sharpest, and complete shielding is observed, which indicates that both the high-temperature reaction and low-temperature annealing are required to obtain a high-quality FeSe sample. In Figure 6(b) the FeSe phase diagram estimated in [99] is shown. $\beta$-FeSe is unstable at low temperatures: there is a slow conversion of the tetragonal $\beta$-$Fe_{1+\delta}Se$ phase to a hexagonal NiAs structure-type ($\alpha$-FeSe) phase that is non-superconducting above 1.8K, with larger lattice parameters than are found for $Fe_7Se_8$ [107],[109] below approximately 300 °C.

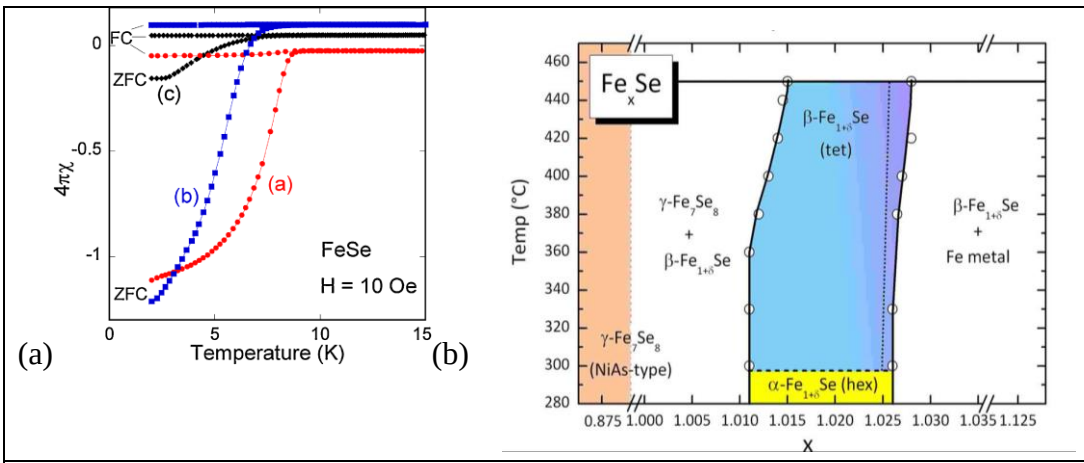


Figure 6: (a) Temperature dependence of magnetic susceptibility for the FeSe sample synthesized by three heating processes: (a) 1100 °C +400 °C for 200 h, (b) 1100 °C, and (c) 680 °C [107]. (b) FeSe Phase diagram estimated in [99]. Below 300 °C, β-$Fe_{1+\delta}Se$ slowly converts to α-$Fe_xSe$, which has the NiAs structure type and is non-superconducting above 1.8 K.

In Figure 7 physical properties of FeSeTe samples with different composition and preparation procedures are shown [107]. The samples in Figure 7(a) are almost single phase but the superconducting transitions are broad for these primitive polycrystalline samples, implying the existence of the local phase separation [105],[10],[106].
With increasing Te concentration, the tetragonal–orthorhombic structural transition observed in FeSe is suppressed. Figure 7(b) shows the temperature dependence of magnetic susceptibility at the zero-field cooling (ZFC) and field cooling (FC) for the plate-like single crystals.

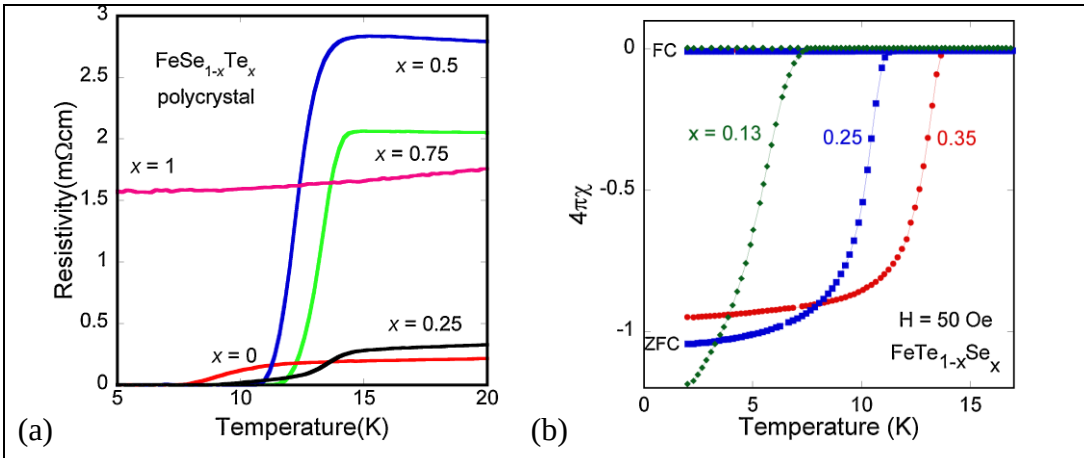


Figure 7: (a) Temperature dependence of resistivity for polycrystalline $FeTe_{1-x}Se_x$. (b) Temperature dependence of magnetic susceptibility for the $FeTe_{1-x}Se_x$ crystals grown by the melting method [107].

The phase diagram established in [107] for $Fe_{1+\delta}Te_{1-x}Se_x$ with a low excess-Fe concentration is shown in Figure 8(a). Superconductivity in this composite is tolerant to stoichiometric variations in the Se/Te ratio, anyway the highest $T_c$ appears at the tetragonal phase near x = 0.5. With further increase of Te content, the $T_c$ decreases and the antiferromagnetic (AFM) ordering accompanying the tetragonal–monoclinic distortion appears, while the bulk superconductivity disappears.

$Fe_{1+\delta}Te_{1-x}Se_x$ phase diagram has been studied by several groups and the conclusions not always reach a consensus. Liu *et al.* [103],[110] divided the phase diagram into three composition regions with distinct physical properties; considering Figure 8(b), the samples in region (I) ($0 \leq x \leq 0.09$) exhibit a long-range AFM order, while the samples in region (II) ($0.09 \leq x \leq 0.29$) exhibit neither a long-range AFM order nor bulk superconductivity. Only the samples in region (III) ($x \leq 0.29$) exhibit bulk superconductivity. Katayama *et al.* [111], on the other hand, divided the phase diagram into three composition regions: the AFM phase for $x \leq 0.1$, the superconductivity region in $x \geq 0.1$, and the intermediate spin-glass region. Khasanov *et al.* [112] suggested that in $x \sim 0.25–0.45$ region, superconductivity coexists with an incommensurate AFM order, and bulk superconductivity did not appear until $x \sim 0.5$. These discrepancies mainly concentrate on in what region bulk superconductivity emerges and whether it coexists or not with a long-range AFM order [100].

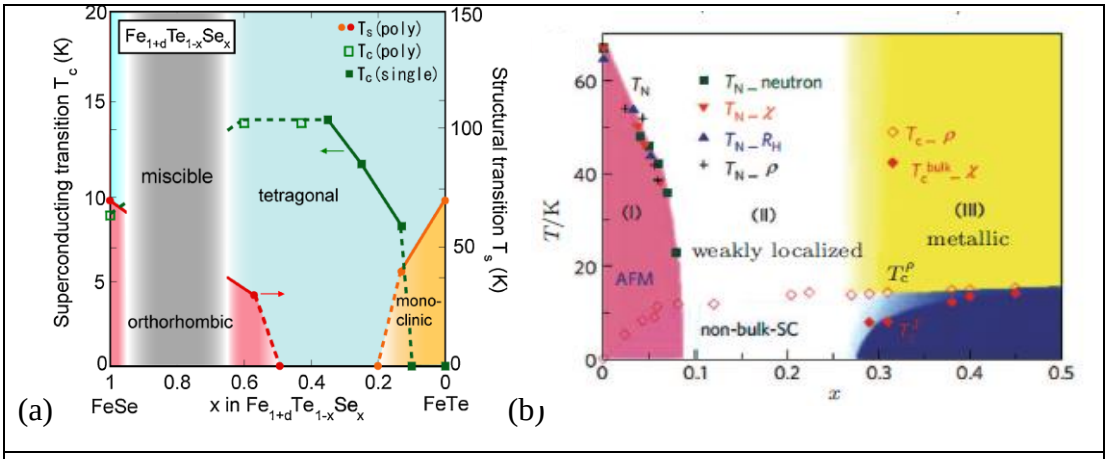


Figure 8: (a) Phase diagram of $Fe_{1+\delta}Te_{1-x}Se_x$ with low excess Fe concentration established in [107]. The tetragonal–orthorhombic structural transition is suppressed with increasing Te concentration. The highest $T_c$ appears at the tetragonal phase near x = 0.5. With increasing Te content, the $T_c$ decreases and the AFM ordering accompanying the tetragonal– monoclinic distortion grows up. (b) Phase diagram of $Fe_{1.02}Te_{1-x}Se_x$. From Refs. [103] and [110],[100].

## 1.6.2 Pressure effects on Fe-chalcogenides

FeSe shows the most significant pressure dependence of $T_c$ among the Fe chalcogenides. The $T_c$ onset and $T_c$ zero of FeSe at ambient pressure are 13 and 8.5 K, respectively. The $T_c$ onset dramatically increases above 20 K at 1.48 GPa; the first observation of the huge pressure effect was achieved using a piston–cylinder cell, as shown in Figure 9(a) [107]. Interestingly, the transition becomes sharper around 0.5 GPa than that at ambient pressure. With applying further pressure using a diamond-anvil cell, the $T_c$ onset reached 37 K as displayed in Figure 9(b) [113],[95], [114]. With increasing pressure, the lattice constants a, b, c, volume (V) and the Fe–Se distance decreases monotonously. The Se–Fe–Se angle decreased from 104.53° (at 0.25 GPa) to 103.2° (at 9.0 GPa) with increasing pressure.

Positive pressure effect was observed for $FeTe_{1-x}Se_x$ as well [115],[116]. Figure 10(a) shows the temperature dependence of resistivity for $Fe_{1.03}Te_{0.43}Se_{0.57}$ under high pressure up to 11.9 GPa. The crystal structural analysis under high pressure was also performed using synchrotron x-ray diffraction. Figure 10(b) displays a pressure–temperature phase diagram for $Fe_{1.03}Te_{0.43}Se_{0.57}$. A pressure-induced orthorhombic-monoclinic transition is observed around 2 – 3 GPa, and the $T_c$ decreases above this

pressure region. Also for $FeSe_{0.5}Te_{0.5}$, similar pressure dependence of $T_c$ was observed. Furthermore, $FeTe_{0.75}Se_{0.25}$, which is a superconductor close to the antiferromagnetically ordered phase, shows a positive pressure effect. The temperature dependence of magnetization under high pressure up to 0.99 GPa: with increasing pressure, both the $T_c$ and the superconducting volume fraction were enhanced [107].

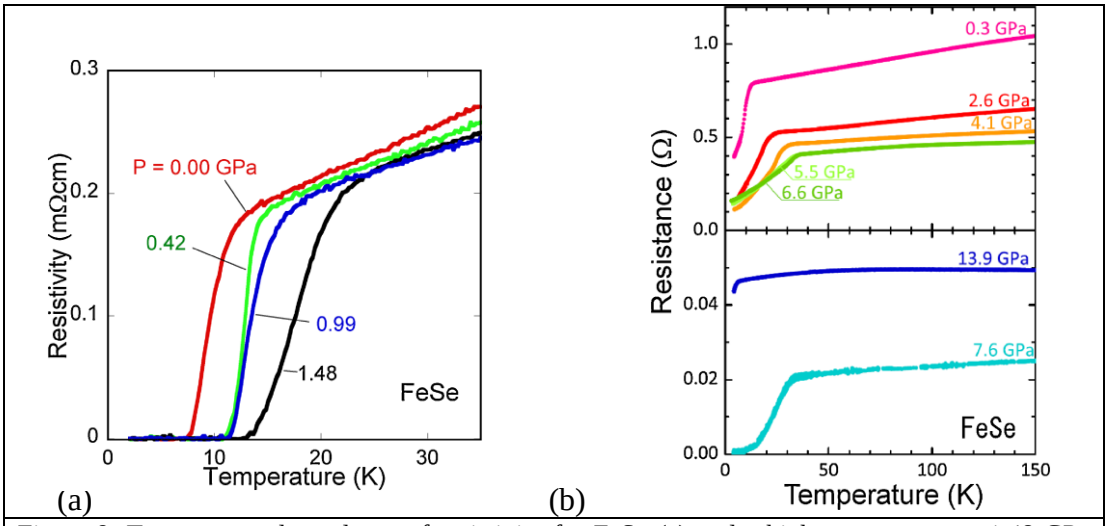


Figure 9: Temperature dependence of resistivity for FeSe (a) under high pressure up to 1.48 GPa using a piston cylinder cell [107]. (b) measured using a diamond-anvil cell for FeSe under high pressure up to 13.9 GPa [113].

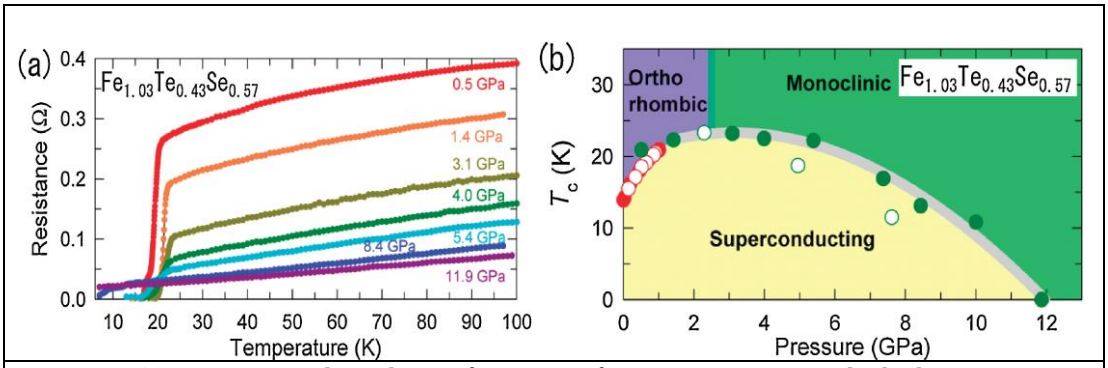


Figure 10: (a) Temperature dependence of resistivity for $Fe_{1.03}Te_{0.43}Se_{0.57}$ under high pressure up to 11.9 GPa. (b) Pressure–temperature phase diagram of $Fe_{1.03}Te_{0.43}Se_{0.57}$ [115].

### 1.6.3 Electronic structure

The band structure and Fermi surface of the bulk FeSe superconductor from the band structure calculations show similar behaviours to other iron based superconductors, i.e. the low energy electronic states originate mainly from the iron 3d orbitals and there are two hole-like Fermi surface sheets at the zone centre and two intersecting electron-like Fermi surface sheets around the zone corner [117]. With the latest progress on growing high-quality FeSe single crystals [118]–[120], several ARPES

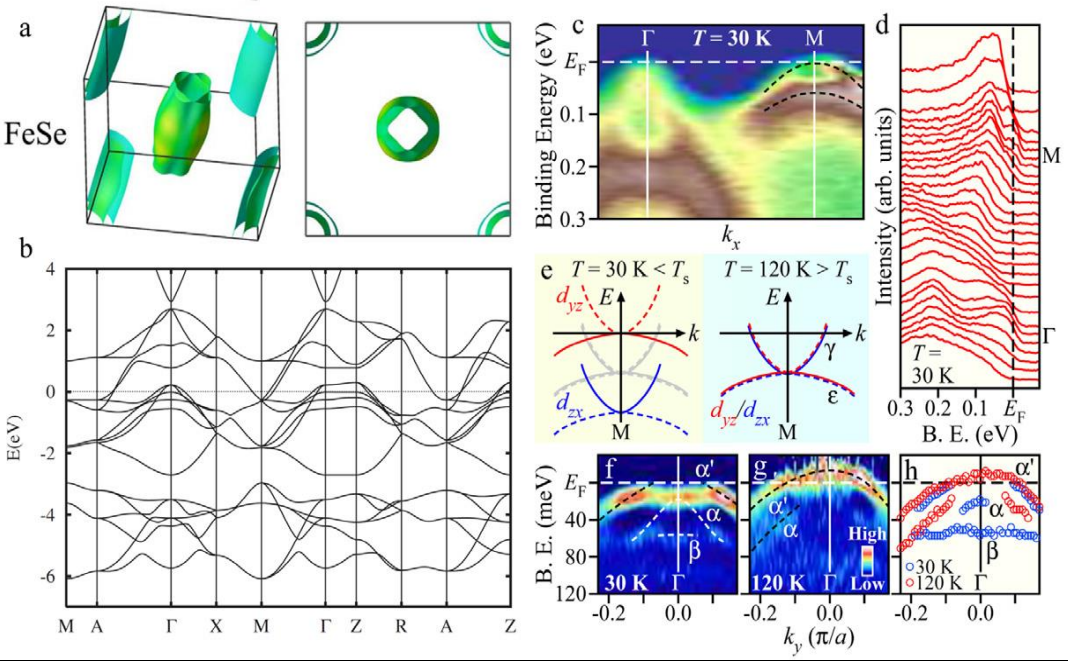


Figure 11: Fermi surface and band structure of the bulk FeSe from band structure calculations and angle-resolved photoemission measurements. (*a*) and (*b*) LDA calculated Fermi surface and band structure of bulk FeSe, [117]. (*c*) and (*d*) ARPES intensity and corresponding EDCs, respectively, along the *Γ*-M cut at $T$ = 30 K. (*e*) Schematic band diagram around the M point below/above the structural transition temperature $T_s$. Red and blue curves indicate the $d_{yz}$ and $d_{zx}$ orbitals, respectively. Solid and dashed curves represent the band dispersion along the (0, 0)–($\pi$, 0) and (0, 0)–(0,$\pi$) directions (longer Fe–Fe and shorter Fe–Fe directions) of the untwined crystal, respectively. (*f* ) and (*g*) Comparison of the second-derivative plot of the near-$E_F$ ARPES intensity around the *Γ* point between $T$ = 30 and 120 K. (*h*) Experimental band dispersion around the *Γ* point at $T$ = 30K (blue circles) and 120K (red circles), extracted by tracing the peak maxima of the EDCs divided by the Fermi-Dirac function, [122].

measurements on the FeSe superconductor have become available [121]-[123].
The ARPES results on FeSe single crystals reported so far give a basically consistent picture, as exemplified in Figure 11 [121]-[124].
Extensive ARPES measurements have been carried out on the Fe(Se,Te) system as well, to investigate its electronic structure and superconducting gap [125]-[132]. Typical results are summarized in Figure 12. Direct comparison between measurements and band structure calculations indicates a strong orbital selective renormalization in the normal state [132],[133]. In the optimally-doped $FeTe_{0.55}Se_{0.45}$ superconductor, the measured superconducting gap is nearly isotropic both near the zone centre and the zone corner (Figure 12(*g*)) [127]. These ARPES results are consistent with the STM measurement on Fe(Te,Se) that points to an unconventional s wave (s±-wave symmetry) superconducting gap [134]. In Fe(Se,Te) superconductors, like in the FeSe superconductor case [135], the Fermi energy is comparable to the superconducting gap [124].

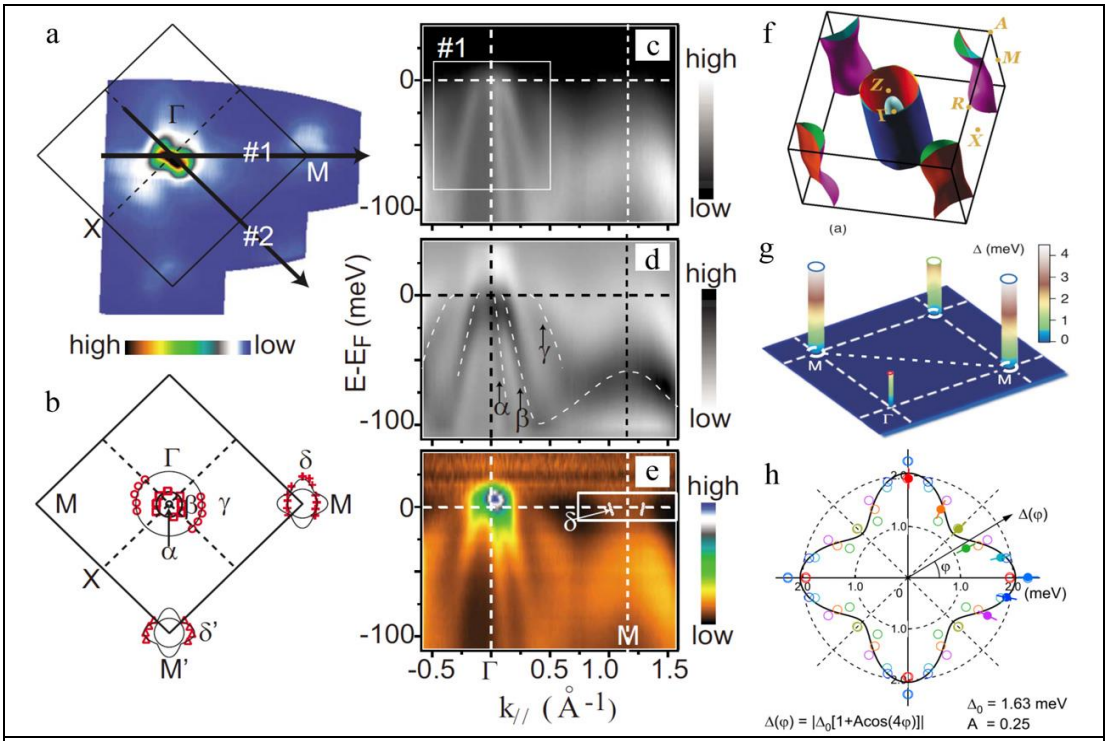


Figure 12: Fermi surface, band structure and superconducting gap of Fe(Te,Se). (*a*) Fermi surface of $Fe_{1.04}Te_{0.66}Se_{0.34}$. (*b*) The Fermi surfaces are constructed based on the measured Fermi crossings. (*c*) The photoemission intensity along the cut 1 in the $\Gamma$-M direction and (*d*) its second derivative with respect to energy. (*e*) The data in panel (*c*) are re-plotted after dividing the angle integrated energy distribution curve. (*f* ) The calculated Fermi surface of $Fe_{1.04}Te_{0.66}Se_{0.34}$ [125]. (*g*) Three-dimensional representation of the superconducting gap with the Fermi surface topology of $FeTe_{0.55}Se_{0.45}$ [127]. (*h*) Fermi surface-angle dependence of superconducting gap size of $FeTe_{0.6}Se_{0.4}$ [128].

## References


[1] Kamihara, Y., Watanabe, T., Hirano, M., & Hosono, H. (2008) Iron-based layered superconductor $La[O_{1-x}F_x]FeAs$ (x=0.05 -0.12) with $T_c$=26K. *Journal of the American Chemical Society*, 130, 3296.

[2] Kamihara, Y. *et al*. (2006). Iron-based layered superconductor: LaOFeP. *Journal of the American Chemical Society*, 128, 10012-10013.

[3] Zhi-AN R., *et al.* (2008) Superconductivity at 55 K in iron-based F-doped layered quaternary compound $Sm[O_{1-x}F_x]FeAs$. *Chinese Physics Letters*, *25*, 2215.

[4] Rotter M., Tegel M. and Johrendt D. (2008) Superconductivity at 38 K in the iron arsenide $(Ba_{1-x}K_x)Fe_2As_2$. *Physical Review Letters*, *101*, 107006.

[5] Yang J., *et al.* (2008), Superconductivity at 53.5 K in $GdFeAsO_{1-\delta}$ *Supercond. Sci.Technol.* 21 082001.

[6] Wen H.H. *et al.* (2008) Superconductivity at 25 K in hole-doped Superconductivity at 25 K in hole-doped $(La_{1-x}Sr_x)OFeAs$ *Europhys. Lett*. 82, 17009

[7] Rotter, M., *et al.* (2008) Spin-density-wave anomaly at 140 K in the ternary iron arsenide $BaFe_2As_2$ *Physical Review B*, 78, 020503.

[8] Wang X. C. *et al*. (2008) The superconductivity at 18 K in LiFeAs system *Solid. State. Commun*. 148 538.

[9] Hsu F-C *et al*. (2008) Superconductivity in the PbO-type structure α-FeSe. *Proc. Natl. Acad. Sci. USA* 105 14262.

[10] Fang M. H., Pham H. M., Qian B., Liu T. J., Vehstedt E. K., Liu Y., Spinu L. and Mao Z. Q. (2008) Superconductivity close to magnetic instability in $Fe(Se_{1-x}Te_x)_{0.82}$. *Phys. Rev. B* 78 224503.

[11] Mizuguchi Y., Tomioka F., Tsuda S., Yamaguchi T. and Takano Y. (2009) Superconductivity in S-substituted FeTe. *Appl. Phys. Lett*. 94 012503.

[12] Tropeano M. (2011) The Fe based compounds: from magnetic ordering to superconductivity. *PhD Thesis*, Scuola di Dottorato in scienze e Tecnologie della Chimica e dei Materiali, Università degli Studi di Genova.
[13] Puri A. (2012) Experiments on strongly correlated materials under extreme conditions. *PhD Thesis*, Scuola di Dottorato "Vito Volterra" in Scienza dei materali, Univeristà la Sapienza di Roma.
[14] Yakita H. *et al.* (2014) A new layered iron arsenide superconductor: (Ca,Pr)$FeAs_2$ *J. Am. Chem. Soc*. 136 846.
[15] A. S. et al. (2014) Synthesis and physical properties of $Ca_{1-x}RE_xFeAs_2$ with RE = La–Gd. *Appl. Phys. Express* 7 073102.
[16] Katrych S. *et al.* (2014) $L_4Fe_2As_2Te_{1-x}O_{4-y}F_y$ (L = Pr, Sm, Gd): a layered oxypnictide superconductor with $T_c$ up to 45 K. *Phys. Rev. B* 89 024518.
[17] Katrych S. *et al.* (2013) $Pr_4Fe_2As_2Te_{1-x}O_4$: A layered FeAs based superconductor *Phys. Rev*. 87 180508(R).
[18] Zhu X., Han F., Mu G., Cheng P., Shen B., Zeng B. and Wen H-H (2009) Transition of stoichiometric $Sr_2VO_3FeAs$ to a superconducting state at 37.2 K. *Phys. Rev. B* 79 220512(R).
[19] Pachmayr U. *et al*. (2015) Coexistence of 3d-Ferromagnetism and Superconductivity in $[(Li_{1-x}Fe_x)$ OH$](Fe_{1-y}Li_y)$Se *Angew. Chem. Int. Ed*. 54 293–7.
[20] Chu C. W. (2009) Alive and Kicking. *Nature Physics* 5 787-789.
[21] Day C. (2009) Iron based superconductors. *Physics Today - American Institute of Physics* 36-40.
[22] Putti M. *et al*. (2010) New Fe-based superconductors: properties relevant for applications. *Supercond. Sci. Technol.* 23 034003 (10pp).
[23] Aswathy P.M., Anooja J. B., Sarun P.M and Syamaprasad U. (2010) An overview on iron based superconductors. *Supercond. Sci. Technol*. 23 073001 (20pp).
[24] Hosono H. and Kuroki K. (2015) Iron based superconductors: Current status of materials and pairing mechanism. *Physica C* 514 399-422.
[25] Paglione J. and Greene R. L., (2010) High-temperature superconductivity in iron-based materials. *Nature Physics* 6 645-658.
[26] Lee C-H. *et al.* (2008) Effect of structural parameters on superconductivity in fluorine-free $LnFeAsO_{1-y}$ (Ln=La, Nd). *J. Phys. Soc. Jpn* 77, 083704.
[27] Gooch M. *et al*. (2009) Superconductivity in ternary iron pnictides: $AFe_2As_2$ (A = alkali metal) and LiFeAs. *Physica C* 470 1 S276.
[28] Singh D. J. (2009) Electronic structure of Fe-based superconductors. *Physica C* 469 418-424.
[29] Sebastian S. E. (2012). Quantum oscillations in iron pnictide superconductors. In N.L.Wang, H. Hosono, P. C. Dai (Eds.), *Iron-based superconductors—materials, properties and mechanisms. Singapore: Pan Standford Publishing.*
[30] Lu D. H. *et al*. (2008) Electronic structure of the iron-based superconductor LaOFeP. *Nature* 455 81-84.
[31] Kondo T. *et al.* (2008) Momentum dependence of the superconducting gap in $NdFeAsO_{0:9}F_{0:1}$ single crystals measured by angle resolved photoemission spectroscopy. *Phys. Rev. Lett* 101, 147003.
[32] Ding H. *et al.* (2008) Observation of Fermi-surface-dependent nodeless superconducting gaps in $Ba_{0:6}K_{0:4}Fe_2As_2$. *Europhys. Lett*. 83, 47001.
[33] Shishido H. *et al.* (2010) Evolution of the Fermi surface of $BaFe_2(As_{1-x}P_x)_2$ on entering the superconducting dome. *Phys. Rev. Lett.* 104, 057008.
[34] Harrison N. *et al.* (2009) Quantum oscillations in antiferromagnetic $CaFe_2As_2$ on the brink of superconductivity. *J. Phys. Condens. Matter* 21, 32220.
[35] Mazin I. I. and Schmalian J. (2009) Pairing symmetry and pairing state in ferropnictides: Theoretical overview. *Physica C* 469, 614-623.
[36] Yildirim T. (2008) Origin of the 150 K anomaly in LaFeAsO: Competing antiferromagnetic interactions, frustration, and a structural phase transition. *Phys. Rev. Lett*. 101, 057010.
[37] de la Cruz C. *et al.* (2008) Magnetic order close to superconductivity in the iron-based layered $LaO_{1-x}F_xFeAs$ systems. *Nature* 453 899-902.
[38] Johnston D. C. (2010) The puzzle of high temperature superconductivity in layered ironpnictides and chalcogenides. *Advances in Physics*, *59*, 803.
[39] Popovich P. *et al.* (2010) Specific heat measurements of $Ba_{0.68}K_{0.32}Fe_2As_2$ single crystals: evidence for a multiband strong-coupling superconducting state. *Physical Review Letters 105*, 027003.
[40] Charnukha A. *et al.* (2011) Eliashberg approach to infrared anomalies induced by the superconducting state of $Ba_{0.68}K_{0.32}Fe_2As_2$ single crystals. *Physical Review B, 84*, 174511.
[41] Shan L., et al. (2012). Evidence of a spin resonance mode in the iron-based superconductor $Ba_{0.6}K_{0.4}Fe_2As_2$ from scanning tunneling spectroscopy. *Physical Review Letters, 108*, 227002.

[42] Z.A. Ren *et al*. (2008) Superconductivity at 55 K in iron-based F-doped layered quaternary compound $SmO_{1-x}F_xFeAs$ *Chin. Phys. Lett*. 25 2215.
[43] Chen T. Y., Tesanovic Z., Liu R. H., Chen X. H. and Chien C. L. (2008) A BCS-like gap in the superconductor $SmFeAsO_{0:8}5F_{0:15}$. *Nature* 453 1224_1227.
[44] Mazin I. I., Singh D. J., Johannes M. D. and Du M. H. (2008) Unconventional superconductivity with a sign reversal in the order parameter of $LaFeAsO_{1-x}F_x$. *Phys. Rev. Lett*. 101 057003.
[45] Boeri L., Dolgov O. V., and Golubov A. A. (2008) Is $LaFeAsO_{1-x}F_x$ an electron-phononsuperconductor? *Physical Review Letters*, *101*, 026403.
[46] Moriya T., and Ueda K. (2003) Antiferromagnetic spin fluctuation and superconductivity. *Reports on Progress in Physics*, *66*, 1299.
[47] Scalapino D. J., Loh E., and Hirsch J. E. (1986) *d*-wave pairing near a spin-density-wave instability. *Physical Review B*, *34*, 8190–8192.
[48] Iimura S. *et al.* (2012) Two-dome structure in electron-doped iron arsenide superconductors *Nat. Commun*. 3 943.
[49] Wang Q-Y *et al.* (2012) Interface-induced high-temperature superconductivity in single unit-cell FeSe films on $SrTiO_3$ *Chin. Phys. Lett*. 29 037402
[50] Tan S. Y. *et al.* (2013) Interface-induced superconductivity and strain-dependent spin density waves in FeSe/$SrTiO_3$ *Nat. Mater*. 12 634
[51] Guo J. *et al.* (2010) Superconductivity in the iron selenide $K_xFe_2Se_2$ ($0 \leq x \leq 1.0$) *Phys. Rev. B* 82 180520.
[52] Qian T. *et al* (2011) Absence of a Holelike Fermi Surface for the Iron-Based $K_{0.8}Fe_{1.7}Se_2$ Superconductor Revealed by Angle-Resolved Photoemission Spectroscopy *Phys. Rev. Lett.* 106 187001.
[53] Kontani H. and Onari S. (2010) Orbital-Fluctuation-Mediated Superconductivity in Iron Pnictides: Analysis of the Five-Orbital Hubbard-Holstein Model *Phys. Rev. Lett.* 104 157001.
[54] Schnering H.G.v. *et al*. (1988) Chemistry and structural chemistry of phosphides and polyphosphides *Chem. Rev*. 88, 243.
[55] Zimmer B.I. *et al*. (1995) The rate earth transition metal phosphide oxides LnFePO, LnRuPO and LnCoPO with ZrCuSiAs type structure *J. Alloys Comp*. 229, 238.
[56] Ni N. *et al.* (2008) Anisotropic thermodynamic and transport properties of single-crystalline $Ba_{1-x}K_xFe_2As_2$ (x=0 and 0.45) *Phys. Rew. B* 78, 014507.
[57] Su Y. *et al.* (2009) Antiferromagnetic ordering and structural phase transition in $Ba_2Fe_2As_2$ with Sn incorporated from the growth flux *Phys. Rew. B* 79, 064504
[58] Sefat A. S. *et al.* (2010) Superconductivity at 22 K in Co-Doped $BaFe_2As_2$ Crystals *Phys. Rew. Lett*. 101, 117004.
[59] Karpinski J. *et al.* (2009) Single crystals of $LnFeAsO_{1-x}Fx$ (Ln = La, Pr, Nd, Sm, Gd) and $Ba_{1-x}Rb_xFe_2As_2$: Growth, structure and superconducting properties *Physica C* 469, 370.
[60] Pallecchi I., Eisterer M., Malagoli A., and Putti M. (2015) Application potential of Fe-based superconductors *Supercond. Sci. Technol*. 28 114005 (12pp).
[61] Tarantini C. *et al*. (2010) Strong vortex pinning in Co-doped $BaFe_2As_2$ single crystal thin films *Appl. Phys. Lett*. 96 142510.
[62] Si W. *et al*. (2013) High current superconductivity in $FeSe_{0.5}Te_{0.5}$-coated conductors at 30 tesla *Nat. Commun*. 4 1347.
[63] Braccini V. *et al.* (2013) Highly effective and isotropic pinning in epitaxial Fe(Se,Te) thin films grown on CaF2 substrates *Appl. Phys. Lett.* 103 172601.
[64] Kurth F. *et al.* (2015) Unusually high critical current of clean P-doped $BaFe_2As_2$ single crystalline thin film *Appl. Phys. Lett.* 106 072602.
[65] Iida K. *et al.* (2013) Oxypnictide SmFeAs(O,F) superconductor: a candidate for high-field magnet applications *Sci. Rep*. 3 2139.
[66] Lee S. *et al.* (2010) Template engineering of Co-doped $BaFe_2As_2$ single-crystal thin films *Nat. Mater*. 9 397.
[67] Fang L. *et al.* (2013) Huge critical current density and tailored superconducting anisotropy in $SmFeAsO_{0.8}F_{0.15}$ by low-density columnar-defect incorporation *Nat. Commun*. 4 2655.
[68] Fujioka M. *et al.* (2013) Phase diagram and superconductivity at 58.1 K in α-FeAs-free $SmFeAsO_{1-x}F_x$ *Supercond. Sci. Technol*. 26 085023.
[69] Pallecchi I. *et al.* (2012) Upper critical fields and critical current densities of Fe-based superconductors as compared to those of other technical superconductors *Physica C* 482 68.
[70] Eisterer M. *et al.* (2014) Critical current anisotropy in Nd-1111 single crystals and the infuence of neutron irradiation *Supercond. Sci. Technol.* 27 044009.
[71] Bellingeri E. *et al.* (2012) Strong vortex pinning in $FeSe_{0.5}Te_{0.5}$ epitaxial thin film *Appl. Phys. Lett*. 100 082601.
[72] Nakajima Y. M. *et al.* (2009) Enhancement of critical current density in Co-doped $BaFe_2As_2$ with columnar defects introduced by heavy-ion irradiation *Phys. Rev. B* 80 012510.

[73] Eisterer M. et al. (2009) Effects of disorder on the superconducting properties of $BaFe_{1.8}Co_{0.2}As_2$ single crystals *Supercond. Sci. Technol*. 22 095011.
[74] Tarantini C. *et al.* (2012) Artificial and self-assembled vortex-pinning centers in superconducting $Ba(Fe_{1-x}Co_x)_2As_2$ thin films as a route to obtaining very high critical-current densities *Phys. Rev. B* 86 214504
[75] Moll P. J. W. *et al.* (2010) High magnetic-field scales and critical currents in SmFeAs(O, F) crystals *Nat. Mater*. 9 628.
[76] Tanatar M. A. *et al*. (2009) Anisotropy of the iron pnictide superconductor $Ba(Fe_{1-x}Co_x)_2As_2$ (x = 0.074, $T_c$ = 23 K) *Phys. Rev. B* 79 094507.
[77] Crabtree G. W. *et al.* (1987) Large anisotropic critical magnetization currents in single-crystal $YBa_2Cu_3O_{7-\delta}$ *Phys. Rev. B* 36 4021.
[78] Hilgenkamp H. and Mannhart J. (2002) Grain boundaries in high-$T_c$ superconductors *Rev. Mod. Phys.* 74 485.
[79] Lee S *et al*. (2009) Weak-link behavior of grain boundaries in superconducting $Ba(Fe_{1-x}Co_x)_2As_2$ bicrystals *Appl. Phys. Lett*. 95 212505.
[80] Katase T. *et al.* (2011) Advantageous grain boundaries in iron pnictide superconductor *Nat. Commun*. 2 409.
[81] Graser S. *et al*. (2010) How grain boundaries limit supercurrents in high-temperature superconductors *Nat. Mater*. 6 609.
[82] Zhang Q *et al*. (2014) Enhancement of transport critical current density of $SmFeAsO_{1-x}F_x$ tapes fabricated by an ex-situ powder-in-tube method with a Sn-presintering process *Appl. Phys. Lett.* 104 172601
[83] Wang C. *et al*. (2012) Effect of starting materials on the superconducting properties of SmFe $AsO_{1-x}F_x$ tapes *Supercond. Sci. Technol*. 25 035013.
[84] Ozaki T. *et al.* (2012) Fabrication of binary FeSe superconducting wires by novel diffusion process *J. Appl. Phys*. 111 112620.
[85] Izawa H., Mizuguchi Y., Takano Y. and Miura O. (2014) Fabrication of $FeTe_{0.4}Se_{0.6}$ superconducting tapes by a chemical-transformation PIT process *Physica C* 504 77.
[86] Iida K. *et al.* (2009) Strong $T_c$ dependence for strained, epitaxial $Ba(Fe_{1-x}Co_x)_2As_2$ thin films *Appl. Phys. Lett*. 95 192501.
[87] Katase T. *et al.* (2011) Biaxially textured cobalt-doped $BaFe_2As_2$ films with high critical current density over 1MA $cm^{-2}$ on MgO-buffered metal-tape flexible substrates *Appl. Phys. Lett.* 98 242510.
[88] Trommler S. *et al.* (2012) Architecture, microstructure and $J_c$ anisotropy of highly oriented biaxially textured Co-doped $BaFe_2As_2$ on Fe/IBAD-MgO-buffered metal tapes *Supercond. Sci. Technol.* 25 084019.
[89] Iida K. et al (2011) Epitaxial growth of superconducting $Ba(Fe_{1-x}Co_x)_2As_2$ thin films on technical IBAD-MgO substrates *Appl. Phys. Express* 4 013103.
[90] Si W. *et al.* (2011) Iron-chalcogenide $FeSe_{0.5}Te_{0.5}$ coated superconducting tapes for high field applications *Appl. Phys. Lett*. 98 262509.
[91] Iida K. *et al.* (2014) Highly textured oxypnictide superconducting thin films on metal substrates *Appl. Phys. Lett*. 105 172602.
[92] Sato H., Hiramatsu H., Kamiya T. and Hosono H. (2014) High critical-current density with less anisotropy in $BaFe_2(As,P)_2$ epitaxial films: Effect of intentionally grown *c*-axis vortex-pinning centers *Appl. Phys. Lett*. 104 182603.
[93] Miura M. *et al.* (2013) Strongly enhanced flux pinning in one-step deposition of $BaFe_2(As_{0.66}P_{0.33})_2$ superconductor films with uniformly dispersed $BaZrO_3$ nanoparticles *Nat. Commun*. 4 2499.
[94] Hosono H. *et al*. (2015) Exploration of new superconductors and functional materials, and fabrication of superconducting tapes and wires of iron pnictide *Sci. Technol. Adv. Mater.* 16 033503 (87pp).
[95] Medvedev S. *et al*. (2009) Electronic and magnetic phase diagram of $\beta$-$Fe_{1.01}Se$ with superconductivity at 36.7 K under pressure *Nat. Mater*. 8 630.
[96] He S.L. *et al.* (2013) Phase diagram and electronic indication of high-temperature superconductivity *Nat. Mater*. 12 605.
[97] Liu D. *et al*. (2012) Electronic origin of high-temperature superconductivity in single-layer FeSe superconductor *Nat. Commun*. 3 931.
[98] Ge J-F *et al.* (2014) Superconductivity above 100 K in single-layer FeSe films on doped $SrTiO_3$ *Nat. Mater*. 14 285.
[99] McQueen T. M. et al. (2009) Extreme sensitivity of superconductivity to stoichiometry in $Fe_{1+\delta}Se$ *Phys. Rev. B* 79 014522.
[100] Dong C-H, Wang H-D and Fang M-H (2013) Exploration of iron-chalcogenide superconductors *Chin. Phys. B* vol. 22, No. 8 087401.
[101] Bao W. *et al*. (2009) Tunable ($\delta\pi$, $\delta\pi$)-Type Antiferromagnetic Order in $\alpha$-Fe(Te,Se) Superconductors *Phys. Rev. Lett*. 102 247001.

[102] McQueen T. M. *et al.* (2009) Tetragonal-to-Orthorhombic Structural Phase Transition at 90 K in the Superconductor $Fe_{1.01}Se$ *Phys. Rev. Lett.* 103 057002.
[103] Liu T. J. *et al.* (2009) Charge-carrier localization induced by excess Fe in the superconductor $Fe_{1+y}Te_{1-x}Se_x$ *Phys. Rev. B* 80 174509.
[104] Paulose P. L., Yadav C. S. and. Subhedar K. M. (2010) Magnetic phase diagram of $Fe_{1.1}Te_{1-x}Se_x$: A comparative study with the stoichiometric superconducting $FeTe_{1-x}Se_x$ system *Europhys. Lett*. 90 27011.
[105] Yeh K. W. *et al.* (2008) Tellurium substitution effect on superconductivity of the α-phase iron selenide *Europhys. Lett*. 84 37002.
[106] Mizuguchi Y., Tomioka F., Tsuda S., Yamaguchi T. and Y. Takano (2009) Substitution Effects on FeSe Superconductor *J. Phys. Soc. Jpn*. 78 074712.
[107] Mizuguchi Y. and Takano Y. (2010) Review of Fe Chalcogenides as the Simplest Fe-Based Superconductor *J. Phys. Soc. Jpn*, vol. 79, No. 10.
[108] Mizuguchi Y., Tomioka F., Tsuda S., Yamaguchi T. and Y. Takano (2008) Superconductivity at27K in tetragonal FeSe under high pressure *Appl. Phys. Lett.* 93, 152505.
[109] Margadonna S. *et al.* (2008) Crystal structure of the new $FeSe_{1-x}$ superconductor *Chem. Commun*. (Cambridge), 5607.
[110] Liu T. J. *et al.* (2010) From (π,0) magnetic order to superconductivity with (π,π) magnetic resonance in $Fe_{1.02}Te_{1-x}Se_x$ *Nat. Mater*. 9 718.
[111] Katayama N. *et al.* (2010) Investigation of the Spin-Glass Regime between the Antiferromagnetic and Superconducting Phases in $Fe_{1+y}Se_xTe_{1-x}$ *J. Phys. Soc. Jpn*. 79 113702.
[112] Khasanov R. *et al.* (2009) Coexistence of incommensurate magnetism and superconductivity in $Fe_{1+y}Se_xTe_{1-x}$ *Phys. Rev. B* 80 140511.
[113] Margadonna S. *et al.* (2009) Pressure evolution of the low-temperature crystal structure and bonding of the superconductor FeSe ($T_c$=37 K) *Phys. Rev*. B 80 064506.
[114] Masaki S. *et al.* (2009) Precise Pressure Dependence of the Superconducting Transition Temperature of FeSe: Resistivity and $^{77}$Se-NMR Study *J. Phys. Soc. Jpn*. 78 063704.
[115] Gresty N. C. *et al.* (2009) Structural Phase Transitions and Superconductivity in Fe(1+delta)Se0.57Te0.43 at Ambient and Elevated Pressures *J. Am. Chem. Soc*. 131 16944.
[116] Horigane K *et al.* (2009) First Investigation of Pressure Effects on Transition from Superconductive to Metallic Phase in $FeSe_{0.5}Te_{0.5}$ *J. Phys. Soc. Jpn*. 78 063705.
[117] Subedi A. (2008) Density functional study of FeS, FeSe, and FeTe: Electronic structure, magnetism, phonons, and superconductivity *Phys. Rev. B* 78 134514.
[118] Boehmer A. E. (2013) Lack of coupling between superconductivity and orthorhombic distortion in stoichiometric single-crystalline FeSe *Phys. Rev. B* 87 180505.
[119] Huynh K. K. *et a.l* (2014) Electric transport of a single-crystal iron chalcogenide FeSe superconductor: Evidence of symmetry-breakdown nematicity and additional ultrafast Dirac cone-like carriers *Phys. Rev.* B 90 144516.
[120] Ma M. W. *et al.* (2014) Flux-free growth of large superconducting crystal of FeSe by traveling-solvent floating-zone technique *Supercond. Sci. Technol.* 27 122001.
[121] Maletz J. *et al.* (2014) Unusual band renormalization in the simplest iron-based superconductor $FeSe_{1-x}$ *Phys. Rev.* B 89 220506.
[122] Nakayama K. *et al.* (2014) Reconstruction of Band Structure Induced by Electronic Nematicity in an FeSe Superconductor *Phys. Rev. Lett.* 113 237001.
[123] Shimojima T. *et al.* (2014) Lifting of *xz*/*yz* orbital degeneracy at the structural transition in detwinned FeSe *Phys. Rev.* B 90 121111.
[124] Liu X. *et al.* (2015) Electronic structure and superconductivity of FeSe-related superconductors *J. Phys. Condens. Matter* 27 183201 (22pp).
[125] Chen F. *et al.* (2010) Electronic structure of $Fe_{1.04}Te_{0.66}Se_{0.34}$ *Phys. Rev.* B 81 014526.
[126] Lubashevsky Y. *et al.* (2012) Shallow pockets and very strong coupling superconductivity in $FeSe_xTe_{1-x}$ *Nat. Phys.* 8 309.
[127] Miao H. *et al.* (2012) Isotropic superconducting gaps with enhanced pairing on electron Fermi surfaces in $FeTe_{0.55}Se_{0.45}$ *Phys. Rev.* B 85 094506.
[128] Okazaki K. *et al.* (2012) Evidence for a cos(4φ) Modulation of the Superconducting Energy Gap of Optimally Doped $FeTe_{0.6}Se_{0.4}$ Single Crystals Using Laser Angle-Resolved Photoemission Spectroscopy *Phys. Rev. Lett.* 109 237011.
[129] Okazaki K. *et al.* (2014) Superconductivity in an electron band just above the Fermi level: possible route to BCS-BEC superconductivity *Sci. Rep.* 4 4109.
[130] Ieki E. *et al.* (2014) Evolution from incoherent to coherent electronic states and its implications for superconductivity in $FeTe_{1-x}Se_x$ *Phys. Rev.* B 89 140506.
[131] Nakayama K. *et al.* (2010) Angle-Resolved Photoemission Spectroscopy of the Iron-Chalcogenide Superconductor $Fe_{1.03}Te_{0.7}Se_{0.3}$: Strong Coupling Behavior and the Universality of Interband Scattering *Phys. Rev. Lett.* 105 197001.

[132] Tamai A. *et al.* (2010) Strong Electron Correlations in the Normal State of the Iron-Based $FeSe_{0.42}Te_{0.58}$ Superconductor Observed by Angle-Resolved Photoemission Spectroscopy *Phys. Rev. Lett.* 104 097002.
[133] Yin Z. P. *et al.* (2011) Kinetic frustration and the nature of the magnetic and paramagnetic states in iron pnictides and iron chalcogenides *Nat. Mater.* 10 932.
[134] Hanaguri T. *et al.* (2010) Unconventional *s*-Wave Superconductivity in Fe(Se,Te) *Science* 328 474.
[135] Kasahara S. *et al.* (2014) Field-induced superconducting phase of FeSe in the BCS-BEC cross-over *Proc. Natl Acad. Sci.* 111 16309.

CHAPTER 2

# Experimental procedures for the preparation of Iron chalcogenides polycrystalline samples

Different and well established synthesis methods have been used for the IBSC by many research groups in the last eight years. In this work I do not explain in details the methods used for IBSC samples fabrication by the scientific community, also because this descriptive material can be found in literature and is continuously under development, as the fabrication routes can be different for the different families and within the same family as well depending also on the kind of sample that is under development. I will, at certain points, describe the synthesis of samples of the 11 family developed by other research groups for comparison to mine, as of course I tried, especially at the beginning, to reproduce some of the interesting results I found in literature. So, during the description of the preparation of the samples that I performed during these years, I make some comparison with the processes developed by others, in order to clarify the meaning of the results I obtained with the measurement of the superconducting properties of my samples and in order to contextualize my results in the frame of the progresses obtained by the scientific community.

I underline the fact that during my research activity, in particular regarding the samples preparation, I had to start from the very beginning in projecting and developing the production procedures, as in my reference laboratories the preparation of iron-based samples had never been managed nor achieved before. It is also for this reason that, among the fabrication routes that I attempted for the preparation of superconducting sample of family 11, only few lead in the end to satisfactory results, intending with this that only few roads lead to the development of samples which shows bulk superconductivity that can be confirmed by physical, structural and compositional measurements. The reason of most of the failures faced in the production of good superconducting samples can be ascribed to the technical hitches and the complexity of some of the procedures, to the difficulties in handling the materials and the instrumentation and also to the inexperience in these kind of manipulations with which I had to deal at the beginning of my work. For sake of completeness, a short description of all the attempted fabrication techniques are included in this Chapter. In the following Chapters and in the discussions I will focus on the comparison among the results obtained with these different techniques and of course on the results obtained by the best performing samples, with the aim of correlate the materials' structure to the superconducting properties.

As anticipated in Chapter 1, FeSe is composed only of FeSe layers with an anti-PbO-type structure (space group P4/nmm), and theoretical studies [1] indicated the similarities in the electronic states between Fe-chalcogenides and Fe-As-based superconductors. These natures common to the Fe-As-based superconductors have made Fe chalcogenides a key system to elucidate the mechanism of Fe-based superconductivity. 11 family is appealing not only for the high magnetic critical fields

but also for the reduced toxicity of its constituents compared to As, and moreover is expected to be suitable for high field applications since it clearly shows a weak dependence of the critical current density $J_c$ on the applied magnetic field [2], [3].
In this Chapter, Fe-Se and Fe-Te binary phase diagrams are shown at the very beginning. These phase diagrams are the starting point for the production of the samples of the family 11 and for understanding their behaviour in terms of physical properties. Then the samples preparation routes learned and implemented during this work of Thesis will be described in details. In particular it will be described: the electrochemical synthesis of iron based superconductor FeSe film, the polycrystalline FeSe solid state synthesis, the polycrystalline FeSeTe solid state synthesis, the FeSeTe solid state synthesis aided by high energy ball milling of precursor powders and the FeSeTe synthesis by fusion. The structural and superconductive characterization of the prepared samples will be then shown in the following Chapters.

Regarding the manufacturing procedures managed and achieved during this PhD work, I'm pleased to underline that I had the possibility to visit the National Institute for Materials Science (NIMS) laboratories of Tsukuba in Japan during the PhD, and in particular I was at the Nano Frontier Materials Group, which is under the leadership of Prof. Dr. Takano. There, I also had the opportunity to meet Dr. Demura, who showed me in person the procedure that he optimized for the electrochemical synthesis of FeSe superconducting films. At NIMS, I also had the chance to learn the fundamental basis for the preparation of FeSe and FeSeTe superconducting samples starting from the precursors powders by means of solid state reactive sintering and melting techniques respectively.

During this years I also had the chance to visit the laboratories of CNR-INFM-LAMIA and the physics and chemistry departments at Università di Genova, where I could see the work of expert researchers in the production and the characterization of iron-based samples.

These experiences were important and formative in view of my objective of developing manufacturing processes of iron-chalcogenides superconducting samples and, even if I did not reproduce exactly the procedures that I saw in Japan and at Genova, the know-how that I gained was exploited in the set up of the laboratories in which I produced the superconducting samples.

In the last paragraph of this Chapter, the main measurement systems used for the structural, the magnetic and the transport characterization of the prepared samples will be shortly described. It will be also given an indication regarding measurements concerning each of the prepared samples.

## 2.1 Fe-Se and Fe-Te binary phase diagrams

Fe-Se and Fe-Te are similar multi-phase systems, with partial reciprocal solubility. Elemental Se, Te and Fe melting and boiling temperatures are shown in Table II-1.

| | Se | Te | Fe |
|---|---|---|---|
| Melting point (°C) | 221 | 450 | 1538 |
| Boiling point (°C) | 685 | 988 | 2862 |

Table II-1: Se, Te and Fe melting and boiling temperatures.

One of the reasons why the production of the superconducting samples of this family is not straightforward, even if the chemical composition is quite easy is the large difference between the melting and the boiling temperatures of the precursors, which compels the use of synthesis in vacuum in most cases. The Fe-Se phase diagram shown in Figure 1 has been adopted in its main features from a publication by Schuster *et al.* [4], who constructed the phase boundaries from their own investigations in the region 20-66 at. % Se and from data published by other investigators. Two liquid miscibility gaps, two compounds, namely tetragonal $\beta(Fe_{1.04}Se)$ and orthorhombic $\varepsilon(FeSe_2)$, and several $Fe_{1-x}Se$ (NiAs related structures $\delta$, $\delta'$, $\gamma$, $\gamma'$) were observed. The Fe-rich hexagonal $\delta$–phase transforms to a high temperature modification $\delta'$ of unknown structure, and undergoes a $\lambda$–transformation to the monoclinic $\gamma'$ phase. Below 750°C the monoselenide $\beta(Fe_{1.04}Se)$ exists between 49.0-49.4 at.% Se. It decomposes peritectoidally at 457°C [5] and crystallizes with the tetragonal PbO-structure. Values for the lattice constants reported by [4] ($a$ = 0.3775 nm and c = 0.5527 nm). The $Fe_{1-x}Se$ phases having NiAs-related structures have an extended range of homogeneity. Samples quenched from 380°C and 550°C, respectively, and investigated by X-ray analysis contain hexagonal $\delta$–phase in the range 51.5-53.5 at. % Se and 51.5-54.3 at. % Se respectively.

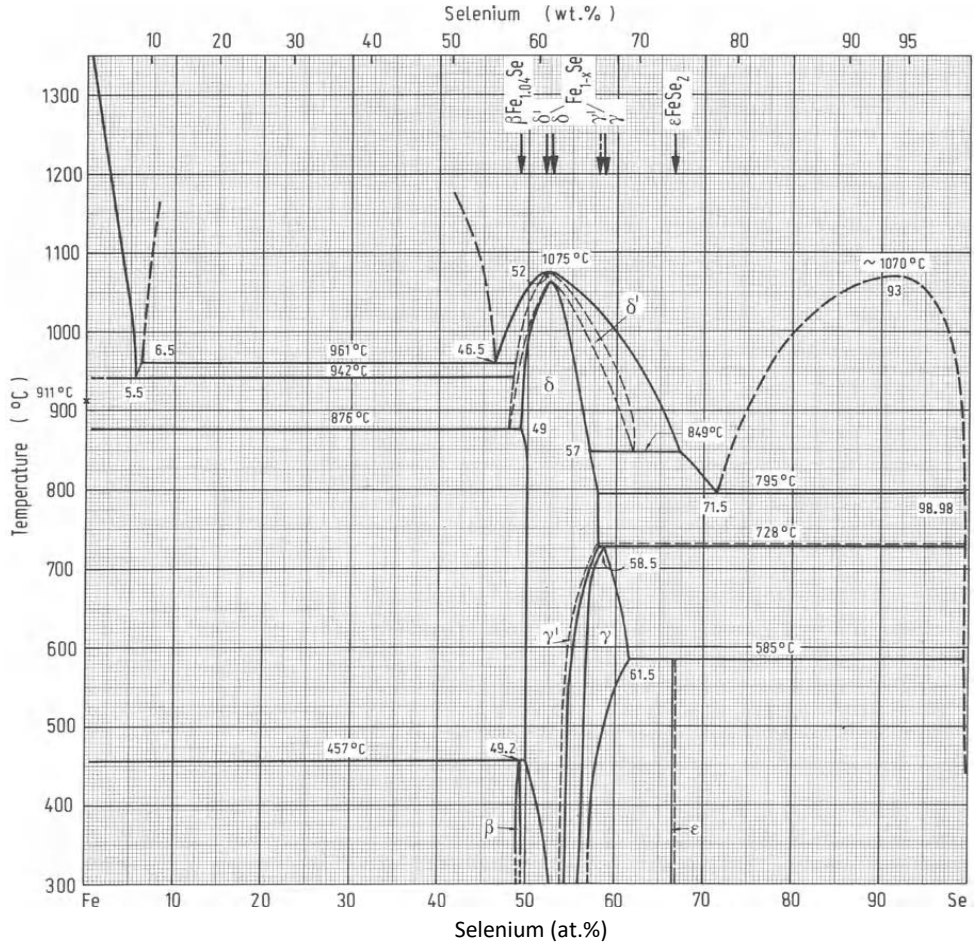


Figure 1: Fe-Se binary phase diagram, reproduced from Kubaschewski [7].

Above 750 °C, according to [4] and [6] the Fe-rich region is characterized by three invariant equilibria at higher temperatures. A monotectic at 961 °C and 46.5 at. % Se, a eutectic at 942 °C and 5.5 at. % Se and a eutectoid at 876 °C. The Se-rich region is marked by a eutectoid at 849 °C, a monotectic at 795 °C and 71.5 at. % Se [4], [6] with a miscibility gap extending from 71.5- 98 at. % Se [4], 71.5-99 at.% Se and 73.9-99.98 at. % Se respectively. The hexagonal δ–phase changes to a high-temperature modification δ' of undetermined structure at 52.8 at. % Se and a transformation temperature of 1065 °C. The congruent melting point of δ' has been observed at 52.0 at.% Se and 1075 °C.

The Fe-Te phase diagram in Figure 2 is based entirely on experimental results critically assessed in a systematic study of various investigations by Ipser et al. [8]. The system contains four 'compounds', $FeTe_{0.9}$ (β and β' tetragonal and rhomobohedral respectively), $FeTe_{1.2}$ (γ), δ and δ' a monoclinically distorted and a hexagonal NiAs phase respectively, and FeTe2 (ε) with an orthorhombic structure. A general investigation of the system was undertaken by [8]. They used thermal, X-ray and isopiestic measurements of alloys prepared from 99.9 % Fe and 99.99% and 99.999% Te. Samples were heated for 15 hours at 900-1000 °C, annealed 1-3 week

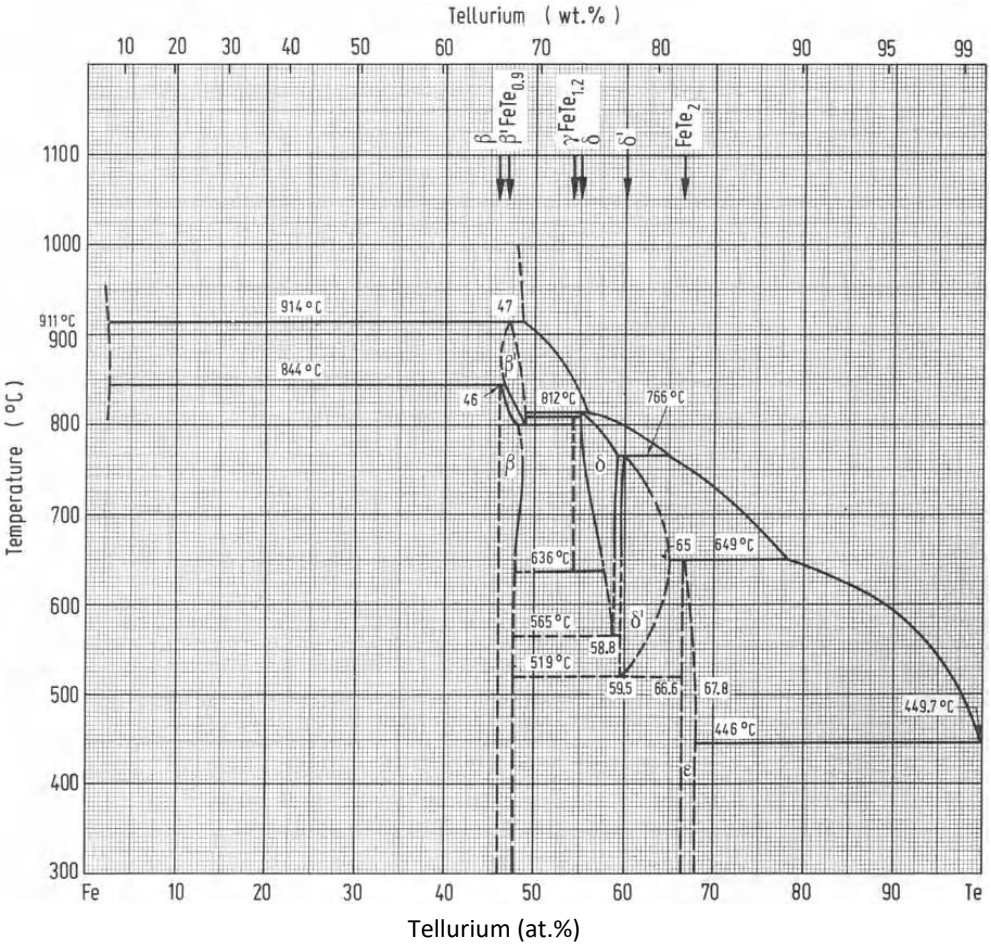


Figure 2: Fe-Te binary phase diagram, reproduced from Kubaschewski [7].

at 600-800 °C and furnace cooled. Samples prepared for X-ray measurements were sealed under vacuum in quartz ampoules, heat-treated and quenched in ice water.
Their results are represented in Figure 2. β($FeTe_{0.9}$) tetragonal is stable from room temperature to 844 °C where it decomposes - probably by peritectoid reaction - into α-Fe and the high-temperature phase β'. However, it is possible that the reaction at 844 °C is eutectoid with a congruent transformation point between β and β'. β shows a maximum range of homogeneity at 750 °C of about 2.5 at.% Te. The solid solubility of Te in Fe has not been accurately determined but appears to be small. According to X-ray measurements, a sample of about 1.5 at. % Te equilibrated at 830 °C showed the lattice parameter identical to that of pure α(Fe).

## 2.2 Electrochemical synthesis of iron-based superconductor FeSe films

The electrochemical synthesis of FeSe films has been developed by Dr. Satoshi Demura *et al.* from the National Institute of Material Science (NIMS) of Tsukuba in Japan (Demura at that time was also with University of Tsukuba and JST-TRIP Tsukuba, Japan) and is described in [9],[10]. Respect to the first of the two works, dated 2012, in the second one, published in 2013, Dr. Demura has optimized the electrochemical procedure.
The whole process of electrochemical deposition can be roughly divided in three steps. The first one is the preparation of the electrolyte, obtained dissolving into distilled water, $FeCl_2 4H_2O$ 0.03 mol/l, $SeO_2$ 0.015 mol/l and $Na_2SO_4$ 0.1 mol/l. The different reagents have to be weighted with high accuracy (± 0.0002 g) and soon poured into distilled water, while the solution is stirred slowly all the time. The pH of

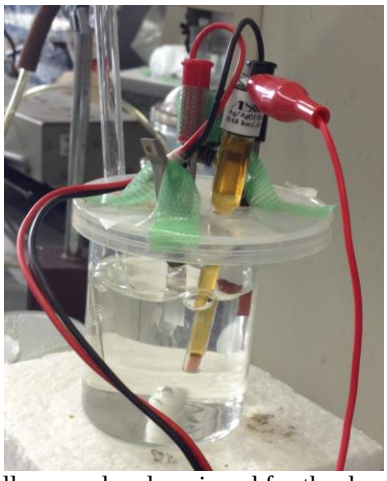

Figure 3: The electrochemical cell covered and equipped for the deposition.

the solution has to be adjusted with a solution of distilled water and $H_2SO_4$, as for FeSe deposition a pH of 2.1 is needed. During the experiment, the temperature of the solution should remain the same, because the pH changes with temperature, even if for variations of 1 or 2 degrees the changes are negligible.
The second step consists in the preparation of the electrochemical cell. The electrochemical depositions are performed by a three-electrode method, where the positive electrode (the counter) is made in platinum, the negative (working) electrode in iron and the differential (ground) electrode is silver chloride (Ag/AgCl). The

positive and the negative electrodes have both dimensions of 2.5x1 cm with a thickness of 0.15 mm and during the electrochemical deposition should be immersed in the solution for 1 cm.
The third step consists in the deposition itself. The voltage difference between the differential electrode and the negative electrode must remain constant during the whole process. This is achieved by means of the Toyo VersaSTAT test software (TVT) that controls the voltage supply and adjust the voltage difference between the Pt electrode (which only has the task of supplying electrons) and the differential electrode. The solution is covered and has to be slowly stirred during the whole process while a nitrogen very slow flow is supplied inside the electrochemical cell. The synthesis is performed at constant voltage for 60 minutes. Demura *et al*. [10] have shown that superconducting tetragonal FeSe is obtained if the voltage difference during the deposition is kept at -0.9 V, but other voltage differences can be tried as well. The composition of the film can be in fact controlled by the synthesis voltage. After the deposition the pH of the solution is measured again and should remain unchanged. FeSe has been electrochemically deposited on the Fe electrode. In Figure 3 a photo of the electrochemical cell filled with the solution and equipped with electrodes and connections is shown.
This method of fabrication has been attempted because, in principle, it may be an innovative and cheap method for the fabrication of superconducting FeSe film, wires, tapes, and coatings.

## 2.3 Polycrystalline FeSe from solid state reactive sintering

After the discovery of 11 system, several groups have optimized the preparation of samples, investigating on the stoichiometry and on the solid-state synthesis procedures [11]–[22]. Beside the importance of single crystals preparation, crucial for studying the correct phase devoid of impurities and for better understanding the underlying mechanisms, for technological applications, especially for fabrication of superconducting wires and tapes, samples are usually made in polycrystalline bulk or thin-film form, and their properties need to be understood and enhanced. From literature we know that polycrystalline FeSe samples contain two major phases: tetragonal $\beta$-FeSe phase (P4/*nmm*), composed of stacks of edge-sharing $FeSe_4$-tetrahedra layer by layer, and hexagonal $\delta$-FeSe ($P6_3/mmc$). Beside these two phases, minor phases such as monoclinic $Fe_3Se_4$, ferromagnetic hexagonal $Fe_7Se_8$, elemental Se or Fe, iron oxides or other impurities can be found inside samples, if the fabrication procedure has been somehow defective [23].
There is large scientific and technological interest in developing simple and reproducible procedures for obtaining samples containing $\beta$-FeSe phase with very few impurities and bulk superconductivity, therefore solid state synthesis techniques are still of great actuality.
The synthesis of FeSe powders and pellets required several steps, starting from stoichiometric quantities of freshly polished powder shots. The powders were mechanically machined inside a mortar, then were loaded into cleaned and dried silica tubes and afterwards sealed under vacuum at $2 \cdot 10^{-2}$ Pa. These tubes were then placed in a furnace, where they underwent a specific heat treatment (HT) at 680 °C for 12 hours before being quenched or cooled slowly inside furnace. After a first HT, powders were mechanically machined again and then reduced into pellets of 8 mm diameter applying a pressure of 9 MPa. The pellets where sealed into an evacuated

quartz tube at $2 \cdot 10^{-2}$ Pa for a second HT, identical to the first one. One of the pellets underwent a third HT inside an evacuated quartz tube at 700 °C for 10 hours.
The choice of the HTs has been based on the recipes found in literature for this

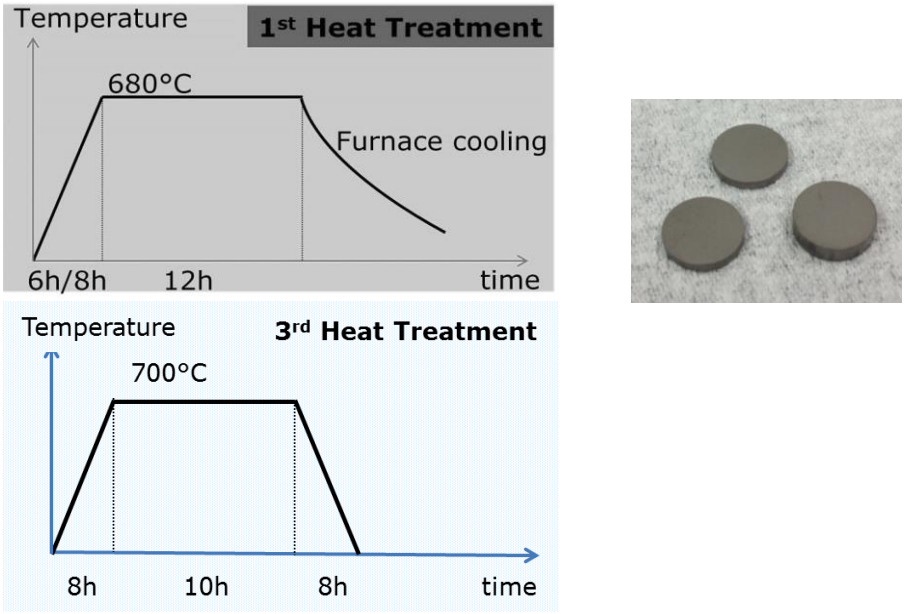


Figure 4: HTs profiles for the solid state synthesis of polycrystalline FeSe samples. On the right hand side three FeSe pellets of 8 mm diameter, produced by solid state sintering are shown.

material. In particular I referred to the works of Mizuguchi *et al.* [19], Hsu *et al.*[20] and Gabarino *et al.* [24], in which the powders are grinded and heat treated in severals steps at temperatures between 680 °C and 700 °C.

## 2.4 Polycrystalline FeSeTe from solid state reactive synthesis

Many experimental and theoretical studies have tried to optimize the superconducting iron chalcogenides preparation focusing on Te concentration [13],[25],[26] and on the chemical addition [27],[28]. Other investigations have been carried out in order to reveal the effect of the processing temperature during the fabrication procedure [15], [17],[23],[29],[30], which also plays an essential role in optimizing the synthesis technique, in understanding the mechanism of superconductivity and in promoting the practical applicationn for iron-based superconductors [12],[31]-[33].

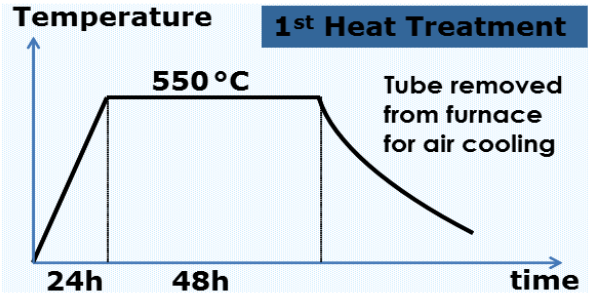


Figure 5: HTs profiles for the first step of the solid state synthesis of all polycrystalline FeSeTe samples.

I synthesized several samples in the nominal composition $FeSe_{0.5}Te_{0.5}$ through a two-steps solid-state reaction route. Stoichiometric quantities of Fe (99.99%), Se (99.99%) and Te (99.99%) powders were prepared and well mixed by manually grinding in an agate mortar. The selected temperature for the first heat treatment (HT) was 550 °C for 48 hours for all samples, and all FeSeTe samples were sealed under vacuum at $2 \cdot 10^{-2}$ mbar into dried silica tubes during treatments. At the end of the first HT the samples in the silica tubes were removed from furnace for air cooling, as shown in Figure 5. The reacted samples were reground into fine powders and then cold pressed into pellets. All samples were sealed under vacuum into dried silica tubes for the second HT as well.

For the second HT different routes were followed:

- some samples were ramped quickly to 650 °C and kept at this temperature for 17 hours, then the temperature was ramped down quickly (200 C°/h) to ambient temperature.
- some samples were ramped quickly to 750 °C and kept at this temperature for 17 hours, then the temperature was ramped down quickly (200 C°/h) to ambient temperature.
- a group of samples were ramped quickly to 800 °C and kept at this temperature for 17 hours and then ramped to 400 °C at 30 °C/h and kept at this temperature for 4 hours, then the samples in the silica tubes were removed from furnace for air cooling.

These HTs' profiles are shown in Figure 6 a), b) and c) respectively.

In Chapter 4 the behaviour of samples belonging to each group will be shown. It is anticipated that samples belonging to the same group behave in very similar ways and for this reason only 1 sample for each group is shown in the following. The samples chosen for each group are respectively called FST650, FST750 and FST800.

The choice of the nominal composition and of the Se/Te ratio has been based on the results obtained by the scientific community, which almost unanimously agrees upon the fact that the $FeSe_{0.5}Te_{0.5}$ composition gives the best results in terms of superconductive properties, being at the centre of the interval of maximum $T_c$ and being also the easiest to prepare [13],[26],[29],[30].

The choice of the HTs has been done based on literature examples and results [13], [17],[23],[27]-[30], with the aim of obtaining good samples possibly in the easiest way from the manufacturing point of view. Each step of the preparation and each manipulation in fact conceal several tricks, especially concerning the purity of the composite. Precursors powders are in fact very reactive with oxygen, which subtracts Fe to the stoichiometry of the mixture and creates agglomerates at grain boundaries, as it will be shown in Chapter 4 when discussing the morphology of some of the measured samples. So, each time that a sealed quartz tube is opened for the preparation of the subsequent step, there is the severe risk of compromising the purity of the composite; for this reason the simplicity should be considered as one of the leading aspects in the choice of the process to be adopted.

Regarding the choice of the HT temperature of 800 °C, as it is close to the melting temperature of FeSeTe composite, I was interested in the observation of the behaviour of the composite as approaching this limit. In particular the reason why, for the last group of samples, it was chosen to hold the temperature at 400 C° for 4

hours after the slow cool down, can be ascribed to the intention of verifying if this could have helped the homogenization of these samples. In literature, in fact [29], [30], it has been evidenced that the composition of sintered Fe($Se_{1-x}Te_x$) phase is non-homogeneous, and this phenomenon has been related to a thermodynamic instability of the Fe($Se_{0.5}Te_{0.5}$) composition at 800 °C. As will be shown in Chapter 4, the results obtained indicate that the additional step at 400°C does not bring homogenization, maybe also because of its short duration (usually in literature final

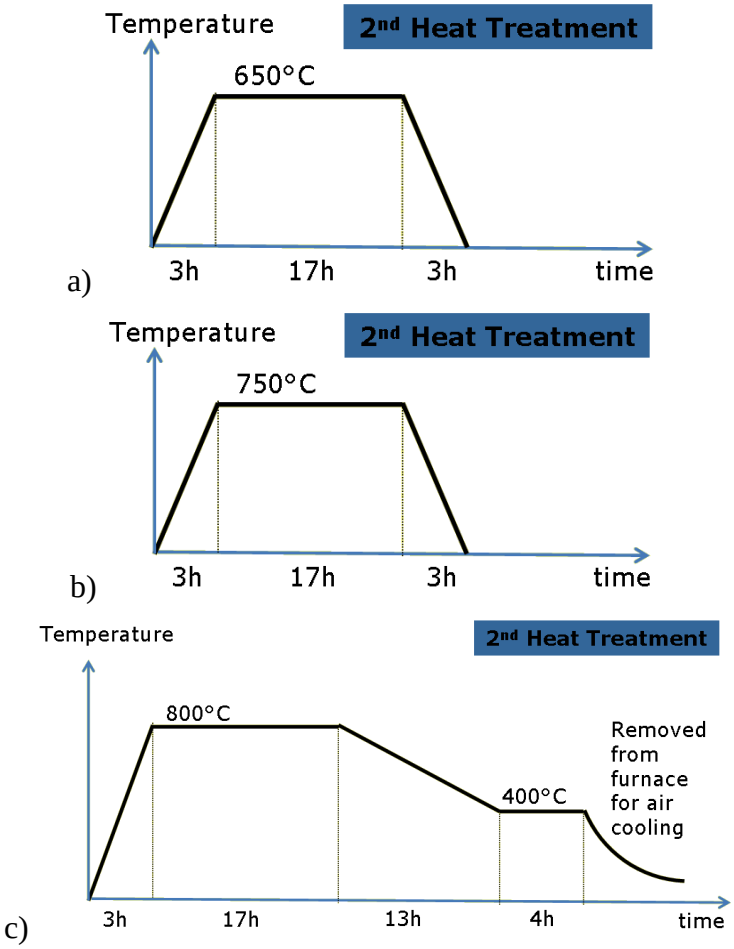


Figure 6: HTs profiles for the second step of the solid state synthesis of polycrystalline FeSeTe samples as described in the text.

annealing processes are much longer [29]).

## 2.5 Polycrystalline FeSeTe from mechano-chemical synthesis

This technique for the manufacture of FeSeTe sample was arranged in the laboratories of ENEA Casaccia Laboratories (*SSPT-PROMAS*). Details on High Energy Ball Milling (HEBM) technology can be found in the first paragraph of Appendix 1 and in the reference therein.

It is well known that HEBM can aid the sintering process of powders in metallurgical manufacturing process of many compounds and materials, and this method has been applied with success to FeSe as well, as can be found in literature [34]–[39]. Fewer

examples regarding ball milling applied to FeSeTe can be found in literature, in particular only one as far as I know, which regards the combination of mechanical alloying and solid-state reaction applied in order to synthesize bulk $FeSe_{0.5}Te_{0.5}$ superconductor [40]. In this work the mechanical alloying processes improved the density of the specimens and also affected morphologies and superconductivity, but the milling was very gentle, pretty much as a blending, and the results very poor from the superconductive point of view. Such a low energy milling, anyway, is not comparable to the HEBM that I applied to my samples.

I used elemental Fe (99.99%), Te (99.99%) and Se (99.99%) as precursors and mixed them in stoichiometric quantities for the nominal composition $FeSe_{0.5}Te_{0.5}$, for the same reasons explained in paragraph 2.4. The HEBM experiments were conducted into a SPEX 8000M mixer mill (SPEX SamplePrep, Metuchen, NJ), using cylindrical steel vials (60 $cm^3$ volume) and balls (10 mm diameter). The powder to ball weight ratio was fixed to 1:10. Each milling experiment consisted in:

a) loading the vial with 2 grams of powder mixture and in sealing it in vacuum atmosphere

b) mechano-chemical treatment of the powder mixture for selected milling time

c) recovering of the milled sample

Powders underwent 10 hours milling and were successively compacted in pellets of 5 mm diameter; some of them were sintered with subsequent heat treatments. In Chapter 4, I will show the results obtained with structural and superconductive characterization for 2 representative samples obtained by mechano-chemical synthesis. The first one was straightforward obtained by compaction of the 10 hours milled powders and will be called HEBM10. Regarding the second one, the powders underwent 10 hours of HEBM, and were then recovered and compacted into pellets; the pellets were sintered at 700 °C for 24 hours under vacuum at $2 \cdot 10^{-2}$ mbar in doubled sealed quartz vial. The sample obtained with this procedure will be called HEBM10-700.

## 2.6 FeSeTe from fusion

Several samples were synthesized from fusion of Fe, Se and Te precursors powders. These melted samples were all obtained starting from the nominal composition $FeSe_{0.5}Te_{0.5}$ for the same reasons explained in paragraph 2.4. Stoichiometric quantities of Fe (99.99%), Se (99.99%) and Te (99.99%) powders were prepared and well mixed by manually grinding in an agate mortar. The selected temperature for the first heat treatment (HT) was 550 °C for 48 hours for all these samples, and all samples were sealed under vacuum into dried silica tubes at $2 \cdot 10^{-2}$ mbar during treatment. At the end of the treatment the samples in the silica tubes were removed from furnace for air cooling.
The reacted samples were reground into fine powders and then cold pressed into pellets. All samples were sealed under vacuum into dried silica tubes for the second HT as well. The second HT for these samples was obtained going to temperatures beyond 800 °C, which is about the melting temperature of the composites. Among the several samples that I produced by melting, I will report on two samples in particular,

which belong to the group of the best performing ones and which were obtained applying the following second HT respectively:

- sample named FST970: the furnace was ramped quickly to 970 °C and kept at this temperature for 17 hours and then ramped to 400 °C at 30 °C/h, then it was quickly cooled to room temperature.
- sample named FST970B: the furnace was ramped quickly to 970 °C and kept at this temperature for 17 hours and then ramped to 400 °C at 10 °C/h, then it was quickly cooled to room temperature.

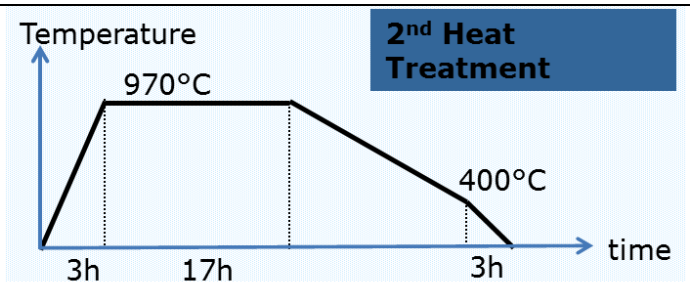


Figure 7: HTs profiles for the second step of the synthesis of polycrystalline FeSeTe samples by fusion as described in the text.

The HT profile is sketched in Figure 7. It is clear that the only difference in the fabrication of the two samples is in the velocity of the cooling ramp from the melting temperature to 400 °C in the second heat treatment. It is during the cooling ramp that the crystallisation of the melted composite happens, and in principle the slower is the ramp, the larger will be the grains and more the sample will resemble the single crystal structure, with a preferential orientation given by plane of growth.
The choice of the heat treatments for these sample has been done in order to evidence the possibility of removing spurious phases between grains during the fusion process, and this is confirmed by the morphology of the two samples in the SEM images, when compared to the samples obtained by solid sate sintering, as will be show in Chapter 4. It will be also seen that this apparently negligible difference in the HT brings remarkable differences in the superconducting behaviour of these samples.

## 2.7 Measurement systems used in this work of thesis

### 2.7.1 XRD measurements

X-ray diffraction spectra of all FeSe samples (powders scratched from the deposited films and samples obtained from solid state reactive sintering) and of FeSeTe samples referred to as FST550, FST650, FST750 and FST970 were performed in the Superconductivity laboratories at ENEA C.R. Frascati. Measurements were performed in the Bragg-Brentano geometry using a Rigaku SmartLab diffractometer with a 9 kW rotating anode. The diffractometer was equipped with a primary monochromator giving CuK$\alpha$1 radiation, a Johansson's Ge crystal, and a secondary graphite monochromator to remove Fe fluorescence.

Room-temperature X-Ray diffraction analysis (XRD) on FeSeTe samples obtained by mechano-chemical synthesis were carried out at ENEA C.R. Casaccia (*SSPT-*

*PROMAS*) laboratories, on a SEIFERT PAD VI diffractometer (Rich. Seifert & Co., Ahrensburg, Germany), equipped with $MoK_\alpha$ radiation and a LiF monochromator on the diffracted beam.
Structural analysis on FeSeTe samples referred to as FST800 and FST970B was carried out at Master Lab. of CNR-SPIN Salerno and Physics Department of Salerno University by means of a X-ray diffractometer Rigaku DMax-2500 with $CuK_\alpha$ radiation on selected samples.

### 2.7.2 SEM imaging

SEM images of the surface of FeSe pellets obtained from solid state reactive sintering after second and third HTs and of samples referred to as FST550, FST650 and FST970 were performed in the Superconductivity laboratories at ENEA C.R. Frascati. The measurements system is a HR-FEG-SEM Leo 1525 with in-lens secondary electron and aperture size 30 $\mu$m.

SEM micrographs for samples obtained by mechanochemical synthesis were performed at ENEA C.R. Casaccia (*SSPT-PROMAS*) laboratories with a Fe-SEM LEO 1530 with in-lens secondary electron.

SEM micrographs for samples referred to as FST800 and FST970B were acquired at Master Lab. of CNR-SPIN Salerno and Physics Department of Salerno University with a LEO EVO 50 SEM.

### 2.7.3 EDX analysis

The chemical compositions of the two FeSeTe samples referred to as FST800 and FST970B have been determined by EDX analysis at Master Lab. of CNR-SPIN Salerno and Physics Department of Salerno University, selecting a grid of 50 points on areas of about 1.5 mm x 1 mm and performing a statistical calculation of each element content while the final compositions are given as an average.

The chemical composition of the FeSeTe sample referred to as FST970 has been determined by EDX analysis in the Superconductivity laboratories at ENEA C.R. Frascati, averaging on areas of about 1.4 mm x 1 mm.

### 2.7.4 Transport measurements

The resistance measurements of FeSe samples obtained from solid state reactive sintering after second and third HTs and of FeSeTe samples referred to as FST500, FST800 and FST970B were performed at Master Lab. of CNR-SPIN Salerno and Physics Department of Salerno University with a Cryogenic Ltd. cryogen free cryostat, equipped with an integrated cryogen-free variable-temperature insert, operating in the range 1.6–300 K, and a superconducting magnet able to generate a field up to 16 T. These measurements have been performed by a standard 4-probe technique. A Source-Meter Keithley model 2430 has been used as current source, while the voltage has been measured by a Keithley Nanovoltmeter model 2182. Each voltage value is the result of an offset-compensated measurement, where the final voltage is obtained by mediating on the values related to the current biases with equal

intensity and opposite sign. The temperature has been measured by a LakeShore Cernox sensor model CX-1030-SD-1.4L via a LakeShore Temperature Controller model 350. The Cryogenic Ltd. facility is shown in Figure 8.

The resistance measurements of FeSe samples obtained from solid state reactive sintering after second HT and of sample referred to as FST970 were performed also in the Superconductivity laboratories at ENEA C.R. Frascati in a Oxford He gas flow cryostat. In this system the sample under measurement is shielded from direct exposure of the cooling He gas flow by means of a copper box. A four-point technique has been applied for the resistance measurement, by means of a Keithley

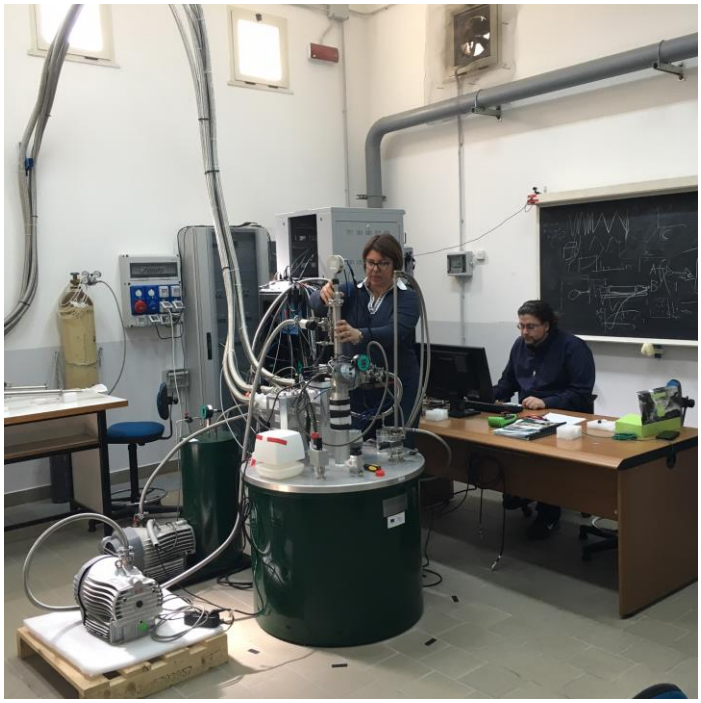

Figure 8: Cryogenic Ltd. cryogen free cryostat for transport and calorimetric measurements up to 16 T at Master Lab. of CNR-SPIN Salerno and Physics Department of Salerno University.

(a) (b)

Figure 9: ENEA C.R. Frascati, Oxford He gas measurement system for transport measurements up to 12 T. (a) acquisition rack (b) cryostat

high precision current supply, coupled to a Keithley nanovoltmeter for the voltage signal. The resistance vs. temperature curves are obtained by ramping the temperature from 20 K to 4.2 K at different magnetic fields, from zero up to 12 T.

The temperature is measured through a Cernox thermometer attached to the copper sample holder. The critical current measurements have been obtained from voltage-current curves by adopting the 1 μV/cm criterion. This measurement system is shown in Figure 9.

### 2.7.5 Magnetic measurements

The magnetic measurements of FeSe samples obtained from solid state reactive sintering after second HT were performed at the Physics Department of Salerno University. The sample magnetization *M* was measured as a function of temperature *T* in DC magnetic field by means of a Quantum Design PPMS-9T equipped with a VSM (Vibrating Sample Magnetometer) option.

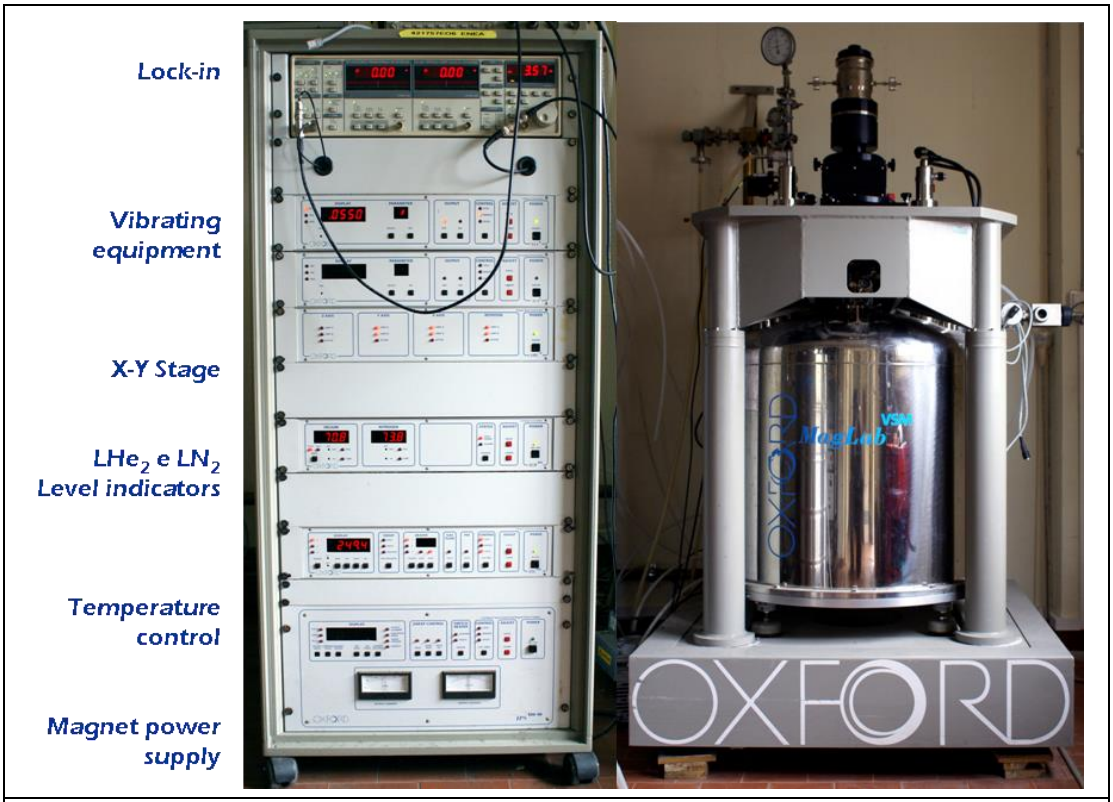


Figure 10: Image of the Oxford Instrument VSM facility at Superconductivity Laboratories, ENEA C.R. Frascati.

The magnetic measurements of FeSeTe samples referred to as FST500, FST650, FST750, FST800, FST970B, FST970 and of samples obtained by mechano-chemical synthesis were performed in the Superconductivity laboratories at ENEA C.R. Frascati by means of an Oxford Instrument VSM (Vibrating Sample Magnetometer) equipped with a 12 T magnet and He gas flow system (Figure 10). The system has a

maximum ramp rate of 1 T/min and a sensibility of the order of $10^{-6}$ emu and can work in the temperature range 4.2-300 K. The field uniformity zone is a sphere with 5 mm diameter. Concerning these measurements it worked with a frequency of 55 Hz and an amplitude of 0.2 mm.

Isothermal magnetization curves of FeSeTe sample FST970 were acquired in the Superconductivity laboratories at ENEA C.R. Frascati also by means of a Cryogenic Ltd. with a cryo-free 18 T superconducting magnet and VSM measurement option. The system is shown in Figure 11. The operating magnet has central field homogeneity of 0.5% over 10 mm diameter x 10 mm long cylinder. The temperature range is 2.2 – 100 K with a temperature stability of ±0.05 K. The sample chamber has 14 mm inner diameter.


Figure 11: Cryogenic Ltd. cryogen free cryostat for transport and magnetic measurements up to 18 T at Superconductivity Laboratories, ENEA C.R. Frascati.

## 2.7.6 Calorimetric measurements

Calorimetric measurements of FeSeTe sample FST970 were performed at Master Lab. of CNR-SPIN Salerno and Physics Department of Salerno University with a Cryogenic Ltd. cryogen free cryostat, as described in paragraph 2.7.4. The heat capacity probe uses integrated sensors to measure the heat capacity of small samples by employing the alternating-current (AC) calorimetry method. The sensors are made on a silicon –nitride-free-standing membrane with a typical thickness of 1 μm. The method is based on detecting oscillations of the sample temperature in response to the oscillating heat power supplied to the sample. The power is produced by driving an AC current (at a frequency F) through a resistive heater. The resulting power has a

steady (DC) component and an oscillating part at a frequency 2F [41],[42]. The temperature is measured by six thermocouples connected in series. The temperature is also oscillating at 2F, with a phase shift respect to the power. The signal from the thermocouples is measured by a lock-in amplifier, therefore the amplitude and phase

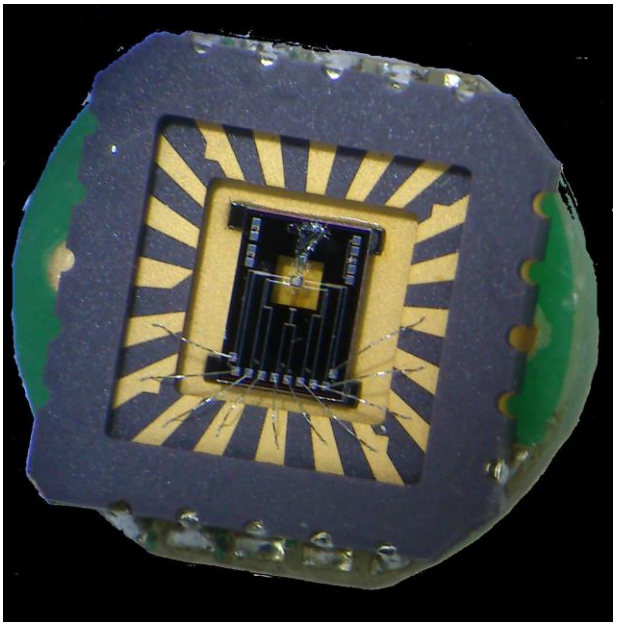

Figure 11: Sample FST970 in the heat capacity gauge.

are detected simultaneously. These values, together with an independently measured heater power, are used to calculate the heat capacity. In Figure 11 an example of sample in the heat capacity gauge is presented.

## References


[1] Subedi A., Zhang L., Singh D. J. and Du M. H. (2008) Density functional study of FeS, FeSe, and FeTe: Electronic structure, magnetism, phonons, and superconductivity *Phys. Rew. B* 78 134514.

[2] Belingeri E. *et al.* (2012) Strong vortex pinning in $FeSe_{0.5}Te_{0.5}$ epitaxial thin film *Appl. Phys. Lett.*, vol. 100, , Art. no. 082601

[3] Si W. *et al.* (2013) High current superconductivity in $FeSe_{0.5}T_{0.5}$-coated conductors at 30 tesla," *Nat. Communic*. 4:1347.

[4] Schuster W., Mikler H., Komarek K.L. (1979) Transition metal-chalcogen systems, VII.: The iron- selenium phase diagram *Monatsh. Chern.* 110 1153.

[5] Grønvold F. (1968) Heat Capacities and Thermodynamic Properties of the Iron Selenides $Fe_{1.04}Se$, $Fe_7Se_8$, and $Fe_3Se_4$ from 298 to 1050 K *Acta Chem. Scand*. 22 1219.

[6] Kullerud, G. (1969) Carnegie Inst. Wash. Year Book 67 175

[7] Kubaschewski O. (1982) Iron-Binary Phase Diagrams Springer-Verlag Berlin Heidelberg GmbH

[8] Ipser, H.; Komarek, K,.L.; Mikler, H. (1974) *Monatsh.Chern*. 105 1322

[9] Demura S. *et al.* (2012) Electrochemical synthesis of Iron-based Superconductor FeSe Films *J. Phys. Soc. Jpn.* 81 043702.

[10] Demura S. *et al.* (2013) Electrodeposition as a new route to synthesize superconducting FeSe *Solid State Communications* 154 pp. 40-42.

[11] Braccini V. *et al.* (2013) Highly effective and isotropic pinning in epitaxial Fe(Se,Te) thin films grown on $CaF_2$ substrates *Appl. Phys. Lett.*, vol. 103, Art. no. 172601.

[12]Palombo M. *et al.* (2015) Exploring the feasibility of Fe(Se,Te) conductors by ex-situ powder-in-tube method *J. Appl. Phys.*, vol. 117, , Art. no. 213903.

[13]Hacisalihoglu M. Y. and Yanmaz E. (2013) Effect of substitution and heat treatment route on polycrystalline $FeSe_{0.5}Te_{0.5}$ superconductors *J. Supercond. Novel Magn.*, vol. 26, pp. 2369–2374.
[14]Pimentel J. L., Jr., Serbena F. C., and Jurelo A. R. (2011) Characterization of $FeSe_x$ superconductor prepared by different thermal routes by instrumented indentation *J. Supercond. Novel Magn.*, vol. 24, pp. 1437–1441.
[15]Onar K. and Yakinci M. E. (2015) Solid state synthesis and characterization of bulk *β*-FeSe superconductors *J. Alloys Compounds*, vol. 620, pp. 210–216.
[16]Zhao P. H. *et al.* (2012) A simple fabrication of FeSe superconductors with high upper critical field *J. Supercond. Novel Magn.*, vol. 25, no. 6, pp. 1781–1785.
[17]Umeyama N. *et al.* (2010) Superconductivity on FeSe synthesized by various sintering temperatures *Phys. C, Supercond.*, vol. 470, pp. S518–S520.
[18]McQueen T. M. (2009) Extreme sensitivity of superconductivity to stoichiometry in $Fe_{1+\delta}Se$ *Phys. Rev. B*, vol. 79, 2009, Art. no. 014522.
[19]Mizuguchi Y., Tomioka F., Tsuda S., Yamaguchi T., and Takano Y. (2008) Superconductivity at 27 K in tetragonal FeSe under high pressure *Appl. Phys. Lett.*, vol. 93, Art. no. 152505.
[20]Hsu F. C. (2008) Superconductivity in the PbO-type structure alpha-FeSe *Proc. Nat. Acad. Sci. USA*, vol. 105, no. 38, pp. 14262–14264.
[21]Janaki J. *et al.* (2009) Synthesis, characterization and low temperature studies of iron chalcogenides superconductors *J. Alloys Compounds*, vol. 486, no. 2, pp. 37–41.
[22]Li Z. *et al.* (2010) Structural and superconductivity study on $\alpha - FeSe_x$, *J. Phys. Chem. Solids*, vol. 71, pp. 495–498.
[23] Fiamozzi Zignani C. *et al.* (2016) Fabrication and Characterization of Sintered Iron-Chalcogenides Superconductors *Trans. on Appl. Supercond* vol. 26 no. 3 7400105.
[24]Gabarino G. *et al.* (2009) High-temperature superconductivity ($T_c$ onset at 34K) in the high-pressure orthorhombic phase of FeSe *EPL* 86 27001.
[25]Yeh K. W. *et al.* (2008) Se and Te doping study of the FeSe Superconductors, *J. Phys. Soc. Jpn*., vol. 77, pp. 19-22.
[26]Fang M. H. *et al.* (2008) Superconductivity close to magnetic instability in $Fe(Se_{1-x}Te_x)_{0.82}$, *Phys. Rev. B*, vol. 78, 224503.
[27]Migita M. *et al*. (2013) Substitution effects of Ag into $FeSe_{0.5}Te_{0.5}$ superconductor," *Physica C Superconductivity*, 484, pp. 66-68.
[28]Nazarova E. *et al*. (2015) Improvement of the superconducting properties of polycrystalline FeSe by silver addition, *Supercond. Sci. Technol.*, vol. 28, , Art. no. 125013.
[29]Palenzona A. *et al.* (2012) A new approach for improving global critical current density in $Fe(Se_{0.5}Te_{0.5})$ polycrystalline materials, *Supercond Sci. Technol.*, vol. 25, Art. no. 115018.
[30]Chen N., Liu Y., Ma Z., Yu L., Li H. (2016) Improvement in structure and superconductivity of bulk $FeSe_{0.5}Te_{0.5}$ superconductors by optimizing sintering temperature, *Scripta Materialia*, vol. 112, pp. 152-155.
[31]Li Q., Si W., and Dimitrov I., (2011) Films of iron-calchogenides superconductors , *Rep. Prog. Phys*., vol. 74, Art. no. 124510.
[32]Massee F. *et al*. (2015) Imaging atomic-scale effects of high-energy ion irradiation on superconductivity and vortex pinning in Fe(Se,Te), *Sci. Adv*., 1e1500033.
[33]Haindl S. *et al*.(2014) Thin film growth of Fe-based superconductor: from fundamental properties to functional devices. A comparative review, *Rep. Prog. Phys*., vol. 77, 046502.
[34]Zang S. *et al.* (2015) Optimization of FeSe superconductors with high-energy ball milling aided sintering process, *J. Materiomics*, vol. 1, no. 2, pp. 118–123. Available: http://dx.doi.org/10.1016/j. jmat.2015.04.004.
[35]Ma Z., Dong M., and Liu Y. (2014) The sintering process and reaction kinetics of Fe-Se system after ball milling treatment, *J. Supercond. Novel Magn.*, vol. 27, no. 3, pp. 775–780.
[36]Li X., Ma Z., Liu Y., Dong M., and Yu L. (2013) The sintering process and superconductivity of polycrystalline milled Fe-Se, *IEEE Trans. Appl. Supercond.*, vol. 23, no. 2, Art. no. 7000405.
[37]Li X., Gao Z., Liu Y., Ma Z., and Yu L., "Influence of premilling time on the sintering process and superconductive properties of FeSe," *IEEE Trans. Appl. Supercond.*, vol. 22, no. 6, Dec. 2012, Art. no. 7300105.
[38]Xia Y., Huang F., Xie X., and Jiang M. (2009) Preparation and superconductivity of stoichiometric *β*-FeSe, *Europhys. Lett.*, vol. 86, no. 3, Art. no. 37008.

[39]Muralidhar M. *et al.* (2016) Improved critical current densities in bulk FeSe superconductor using ball milled powders and high temperature sintering, *Phys. Status Solidi* A, 1–7 / DOI 10.1002/pssa.201600299.

[40]Li X. *et al.* (2013) The microstructure and superconducting properties of $FeSe_{0.5}Te_{0.5}$ bulks with original milled powders, *Cryogenics*, vol. 57, pp. 50–54.

[41]Sullivan P.F. and Seidel. G. (1968) Steady-State, ac-Temperature Calorimetry *Phys. Rev.* 173 3 p. 679.

[42]Ventura G. and Perfetti M. (2014) *Thermal Properties of Solids at Room and Cryogenic Temperatures*, International Cryogenics Monograph Series, DOI: 10.1007/978-94-017-8969-1_2, © Springer Science+Business Media Dordrecht.

CHAPTER 3

# FeSe polycrystalline samples: structural and superconductive characterization

As anticipated, in this Chapter the characterizations carried out on the FeSe samples produced during the work for the Thesis are presented. Some samples have been characterized both from the structural and from the superconducting point of view. Other samples, on the other hand, were so poor from the point of view of the superconducting $\beta$-phase formation, that an extensive characterization was considered worthless.

## 3.1 FeSe from Electrochemical deposition

Several FeSe samples have been manufactured with the electrochemical deposition procedure described in paragraph 2.2.

Here only some of the measured xrd patterns have been selected to be shown, which are the most significant from the point of view of the research for the optimization of the procedure and of the formation of the tetragonal $\beta$-FeSe phase.

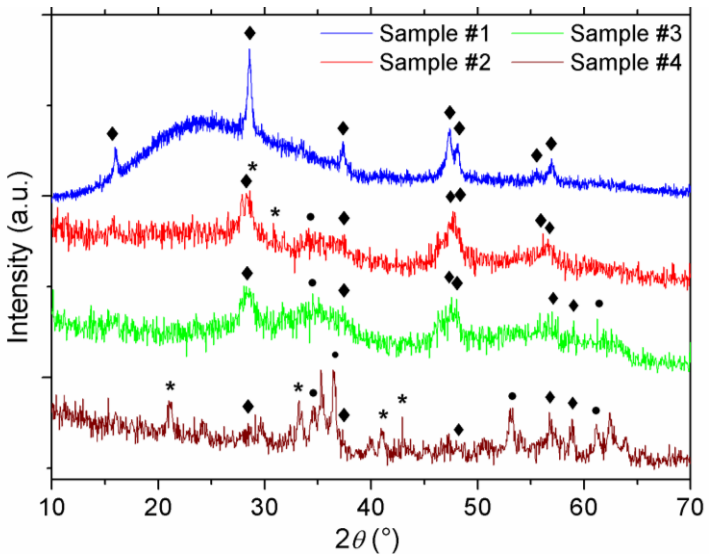


Figure 1: XRD measurements of four FeSe samples obtained with 1 hour electrochemical deposition synthesis, as described in Chapter 2. ♦ refers to $\beta$-FeSe phase, * to $\delta$-FeSe phase, and ● to other impurity phases, such as iron oxides, and selenium oxides. Patterns are shifted for an easy comparison.

As underlined by Demura in [1] and [2], the composition of films during the deposition on iron substrate can be controlled by the synthesis voltage. Another way of tuning the composition is increasing the pH of the solution, which returns in the increase of Se and in the decrease of Fe. Thus, the composition ratio of the electrodeposited film can be tuned also by the pH value.

Several combinations of synthesis voltage and pH of the solution have been tried with the aim of optimizing the procedure. In Figure 1 the XRD patterns for some of the produced samples are shown, together with the XRD pattern of the sample produced by Demura during my visit at NIMS with V=-0.9 V and pH=2.1, which is now named "Sample #1" and is inserted for comparison to show an example of a film with good crystallinity. The other curves in Figure 1 belong respectively to: "Sample #2", deposited with V=-0.9 V and pH=2.1; "Sample #3", deposited with V=-0.9 V and pH=2.2; "Sample #4", deposited with V=-0.75 V and pH=2.1.
From my experience, it can be concluded that the choice made by Demura and co-workers of retaining the applied voltage V=-0.9 V and pH=2.1 in the starting solution is the best one for obtaining the tetragonal superconductive FeSe $\beta$-phase. Anyway the procedure is quite complex and the obtained results were not very promising to incentivize further attempts and studies. As the patterns of all deposited samples, even the best ones, have low intensities and broad peaks, further analysis on these samples have been discarded.

## 3.2 Polycrystalline FeSe from solid state reactive sintering

In this paragraph the achievements obtained from sintering polycrystalline FeSe samples are presented. The synthesis of FeSe powders and pellets was obtained in several steps starting from stoichiometric quantities of freshly polished powders shots, following the procedures described in paragraph 2.3. Samples after first, second and third HTs were then characterized from the structural, transport, and magnetic points of view and the obtained results are discussed.

### 3.2.1 Structural Characterization: results and discussions

In order to have a look at the behaviour of prepared samples and to try to identify the present phases, X-ray diffraction patterns of the material after each HT were recorded at room temperature. In Figure 2 XRD patterns obtained on pellets after each HT are shown, together with the indication of the phases corresponding to the revealed peaks. The first HT promotes the formation of a mix of $\beta$-FeSe and $\delta$-FeSe phases. The lattice parameters of both the tetragonal and hexagonal phases are in good agreement with the literature. As reported in literature, FeSe samples prepared using solid state reaction method do not show single phase structure, and this can be linked to the large melting temperature difference between Fe (1521 ◦C) and Se (221 ◦C) [3],[4]. A certain amount of $\delta$-FeSe phase has been found by several other groups previously [3]–[10], and some of them also reported on the presence of other impurities such as iron or selenium oxides [3],[7]–[9], Se [3],[6], Fe [5], monoclinic $Fe_3Se_4$ phase [4] or iron silicide [8]. The remarkable presence of $\delta$-FeSe phase in XRD patterns is also consistent with what found in literature for $Fe_{1+x}Se$ when $x$ = 0 [9]-[11]. In our samples second and third HTs act on the relative content of the two main phases, and, due to possible oxygen contamination during preparation of samples, oxides and impurities formation is promoted. It was seen [10],[11], that obtaining almost pure $\beta$-FeSe phase requires low temperature (300–400 ◦C) final annealing, to complete the transformation of the hexagonal phase into the tetragonal one. In our case we cannot exclude that oxidation processes are guiding the hexagonal phase transformation, which may be depleted also in favour of impurities development.
SEM imaging of the pellets surface after second and third HT are shown in Figure 3 and in Figure 4 respectively. The surface of the sample after second HT shows grains

placed side by side with poor contact area. The grains dimension is in the range 1–3 $\mu$m. After third HT it is possible to distinguish two regions with very different

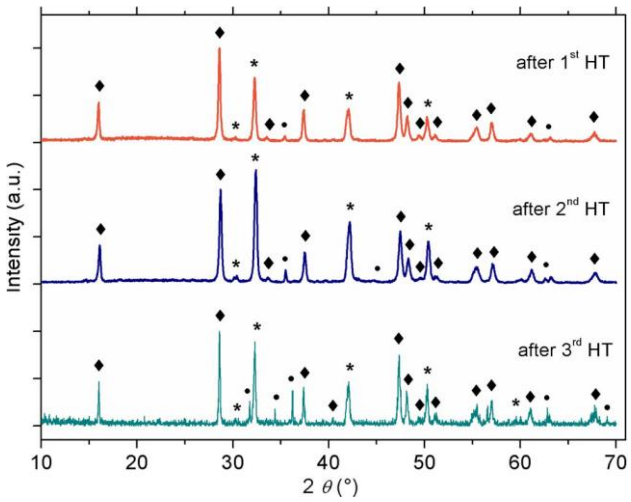


Figure 2. XRD measurements of FeSe samples after each of the three heat treatments. ♦ refers to $\beta$-FeSe phase, * to $\delta$-FeSe phase, and • to other impurity phases, including elemental Se, iron oxides, and selenium oxides. Intensities are normalized to the peak (101) of the $\beta$-FeSe phase and shifted for an easy comparison.

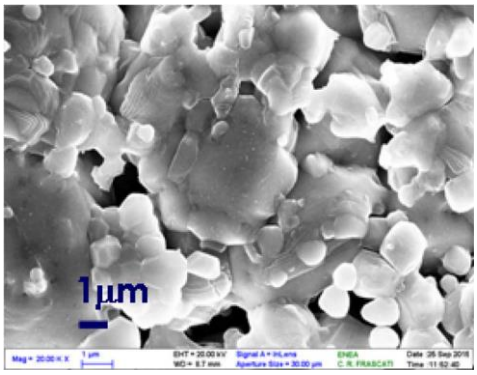


Figure 3: SEM image of FeSe pellet surface after second HT. Measurements system HR-FEG-SEM Leo 1525. In-lens secondary electron, aperture size 30 $\mu$m.

morphologies. Most of the sample shows zones characterized by a compact and homogeneous morphology composed by grains with dimension of 200–300 nm, as shown in Figure 4(b). These zones are surrounded by 1–2 $\mu$m large regions, with irregular and wrinkled morphology. The appearance of the sample after the third HT is quite different from SEM images of samples shown in literature for polycrystalline sintered FeSe, which usually have average grain size of few $\mu$m [3],[5], and a more isotropic aspect [4]. These differences could maybe be due to the HTs temperature that can promote a fine-grained morphology. In [6] it is shown that for HT's temperature of 800 ◦C and higher, apertures leading the diminution in contact area between grains appeared visible in SEM imaging.

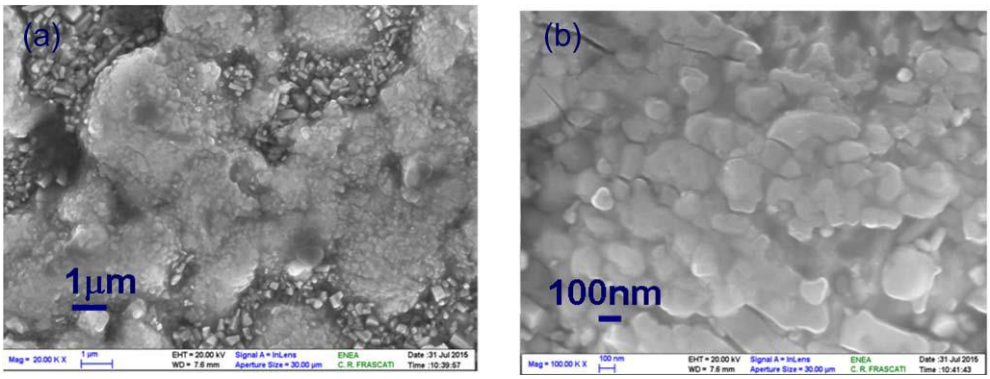


Figure 4. SEMimages at two magnifications of FeSe pellet surface after third HT. Measurements system HR-FEG-SEM Leo 1525. In-lens secondary electron, aperture size 30 $\mu$m.

### 3.2.2 Superconducting Properties: results and discussions

Beside structural characterization, superconducting properties of prepared samples have been investigated to monitor the samples quality corresponding to additional HTs. Superconductivity of FeSe pellet after second HT has been checked by means of transport and magnetic measurements, and the results are shown in Figure 5. After second HT the resistance versus temperature curve presents a clear superconducting onset at about 11 K; the transition is however very broad with a superconducting transition temperature ($T_{c0}$) valuable around 2.5 K at zero field.

The sample magnetization M was measured as a function of temperature $T$ in DC magnetic field by means of a Quantum Design PPMS-9T. Before each measurement as a function of the temperature, the residual trapped field inside the DC magnet was reduced below $10^{-4}$ Tesla by means of demagnetization cycles with a progressively decreasing field amplitude. The sample was warmed up and maintained well above the superconducting transition temperature for the necessary time to perform the cycles. This procedure is used to avoid magnetic field effects on the sample response [12].

As shown in Figure 5(b), the transition temperature is determined as the value of the temperature corresponding to the onset of the ZFC magnetization drop. Beside the strong ferromagnetic contribution, the curves show a diamagnetic onset at about 8.7 K, which is consistent with the values reported in literature for this material [4]–[6],[8],[10],[13]. The lack of complete diamagnetism below the onset of the transition can be attributed to the co-existence of both magnetism and superconductivity in the sample, due to ferromagnetic nature of Fe and ferri/ferromagnetism of $\delta$-FeSe phase and of the other impurities in the bulk of the sample, [4]–[6]. The magnetic irreversibility between the ZFC and FC curves, above the superconducting critical temperature, is also compatible with the presence of a ferromagnetic phase.

The diamagnetic onset is consistent with the result obtained with the transport measurement, however the main difference in measured $T_c$ values can be ascribed to a lack of homogeneity in the whole sample, beyond the usual imbalance coming from the intergranular and intragranular contributions of polycrystalline samples.

After the third HT the sample resistance was measured again and the results are shown in Figure 6. While the superconducting onset appears unchanged with respect

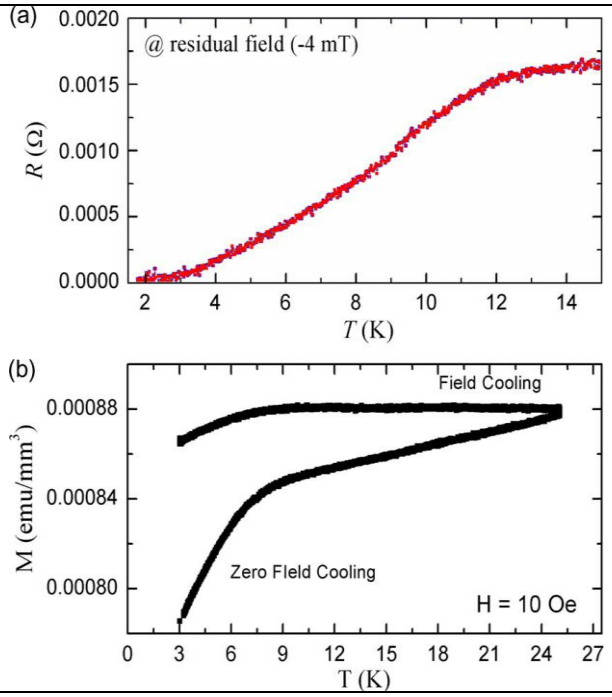


Figure 5. FeSe pellet: superconducting properties after second HT. (a) Four probes resistance measurement versus temperature at 0 T. (b) Magnetization versus temperature measured in ZFC and in FC with $H$ = 10 Oe.

to the one measured before the last HT, the broadness of the transition is slightly reduced, and the $T_{c0}$ can be evaluated to be about 5.5 K. The application of a background magnetic field during resistance measurements enlarges as expected the transition curves. The measured superconducting onset is in agreement with respect to measurements obtained by other groups, but the broadness of the transition is larger, being the $T_{c0}$ found in literature for optimized polycrystalline FeSe in the range 6.6–8 K, [3]–[5],[7],[9],[10]. In particular it was shown [11], that oxygen contamination of the samples can rise to very broad resistive transitions with disappearance of bulk superconductivity and that sintering temperatures between 680 ◦C and 700 ◦C can lead to multiphase samples with non-negligible amounts of iron oxides, formed due to the oxidation of Fe under the high temperature reaction conditions [9]. The non-negligible presence of $\delta$-FeSe phase and iron oxides, along with the possible oxygen contamination, are likely to be responsible for the irregularity and non-homogeneity of the samples which lead to a percolative path of the superconducting current inside the samples and therefore to broad resistive transitions.

### 3.2.3 Further considerations

The production of sintered polycrystalline FeSe samples started from the application of standard HTs on FeSe samples sealed under vacuum, after which a possible optimization of their superconducting properties has been attempted through subsequent HTs.

In polycrystalline samples, the existence of second phases at the grain boundaries strongly influences the correlation between the structural characteristics and the superconducting properties [3]–[11],[14]. As shown in literature [3]–[11], not negligible amounts of $\delta$-FeSe non-superconducting phase and other impurities can be found in samples when the suitable HT cycles are not applied, when starting stoichiometry is even slightly incorrect or if there is oxygen contamination during

samples preparation. It was shown that $\beta$-FeSe phase can easily be surrounded by the $\delta$-FeSe phase during HT cooling stage preventing or reducing the dissolution of $\beta$-FeSe phase to the main matrix [4], [9]-[11]. We can conclude that the possible reasons

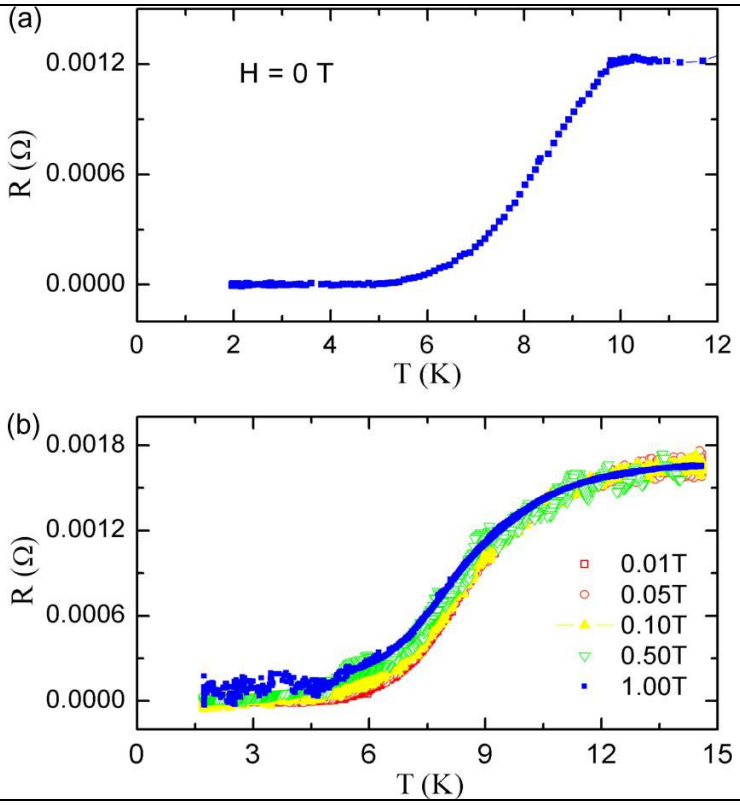


Figure 6. FeSe pellet: superconducting properties after third HT. (a) Four probes resistance measurement versus temperature at 0 T. (b) Four probes resistance measurements with background fields of (empty squares) 0.01 T, (empty circles) 0.05 T, (triangles) 0.10 T, (reversed empty triangles) 0.50 T, and (squares) 1.00 T.

that could explain the poor superconductive properties measured in the presented samples are: possible oxygen contamination, high temperature of the performed treatments, which could have led to non-negligible amount of iron oxides formation, along with the lack of a final annealing at low temperatures, which could have help removing $\delta$-FeSe phase transforming it into $\beta$-FeSe phase, and slightly incorrect stoichiometry in the initial powders.

Nevertheless, relative intensity of the $\beta$-FeSe phase peaks in the XRD measurements increases after the last applied HT, and the SEM micrographs outlines the tendency of the powders to agglomerate in larger compact areas with slight increase of sample connectivity, that can of course be further optimized. This seems in agreement with the increase of $T_{c0}$ measured after the third HT. This small improvement of superconducting properties is encouraging and this result deserves to be pursued besides the end of the work for the Thesis. There are factors identified in this paragraph on which it is possible to act on, and of course it is possible to look for other routes of FeSe polycrystalline samples production. The investigation described in paragraph 3.2 do not portray new scenarios in the fabrication of sintered FeSe, but is however of great actuality, being polycrystalline samples suitable for applications. Every route for polycrystalline production of superconducting FeSe phase, even only slightly different from others, can be interesting in view of possible time or resources

optimization. The results showed in this paragraph have been published and are described in [15].

## References


[1] Demura S. *et al.* (2012) Electrochemical synthesis of Iron-based Superconductor FeSe Films *J. Phys. Soc. Jpn.* 81 043702.

[2] Demura S. *et al.* (2013) Electrodeposition as a new route to synthesize superconducting FeSe *Solid State Communications* 154 pp. 40-42.

[3] Pimentel J. L. Serbena., Jr., F. C, and. Jurelo A. R. (2011) Characterization of $FeSe_x$ superconductor prepared by different thermal routes by instrumented indentation, *J. Supercond. Novel Magn.*, vol. 24, pp. 1437–1441.

[4] Onar K.and Yakinci M. E. (2015) Solid state synthesis and characterization of bulk *β*-FeSe superconductors, *J. Alloys Compounds*, vol. 620, pp. 210–216.

[5] Zhao P. H. *et al.* (2012) A simple fabrication of FeSe superconductors with high upper critical field, *J. Supercond. Novel Magn.*, vol. 25, no. 6, pp. 1781–1785.

[6] Umeyama N.*et al.* (2010) Superconductivity on FeSe synthesized by various sintering temperatures, *Phys. C, Supercond.*, vol. 470, pp. S518–S520.

[7] Mizuguchi Y. *et al.* (2008) Superconductivity at 27 K in tetragonal FeSe under high pressure, *Appl. Phys. Lett.*, vol. 93, Art. no. 152505.

[8] Hsu F. C. (2008) Superconductivity in the PbO-type structure alpha-FeSe, *Proc. Nat. Acad. Sci. USA*, vol. 105, no. 38, pp. 14262–14264.

[9] Janaki J.*et al.* (2009) Synthesis, characterization and low temperature studies of iron chalcogenides superconductors, *J. Alloys Compounds*, vol. 486, no. 2, pp. 37–41.

[10] Li Z. *et al.* (2010) Structural and superconductivity study on $\alpha - FeSe_x$, *J. Phys. Chem. Solids*, vol. 71, pp. 495–498.

[11] T. M. McQueen (2009) Extreme sensitivity of superconductivity to stoichiometry in $Fe_{1+\delta}Se$, *Phys. Rev. B*, vol. 79, Art. no. 014522.

[12] Zola D., Polichetti M., Senatore C., and Pace S. (2004) Magnetic relaxation of type-II superconductors in a mixed state of entrapped and shielded flux, *Phys. Rev. B, Condens. Matter Mater. Phys.*, vol. 70, Art. no. 224504.

[13] Leo A. *et al.* (2015) Vortex pinning properties in Fe-chalcogenides, *Supercond. Sci. Technol.*, vol. 28, no. 12, Art. no. 125001.

[14] Hacisalihoglu M. Y. and Yanmaz E. (2013) Effect of substitution and heat treatment route on polycrystalline $FeSe_{0.5}Te_{0.5}$ superconductors, *J. Supercond. Novel Magn.*, vol. 26, pp. 2369–2374.

[15] Fiamozzi Zignani C. *et al.* (2016) Fabrication and Characterization of sintered Iron-Chalcogenides superconductors, *Trans. on Appl. Supercond.*, vol. 26, n. 3, 7400105.

CHAPTER 4

# FeSeTe polycrystalline samples: structural and superconductive characterization

In this Chapter the main results obtained regarding the structural characterization and the physical properties of manufactured polycrystalline FeSeTe samples are described. In order to have a look at the behaviour of prepared samples and to try to identify the present phases, X-ray diffraction patterns of the material after each HT were recorded at room temperature. The results will be shown starting from first attempts in the samples preparation to the most optimized samples. On the best performing samples, an extended characterization has been performed (Scanning Electron Microscope (SEM) micrographs, X-Ray Diffraction (XRD) and Energy Dispersive X-ray spectroscopy (EDX), magnetic and transport measurements) in order to try to correlate their structural properties to the superconducting behaviour and eventually to describe their vortex pinning properties.

## 4.1 Polycrystalline FeSeTe from solid state reactive sintering

As anticipated in paragraph 2.4, only the results for one representative sample belonging to each group of HTs will be shown in the following.

### 4.1.1 $FeSe_{0.5}Te_{0.5}$ after 1st HT

In this paragraph, $FeSe_{0.5}Te_{0.5}$ properties after first HT are shown. In the following the sample will be referred to as FST550. As described in paragraph 2.4, after the first HT at 550°C powders were manually grinded and reduced into pellets for subsequent HT. At this step the sample has been characterized in order to recognize the phases' formation and for comparison with subsequent heating steps, to evaluate the impact of the heat treatments on the samples properties.

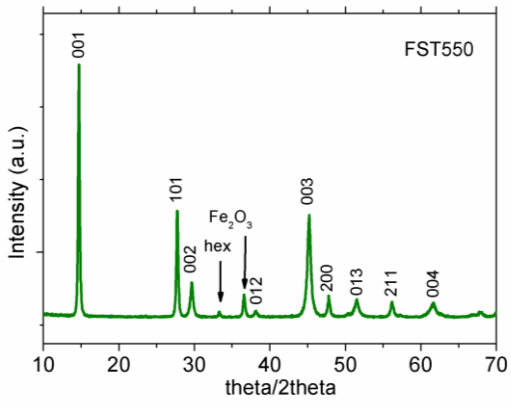


Figure 1: XRD patterns of FST500 sample.

In Figure 1 XRD measurements obtained on pellet after first HT is shown, together with the indication of the phases corresponding to the revealed peaks. The indexes of the FeSeTe reflections correspond to the tetragonal space group P4/nmm and few impurities and spurious phase are still present after the first HT, such as iron oxide and hexagonal phase. SEM micrographs at this stage are presented in Figure 2, and show compact clear zones separated by voids, which is barely an indication of an uneven material.

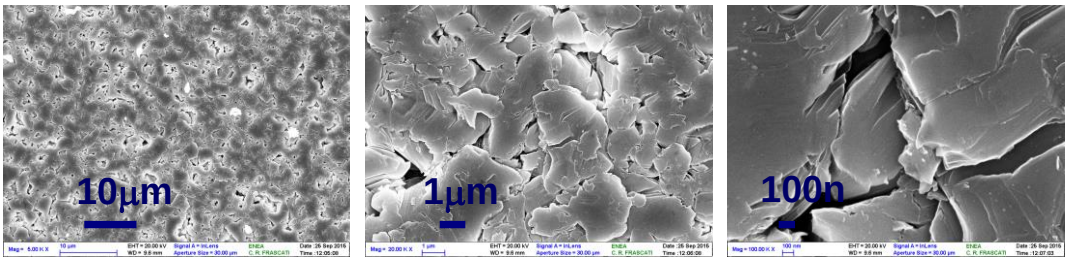


Figure 2: SEM micrographs of sample FST550 surface at different magnifications.

Magnetic measurements on sample FST550 were performed on a piece of dimensions 4.1 x 2.5 x 0.75 mm by means of an Oxford Instrument VSM (Vibrating Sample Magnetometer) equipped with a 12 T magnet and He gas flow system. The magnetic field was perpendicular to the sample surface. Before each measurement, the residual trapped field inside the DC magnet was reduced below $10^{-4}$ Tesla by means of degaussing cycles with a progressively decreasing maximum field amplitude. In Figure 3(a) the magnetic moment versus temperature measured at 10 and 100 Gauss in Zero Field Cooling (ZFC) is shown. The transition temperature, at each field, is determined as the value of the temperature corresponding to the onset of the ZFC moment drop. In particular, the curve at 10 Gauss shows a diamagnetic onset at about 12 K. The magnetic moment of this sample was measured as a function of magnetic field up to 12 T (ramp-rate = 0.5 T/min) at 4.2 K and at 20K, well beyond the transition temperature and the results are shown in Figure 3(b). It is evident that, despite the diamagnetic onset clearly visible in Figure 3(a), the magnetic hysteresis cycle below the transition temperature is very narrow and almost comparable with the

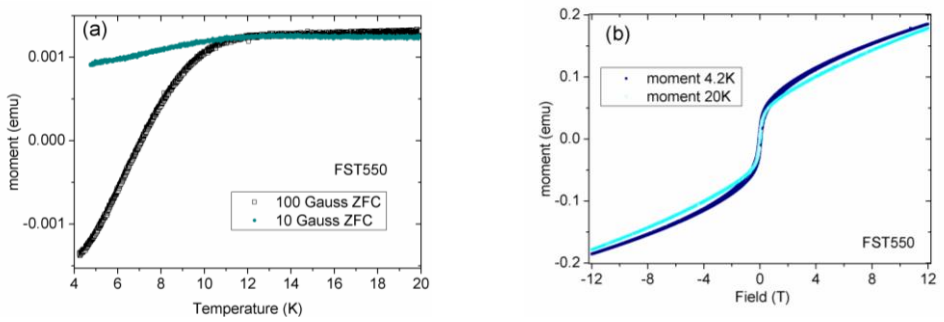


Figure 3: sample FST550: (a) ZFC magnetic moment measurements versus temperature obtained at 10 and 100 Gauss (b) hysteresis cycles at 4.2K and at 20K.

background one, measured at 20 K. Nevertheless, subtracting this background signal from the one measure at 4.2 K, as shown in Figure 4(a), it is possible to verify that the

hysteresis cycle is indeed narrow but open. The cycles measured in the temperature range form 4.2 K to 10 K up to 1 T, after the subtraction of the background are shown in Figure 4(b). Increasing the temperature, the pinning becomes weaker and consequently the width of the loops decreases, even if it is possible to appreciate superconductivity at very low fields up to 10 K.

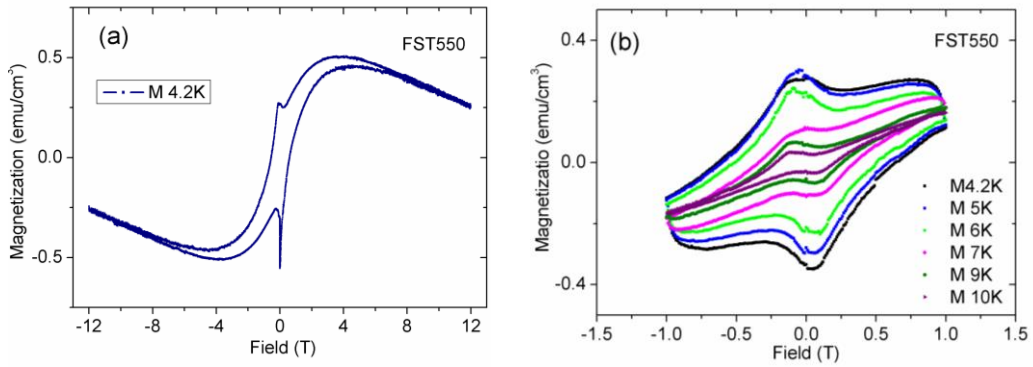


Figure 4: sample FST550: (a) hysteresis cycle at 4.2K after background signal subtraction (b) hysteresis cycles at 4.2, 5, 6, 7, 8, 9, 10 K after background signal subtraction.

Resistance as a function of the temperature $R(T)$ measurement for sample FST550 has been carried out in the range 1.6–300 K. In Figure 5 the $R(T)$ curve at zero magnetic field is shown. The critical temperature ($T_c$), has been estimated with a standard 50% criterion of the normal state resistance ($R_N$). It results a $T_c$ of about 12.7 K, while the transition width $\Delta T_c$, calculated as $T_c(90\%)$-$T_c(10\%)$ is about 6 K, that is very broad. The diamagnetic onset is consistent with the result obtained with the transport measurement, however the main difference in measured $T_c$ values can be ascribed to a lack of homogeneity in the whole sample, beyond the usual imbalance coming from

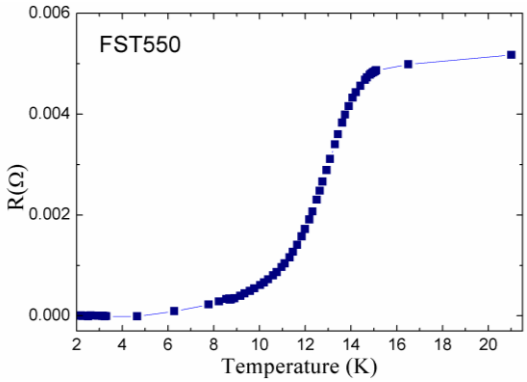


Figure 5: sample FST550, resistance as a function of the temperature at zero field.

the intergranular and intragranular contributions of polycrystalline samples. All this results agree on the fact that sample FST550, despite the undeniable superconducting onset, is an uneven and not optimized sample. Nevertheless is was important to show its behaviour because it is a starting point, and because it can be used as a comparison

with the following FeSeTe samples, which all underwent the same first HT, and which evolved thanks to subsequent HTs.

### 4.1.2 Samples FST650 and FST750

In Figure 6(a) and (b), XRD measurements obtained on FST650 and FST750 pellets are shown, together with the indication of the phases corresponding to the revealed peaks. The indexes of the FeSeTe reflections correspond to the tetragonal space group P4/nmm and few impurities and spurious phases are still present after the second HTs, such as iron oxide and hexagonal phase.

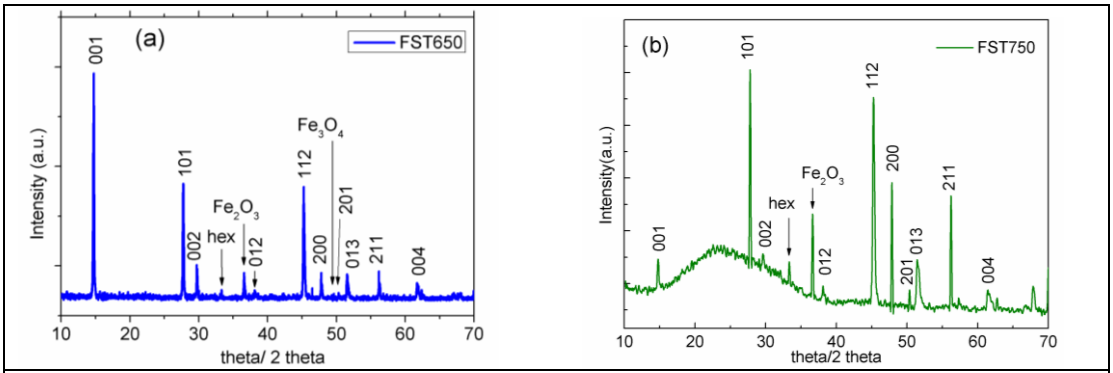


Figure 6: XRD patterns (a) FST650 sample (b) FST750 sample

The two spectra differs in particular for the ratio among FeSeTe peaks. The formation of iron oxides is almost inevitable due to powder handling in air and can cause a depletion of Fe concentration in the samples, leading to the formation of impurity phases such as $FeTe_2$, FeSe and $Fe_7Se_8$, as can be explained in the phase diagrams of FeSe and FeTe for Se content ≥ 0.4 [1], [2]. For the same tetragonal crystal structure, $\beta$-FeTe is more stable than $\beta$-FeSe in terms of sintering temperature and compositional variation. Yeh *et al.* [3] reported that FeTe with same tetragonal crystal structure is stable up to a much higher temperature, ~ 1200 K, compared with FeSe which undergoes a phase transformation toward hexagonal FeSe if synthesized at ~

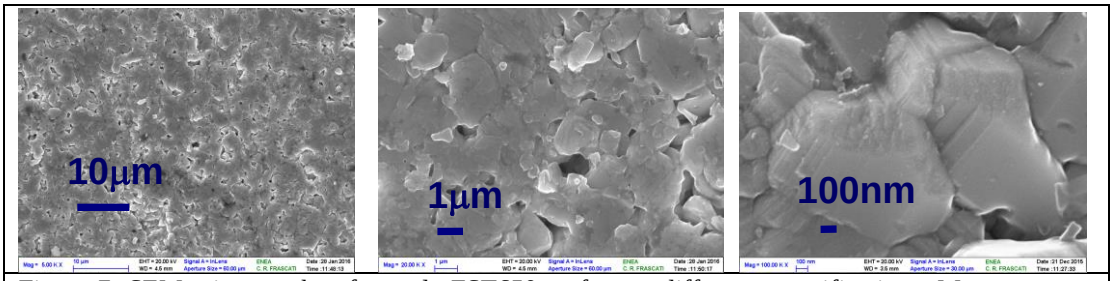


Figure 7: SEM micrographs of sample FST650 surface at different magnifications. Measurements system HR-FEG-SEM Leo 1525. In-lens secondary electron.

731 K. The hexagonal FeSe/$Fe_7Se_8$ tends to form at lower concentration of Te [4],[5]. For both samples the formation of impurity phases is promoted by Fe deficiency [6]. The SEM micrographs shown in Figure 7 do not add much information, but make evident the internal disconnection of sample FST650: as after the first HT, the sample shows compact zones surrounded by disconnection and voids.

Measured FST650 sample has dimensions 4.0 x 3.0 x 0.2 $mm^3$, while measured FST750 sample has dimensions 3.1 x 2.9 x 0.7 $mm^3$. In Figure 8 moment versus temperature measured for both samples in Zero Field Cooling (ZFC) are shown.

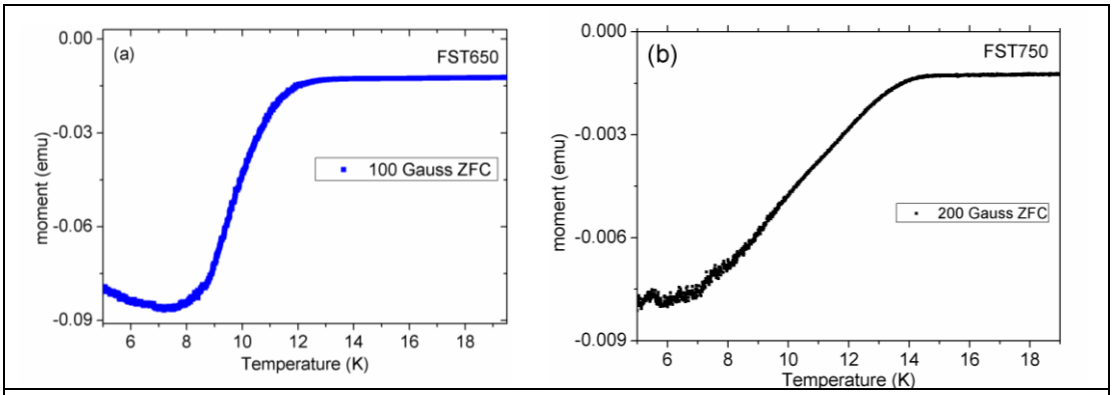


Figure 8: ZFC measurements of moment versus temperature obtained for (a) sample FST650 at 100 Gauss and (b) for sample FST750 at 200 Gauss.

The transition temperatures, determined as the value of the temperature corresponding to the onset of the ZFC moment drop, are about 11.8 K for sample FST650 and 13.8 K for sample FST750. A diamagnetic response, due to the sample holder at $T>T_c$, is clearly visible in both measurements.

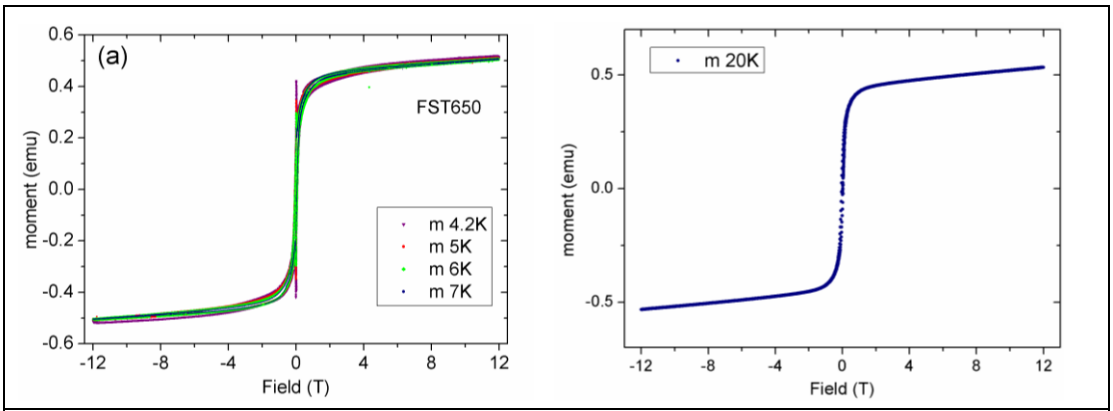


Figure 9: sample FST650: (a) magnetic moment versus external field curves obtained at different temperatures (b) hysteresis background cycle measured at T=20 K

The magnetic moment of these samples was measured as a function of magnetic field up to 12 T (ramp-rate = 0.5 T/min) in the temperature range between 4.2 K and 7 K, for sample FST650 and up to 5 K for sample FST750. The results are shown in Figure 9(a) and Figure 11(a) respectively. The loops are very narrow and it is possible to see a very small irreversibility in the cycles after the subtraction of the background hysteresis cycle measured for both samples at 4.2 K (Figure 10 and Figure 11(b)). The very tight loops, even if open up to 12 T, are an indication of the poor superconductivity inside the samples.

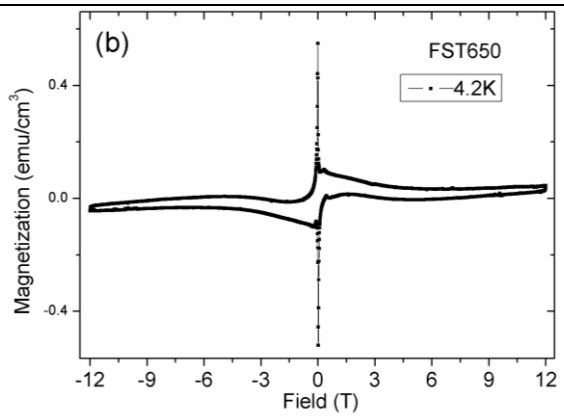


Figure 10: FST650 : hysteresis loop at 4.2 K after the subtraction of the background cycle measured at 20 K.

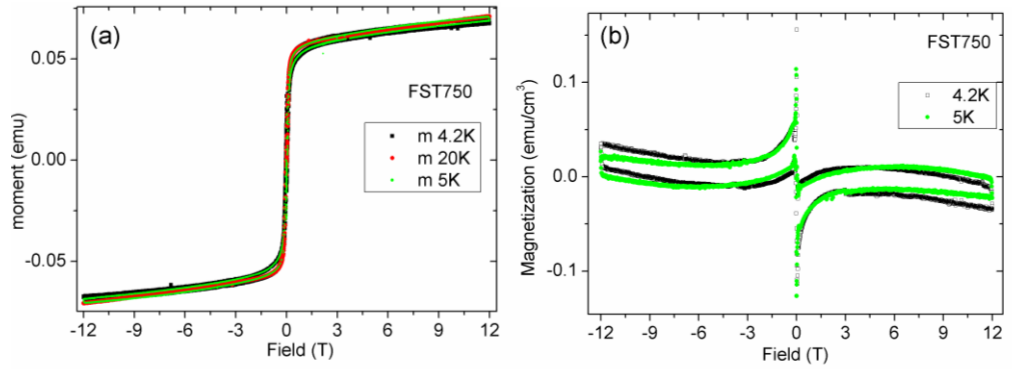


Figure 11: sample FST750: (a) magnetic moment versus external field curves obtained at different temperatures (b) hysteresis loops at 4.2 K and 5 K after the subtraction of the background cycle measured at 20 K.

## 4.2 Polycrystalline FeSeTe from mechano-chemical synthesis

In this paragraph the results obtained for the samples prepared by means of mechano-chemical synthesis are described.

In Figure 12(a) X-ray diffraction patterns on sample HEBM10 are shown, including the intermediate results after short ball milling steps. HEBM promotes first of all Se-Te blending, as shown in the patterns recorded after 10 minutes and after 1 hour. After 2 hours (Se-Te) is reacting with iron and Fe(Se,Te) phases are forming, but iron has not completely been absorbed in the mixture and the stoichiometry for the correct phase formation is not complete. After 10 hours $\beta$-Fe(Se,Te) is crystallizing (Wt% 81), together with $Fe_7(Se,Te)_8$-like phase (Wt% 19). SEM micrograph in Figure 12(b) shows an almost amorphous composite with grains of tens nm.

Thermo-analytical characterizations such as Temperature-Programmed Desorption (TPD) techniques are important methods for the determination of kinetic and thermodynamic parameters of desorption processes or decomposition reactions. In our case, powders belonging to sample HEBM10 were set under gas flow ($Ar/H_2$ 3% and $He/H_2$ 3%) conditions and the out-coming flows have been checked, measuring the

heat capacity of the gas in each of the two cases. In both cases the sample exhibits high reactivity towards hydrogen. There is a great amount of $H_2$ consumed, which suggests high reactivity of powder with oxygen, confirmed by water formation. The TPD results are shown in Figure 13. Despite the tetragonal $\beta$-Fe(Se,Te) formation during ball milling, sample HEBM10 does not show superconductivity. This is probably due to the presence of many defects and spurious phases beside the tetragonal one.

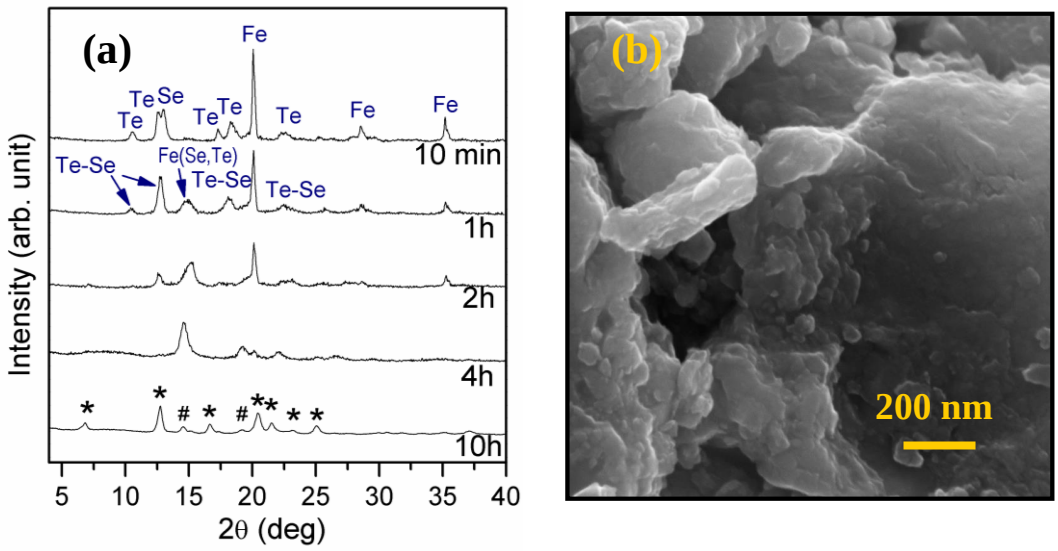


Figure 12: sample HEBM10: (a) XRD measurements at several steps of the HEBM process. In the last line * refer tetragonal $\beta$-Fe(Se,Te), and # to $Fe_7(Se,Te)_8$.(b) SEM micrograph .

The same powders used for sample HEBM10 were then heat treated for 24 hours at 700 to obtain sample HEBM10-700, as described in paragraph 2.5. XRD pattern for this sample is shown in Figure 14(a). The tetragonal $\beta$-Fe(Se,Te) phase is present (Wt% 84) together with a Te rich secondary phase (Wt% 16). A polycrystalline multi-phase material is obtained, with significant particle growth with respect to the powder, as shown in the SEM micrograph presented in Figure 14(b).

.

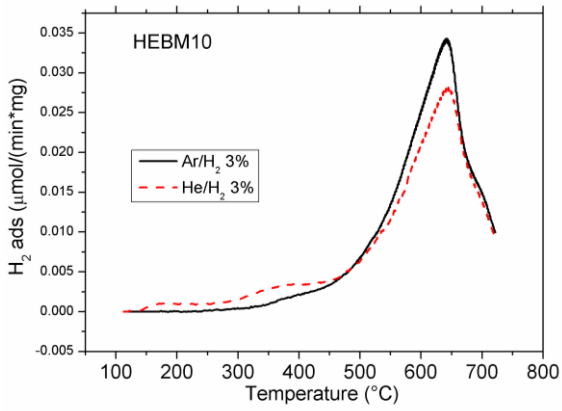


Figure 13: TPD measurements on HEMB10 powders with $Ar/H_2$ and with $He/H_2$ gas flows.

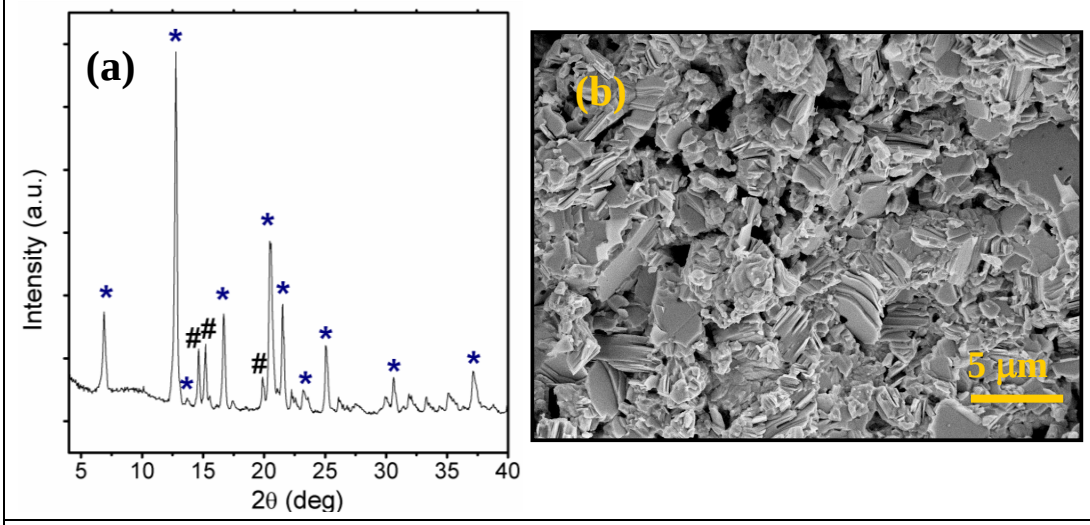


Figure 14: sample HEBM10-700: (a) XRD measurements 24 hours sintering at 700 °C. Symbol * refer tetragonal $\beta$-Fe(Se,Te), and # to $Fe_7(Se,Te)_8$.(b) SEM micrograph.

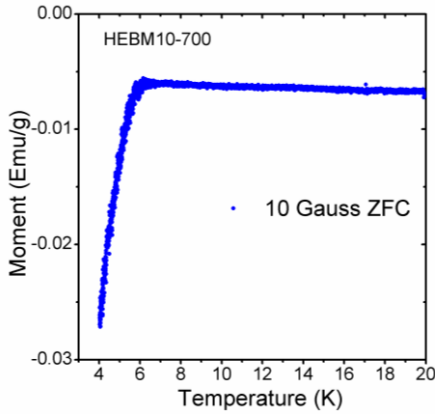


Figure 15: magnetic moment versus temperature at 10 Gauss (ZFC) for sample HEBM10-700.

The weight of sample HEBM10-700 is 86.6 mg and its diamagnetic transition, with the onset at about 6 K, is shown in Figure 15. A diamagnetic response, due to the sample holder at $T>T_c$, is clearly visible in this measurement. The superconducting onset is quite low respect to literature, and this can be due to the reactivity of the precursors powder (that is sample HEBM10) with oxygen, as shown in Figure 13. So it results that till now the samples produced with this techniques are not optimized, and further developments are required to keep the phase clean and avoid defects that compromise the superconducting performances.

## 4.3 Polycrystalline FeSeTe from fusion

In this paragraph the results for samples FST800, FST970B and FST970 are presented. These are the best performing among the samples that have been prepared during this work of Thesis, and have been extensively characterized. The first two

samples will be directly compared, while the third one will be treated apart, because of its peculiar characteristics.

The results for sample FST800 have been inserted in this paragraph even if it is not properly a sample obtained from melting (as said 800 °C is about the fusion temperature of the composite). This choice is due to the fact that, as already evidenced, it belongs to the group of the best performing samples and inserting its results in this paragraph conveys an easy comparison among these samples.

## 4.3.1 Samples FST800 and FST970B

The two samples presented here have been firstly characterized by means of Scanning Electron Microscope (SEM) micrographs, X-Ray Diffraction (XRD) and Energy Dispersive X-ray spectroscopy (EDX), in order to recognize the phases' formation and to measure the composition. The impact of the heat treatments, described in Chapter 2, on the samples properties has been analysed through an extensive campaign of magnetization and transport measurements. The pinning properties of these two types of samples have been compared to correlate the fabrication process with the pinning landscape. The final aim would be to obtain an increased $T_c$ and $H_{c2}$, as well as an enhanced pinning efficacy which could lead to higher critical current density, $J_c$, relevant for practical uses. Most of the analysis and the results presented in this paragraph have been included in [7].

### 4.3.1.1 Structural characterization and compositional analysis

In general, FST970B samples are larger than FST800 ones: X-ray diffraction patterns of the two samples are shown in Figure 16(a) and 16(b) respectively. The indexes of the FeSeTe reflections correspond to the tetragonal space group P4/nmm. Both the samples grew with a preferential orientation along the *c*-axis, as can be deduced from the fact that the (00ℓ) peaks are more intense than the off axis peaks, in contrast to what happens with random powder or polycrystalline samples [4]-[6],[8],[9]. Only some residuals of the polycrystalline phase are detectable in the patterns and, in the case of FST800, it is also observed that the (00ℓ) peaks are asymmetric. This detail and the lower intensity of the peaks indicate that grains are smaller and misoriented with respect to that of the FST970B. The images in the insets of Figure 16 are coherent with the XRD results: the first micrograph shows a flat area of the FST970B crystal and the terraces typical of the layered structures; the second one also represents a flat area with some terraces, but smaller than the previous ones and with many defects and impurities. The two samples' dimensions are comparable. The areas being equal, it results that in sample FST800 more grains are present (size around 70 μm x 60 μm) with several iron oxide particles among them; sample FST970B has larger grains (size around 250 μm x 150 μm) without spurious phases and with some residuals of the fused phase.

The chemical compositions of the two samples have been determined by EDX analysis selecting a grid of 50 points on areas of about 1.5 mm x 1 mm and performing a statistical calculation of each element content, normalizing to the sum Se+Te [10]. Figure 17 show examples of statistical analysis obtained for each element for the two samples under investigation: the statistical distribution of the data are centred on the element content normalized to the sum of Se and Te. Figure 17(c) shows a sketch of the typical grid of points acquired on one of the samples.

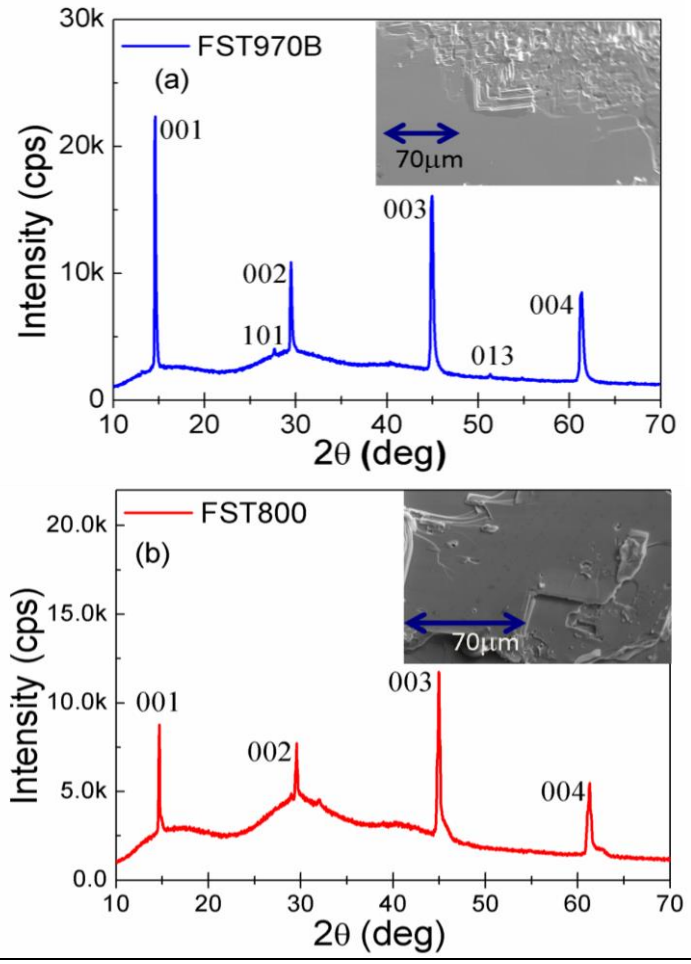


Figure 16: XRD measurements of samples FST970B (a) and FST800 (b). In the insets: SEM images of the samples surface.

The final compositions are given as an average and it results that both samples are homogeneous with a very small Fe excess. It results: $Fe_{1.05}Se_{0.44}Te_{0.56}$ for sample FST970B and $Fe_{1.03}Se_{0.41}Te_{0.59}$ for sample FST800 and the slight excess of iron is coherent with the $T_c$ values that will be reported in the following [11],[12]. The Se:Te ratio results less than 1, indicating a slight difference from the nominal composition of the samples which indeed does not critically affect the $T_c$ value [9]. The presence of defects and impurities among the grains of FST800 sample are observed by SEM and mainly associated to iron oxides, maybe related to oxygen leakage from defects occurring on the quartz tube during the heat treatment process.
In literature ([13],[14]) it has been evidenced that the composition of sintered $Fe(Se_{1-x}Te_x)$ phase is non-homogeneous, and this phenomenon has been related to a thermodynamic instability of the $Fe(Se_{0.5}Te_{0.5})$ composition at 800 °C. I intended to verify if, after the heat treatment at 800 °C, the homogenization of the superconducting phase inside the sample could have been improved with the extra step at 400 °C done without intermediate regrinding of the powders. The results obtained indicate that this is not the case, maybe also because of the short duration of this extra step at 400 °C (usually in literature final annealing processes are much longer [13]). It seems that the extra step has negligible influence, so the influence of sintering temperature alone for these two samples can be easily compared. Actually,

the choice of the comparison of samples obtained with this two temperatures, one slightly below and the other above the fusion temperature of the composite, has been done in order to evidence the possibility of removing spurious phases between grains during the fusion process, and this is confirmed by the different morphology of the two samples in the SEM images.

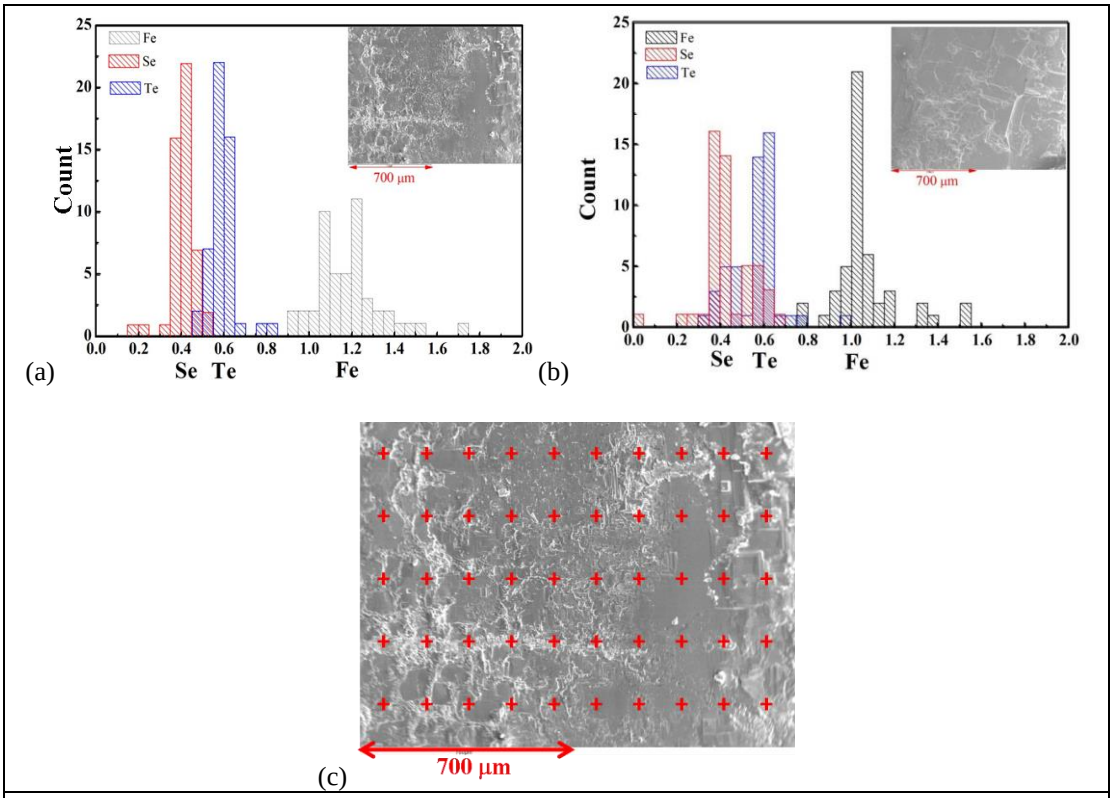


Figure 17: Statistical analysis of (a) FST970B and (b) FST800 samples. The insets are SEM images of the samples. (c) SEM image of sample FST970B with a sketch of the grid of points acquired on it.

### 4.3.1.2 Magnetic and transport measurements

Measured FST970B sample has dimensions 4.1 x 2.0 x 0.2 $mm^3$, while measured FST800 sample has dimensions 3.1 x 2.5 x 0.75 $mm^3$ and measurements where carried out with magnetic field perpendicular to the sample surface and parallel to the *c*-axis. In Figure 18(a) dc susceptibility versus temperature measured for sample FST800 at several magnetic fields in Zero Field Cooling (ZFC) is shown. In Figure18(b) the comparison between measurements at 0.001 T for both samples is presented, where demagnetization factors have not been taken into account. The transition temperature, at each field, is determined as the value of the temperature corresponding to the onset of the ZFC moment drop. In particular, the curves at 0.001 T show a diamagnetic onset at about 15.2 K for sample FST970B and 15 K for sample FST800. Besides the diamagnetic response, due to the sample holder at $T>T_c$ observed at 0.001 T for both samples, sample FST800 gives at the same time a ferromagnetic response that increases with the applied field, as shown in Figure 18(c); this is compatible with the data presented in Figure 19(b) and could be due to the presence of ferromagnetic oxides, in agreement with the microanalysis results.

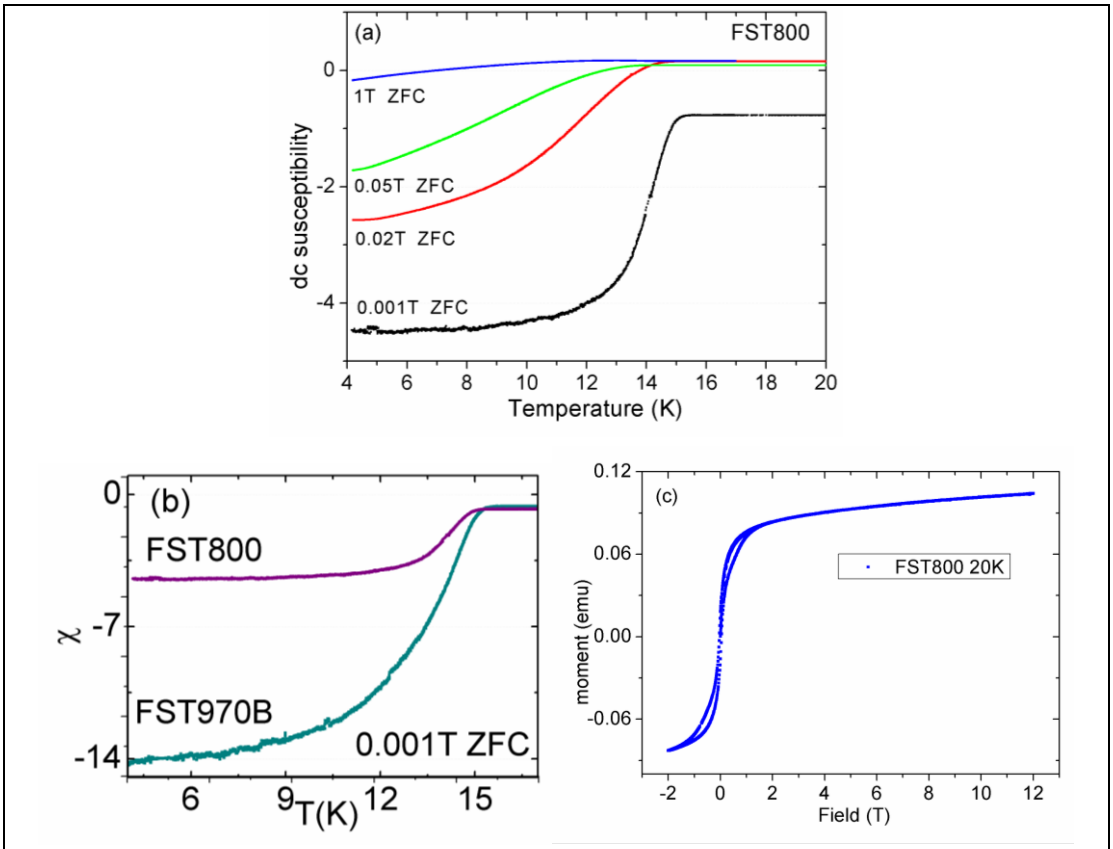


Figure 18: (a) ZFC measurements of adimensional dc susceptibility versus temperature obtained for different fields in sample FST 800. (b) Comparison of the results obtained at 0.001T for samples FST970B and FST800. (c) Hysteresis cycle measured at 20K for sample FST800. The measurements have not been corrected for the demagnetization factor.

The magnetic moment of these samples was measured as a function of magnetic field up to 12 T (ramp-rate = 0.5 T/min) in the temperature range between 4.2 K and 14 K, the results are shown in Figure 19. Increasing the temperature, the pinning becomes weaker and consequently the width of the hysteresis loops decreases. Sample FST970B shows a ferromagnetic background as well (Figure 19(c)), and, as the intensity of its signal is lower, it doesn't almost affect the shapes of the magnetization cycles below $T_c$.

The magnetic field dependence of the current density $J_c$ can be extracted from the $m(\mu_0 H)$ curves, for different values of the temperature, using the Bean critical state formulas [15], after the subtraction of the background signal measured at $T>T_c$. For a slab in perpendicular magnetic field, $J_c(T,\mu_0 H)=3\Delta m(T,\mu_0 H)/a^2 c(3b-a)$, where $\Delta m(T,\mu_0 H)$ is the separation between the two branches of the magnetic-moment loop, $b$ and $a$ are the length and the width respectively, of the samples ($b>a$), and $c$ is the thickness [16],[17]. Anyway, as the samples under investigation are polycrystalline, it would be difficult to distinguish the contributions of the inter-granular and intra-granular critical current density. For this reason, I preferred to talk about $\Delta m$, considering that, as far as the Bean model is assumed, it is proportional to the intergranular critical current density $J_c$.

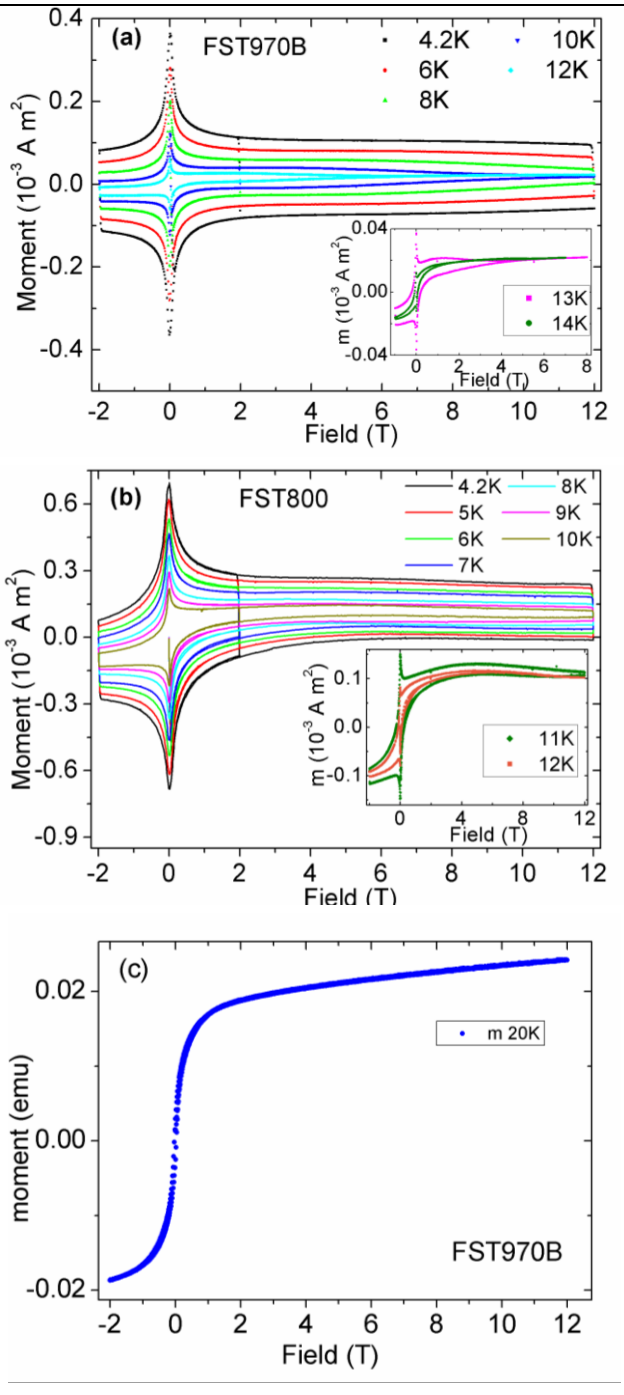


Figure 19: Magnetic moment versus external field curves obtained at different temperatures in sample FST970B (a) and FST800 (b). In the insets the measurements at temperatures near the transition are shown. (c) Hysteresis cycle measured at 20K for sample FST970B.

As shown in Figure 20, the $\Delta m$ values are always higher for the FST970B sample at any temperature. Moreover the magnetic field dependence of $\Delta m$ is quite robust, showing an almost constant behaviour in a wide intermediate field range above 1 T. It cannot be disregarded that sample FST800 presents a more insensitive and flat behaviour at high fields.

In Figure 21 the $R(T)$ curves at magnetic fields from zero to 9 T in steps of 0.3 T for both samples are presented.

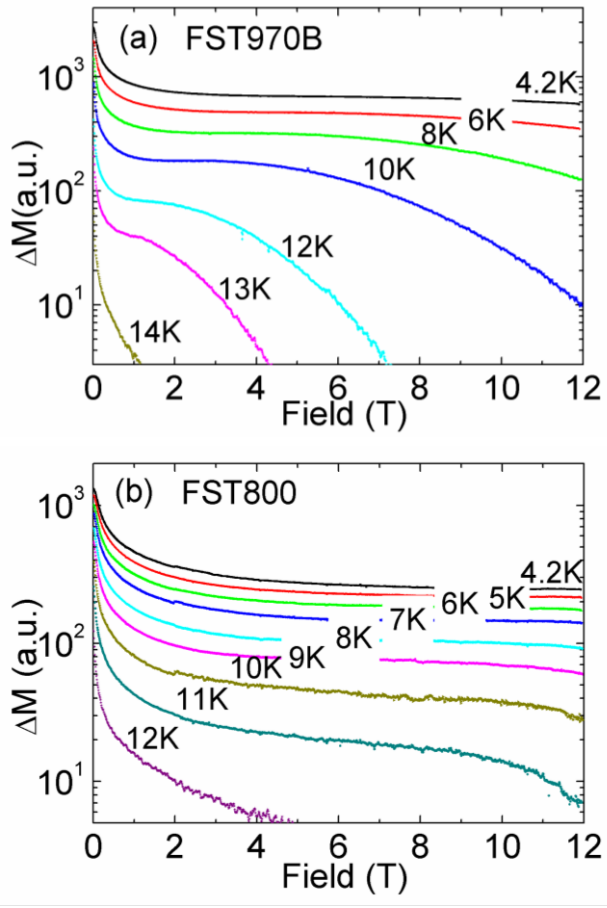


Figure 20: Field dependence of the critical current density at different temperatures in sample FST970B (a) and FST800 (b).

The critical temperature ($T_c$), has been estimated with a standard 50% criterion of the normal state resistance ($R_N$). It results a $T_c$ of about 14 K for FST970B and of about 15 K for FST800 in good agreement with what reported in literature, [9],[13],[18].

Magneto-resistance measurements provide also the magnetic field-temperature phase diagrams. In Figure 22 the irreversibility line and the upper critical field, together with the critical temperature lines are shown for the two investigated samples. The $\mu_0 H_{c2}$ has been defined by the standard 90% criterion of $R_N$, while $\mu_0 H_{irr}$ has been determined by the 10% criterion of the normal state resistance. For sample FST970B the superconducting transition width $\Delta T_c$ at 0 T is about 0.8 K and at 8 T is about 1.3 K. For sample FST800 $\Delta T_c$ at 0 T is about 1.8 K and at 8 T is about 2.5 K. These results can be interpreted as a sign of good homogeneity and a better quality of sample FST970B.

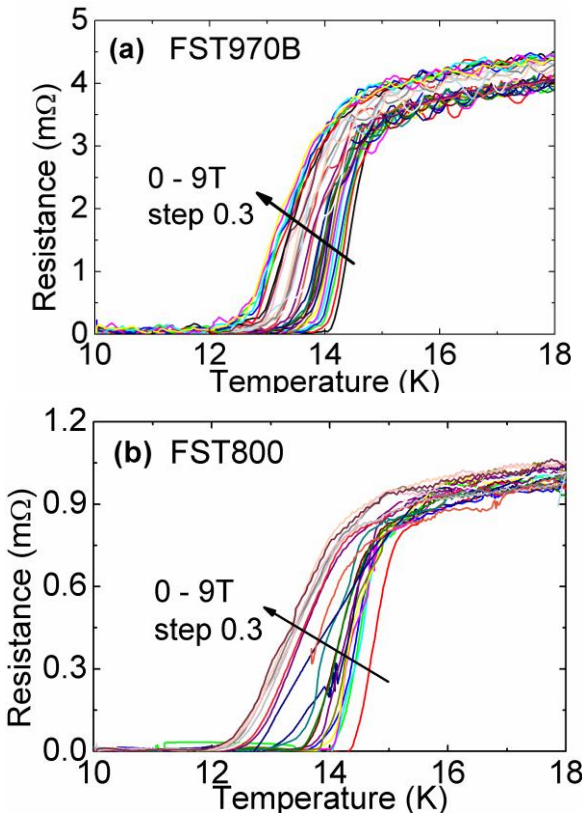


Figure 21: Resistance as a function of the temperature curves from zero to 9T applied magnetic field for samples FST970B (a) and FST800 (b).

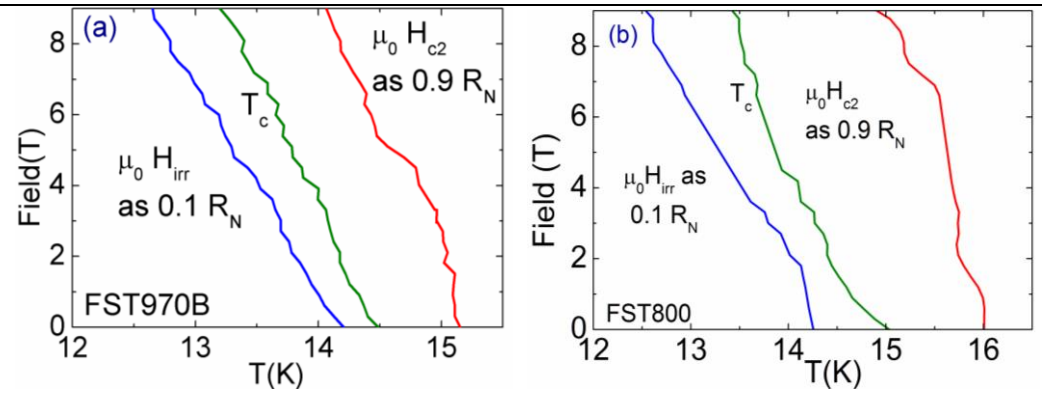


Figure 22: Upper critical field and irreversibility field as a function of the temperature for samples FST 970B (a) and FST 800 (b).

### 4.3.1.3 Pinning properties

It is crucial to understand the pinning mechanism in iron-chalcogenides both from the practical and the fundamental point of view. In order to shed light on the mechanisms that rule pinning in these FeSeTe samples, we have investigated the magnetic field dependence of the normalized pinning force density ($f_p=F_p/F_{p,max}$). It has been shown for a variety of low-$T_c$ and high-$T_c$ superconductors that the curves of $f_p$ obtained at different temperatures, plotted versus the reduced magnetic field ($h=H/H_{irr}$), scale into a unique curve. The empirical formula that accounts for the scaling is $f_p(h)=ch^p(1-h)^q$

where $c$ is a proportionality constant, $p$ and $q$ are two parameters whose values depend on the origin of the pinning mechanism [19].

In general, flux lines interact with pinning centres because the superconducting properties of the latter are different from those of the bulk of the superconductor. The energy gain of the vortex lattice achieved from an adjustment of the flux-line configuration to the spatial distribution of the pinning centres can result from various interactions. The pinning mechanisms for nearly isolated flux lines is expected to be different from that of a lattice of strongly interacting vortex lines [20]. For nearly isolated vortex lines, flux pinning can result from the interaction between the normal vortex core and a local inhomogeneity in the material. At the centre of a vortex line the order parameter drop to zero and the condensation energy needed for generating this normal core can be totally or partially recovered if the core of the vortex line passes through a region in the material where the order parameter is already zero or suppressed below its regular value through the presence of normal inclusions, voids, etc. When either the size or the spacing of the pinning centres are less than $\lambda$ (the distance over which the magnetic induction can undergo an appreciable change within the superconductor) the magnetic induction cannot adjust to the local equilibrium value and will assume some appropriate average value. The free energy of the flux lines has a value in the pinning centres different from that in the matrix and this kind of interaction is referred to as core interaction [19],[20].

In addition to the energy of the normal vortex core, nearly isolated flux lines contain an energy contribution from the magnetic field and the circulating supercurrents associated with the lines. If both the size and the spacing of the pinning centres are greater than $\lambda$, the field is able to adjust everywhere to its equilibrium value [19]. Sample inhomogeneity will change the distribution of magnetic fields and supercurrents, resulting in spatial variations of the line energy and in magnetic pinning interaction [20].

In the superconducting state the density and the elastic constant of a material are slightly smaller than in the normal state, hence in the normal core of a vortex line the material is slightly denser and stiffer than in the superconducting region around it, and this leads to elastic pinning interactions. For high vortex line densities the distinction between core interaction and magnetic interaction is not very meaningful, and the Ginzburg-Landau theory will be more adequate for describing the pinning interactions [20].

Within the Dew-Hughes model, the different contributions to flux pinning are usually catalogued into two main categories: (i) $\delta l$ (or normal) pinning, arising from spatial variations in the charge carrier mean free path near lattice defects and (ii) $\delta T_c$ (or $\delta k$) pinning, associated with spatial variations of the Ginzburg parameter $k$ due to fluctuations in the transition temperature $T_c$ [19],[21]. A classification is also made for pinning centers, as a function of the number of dimensions that are large with respect to the inter-vortex distance $d \sim (\phi_0/B)$. Following the definition given by Dew-Hughes in [19], in this work I refer to point pins as regions whose dimensions in all direction are less than $d$, line pins, which have one dimension larger than $d$, grain- and twin-boundaries, which have two dimensions greater than $d$ and act as surface pins, and volume pins, which have all dimensions large with respect to $d$. In the framework of Dew-Hughes model, different values for $p$ and $q$ are expected, as a function of the

specific pinning mechanism involved. Correspondingly, the theoretical $f_p$ versus $h$ curves present a maximum at different $h$ values. In the case of $\delta l$ pinning, the maximum is expected at $h$=0.33 ($p$=1, $q$=2) for point pins and at $h$=0.2 ($p$=1/2, $q$=2) for surface pins, such as grain boundaries. No maximum is expected in the case of $\delta l$ volume pinning ($p$=0, $q$=2). The maximum of the $f_p(h)$ curve is expected at higher values in the case of $\delta T_c$ pinning; in particular it occurs at $h$=0.67 ($p$=2, $q$=1) for point pins, at $h$=0.6 ($p$=3/2, $q$=1) for surface pins and at $h$=0.5 ($p$=1, $q$=1) for volume pins. Therefore, important information on the physical origin of the pinning mechanisms can be achieved by analyzing the scaling, if present, of the $f_p(h)$ curves.

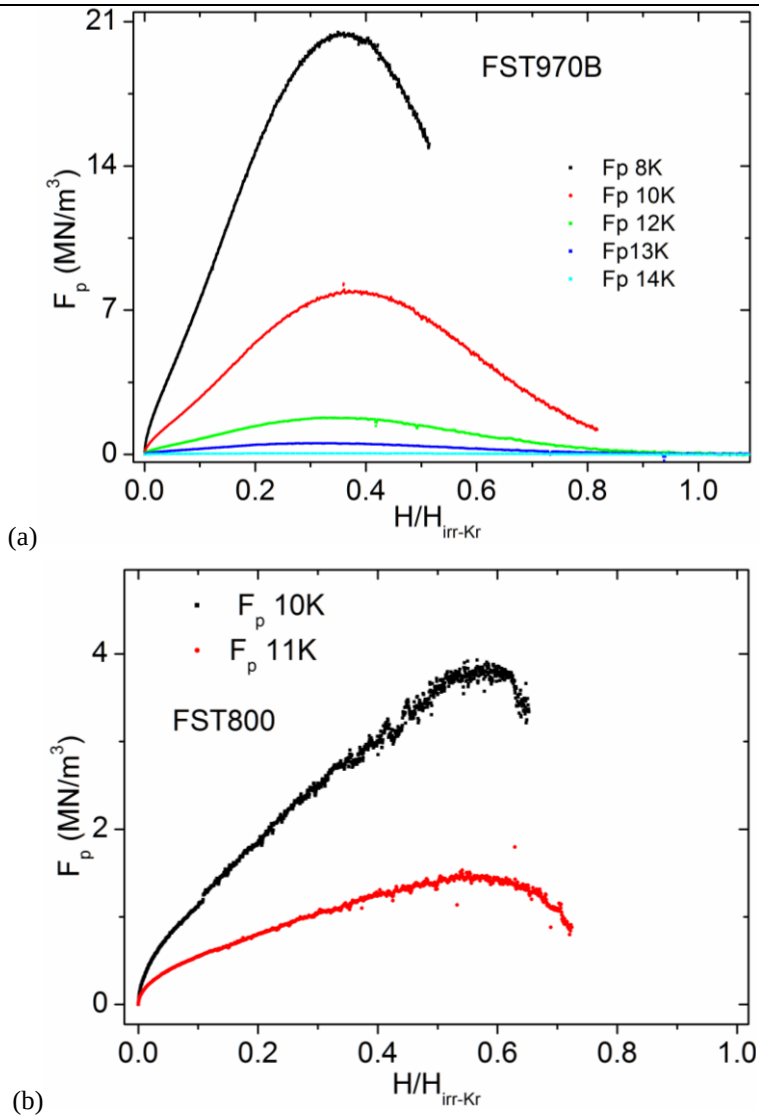


Figure 23: Pinning forces as a function of normalized magnetic field at several temperatures: (a) sample FST970B and (b) sample FST800.

The pinning forces ($F_p$) as a function of the normalized magnetic field at different temperatures have been evaluated from magnetic measurements for both samples and are reported in Figure 23. Here the $H_{irr}$ values have been evaluated as the extrapolated zero value in the Kramer plots, where $J_c^{1/2}\mu_0 H^{1/4}$ is plotted as a function of $\mu_0 H$

[16],[22]. Despite the aforementioned possible inadequacy of the use of the Bean model in these polycrystalline samples, here the $F_p$ of the two samples under investigation are quantitatively compared, and the stronger pinning present in sample FST970B with respect to the sample FST800 is evidenced without ambiguity.

The normalized pinning forces as a function of the normalized magnetic field at different temperatures have been also evaluated for both samples and are reported in Figure 24. In Figure 24(a) the $f_p(h)$ curves are shown at four different temperatures (8 K, 10 K, 12 K and 13 K) for the sample FST970B and in Figure 24(b) at two temperatures (10 K and 11 K) for sample FST800. At lower temperatures the $\mu_0 H_{irr}$ could not be extrapolated because of the very weak $J_c$ dependence on the applied magnetic field up to 12 T.

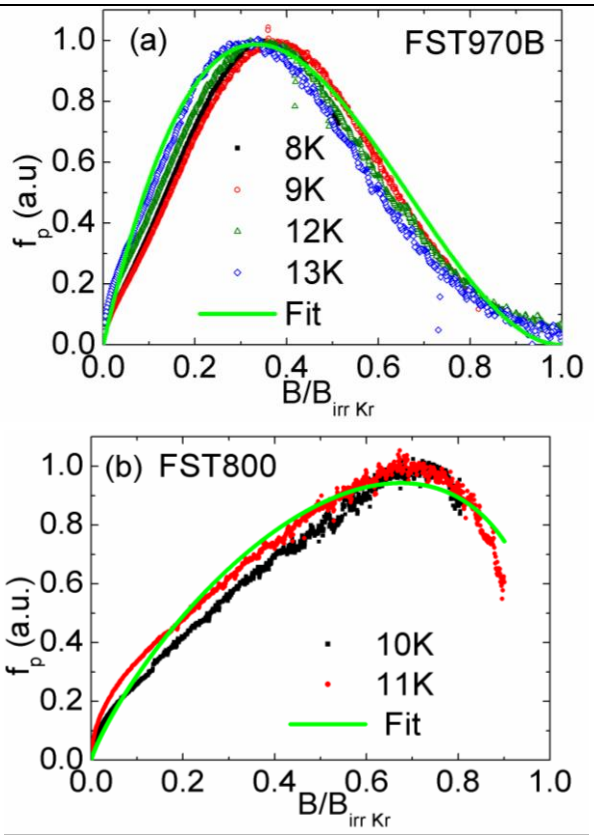


Figure 24: Normalized pinning force as a function of normalized magnetic field at several temperatures together with fits by the Dew-Hughes model as described in the text: (a) for the sample FST970B and (b) for the sample FST800.

Generally speaking, for conventional superconductors, the expected behaviour of the pinning force is $f_p(h)=ch^{0.5}(1-h)^2$ [19],[22]. Dense, strong pinning produces a high peak in $f_p$(h) at low $h$, whereas weaker and fewer pinning centres produces a low peak in $f_p(h)$ at high $h$. Therefore such a pinning function is sensitive to pinning strength and spacing [19],[22]. Experimental data for the two different kind of samples show a major difference: the pinning function $f_p(h)$ is peaked around $h$=0.7 for the FST800 sample, whereas around $h$=0.35 for the FST970B sample. This is an evidence of the different pinning mechanisms acting in the two samples, as well as of the different types of pinning centers that can be present. We fitted the experimental $f_p$ curves with

the scaling law $f_p$=C $h^p(1-h)^q$ [19], obtaining $p$=1 and $q$=2 for sample FST970B, while $p$=0.83 and $q$=0.4 were the best fitting parameters for sample FST800. Thus, considering the above discussion regarding the position of the maximum and the values of $p$ and $q$ parameters in the framework of the Dew-Hughes model, for both samples we can talk of core pinning with point defects. Pinning in sample FST970B can be due to the spatial variations in the carrier mean free path $l$ ($\delta l$ pinning), in agreement with other reports found in literature for this material [16],[23],[24]. Pinning in sample FST800 could be at least partially due to spatial variations of the Ginzburg parameter $k$ due to $T_c$ fluctuations ($\delta T_c$ or $\delta k$ pinning). Here, it is worth mentioning that $h_{max}$ is highly sensitive to a proper determination of $H_{irr}$.

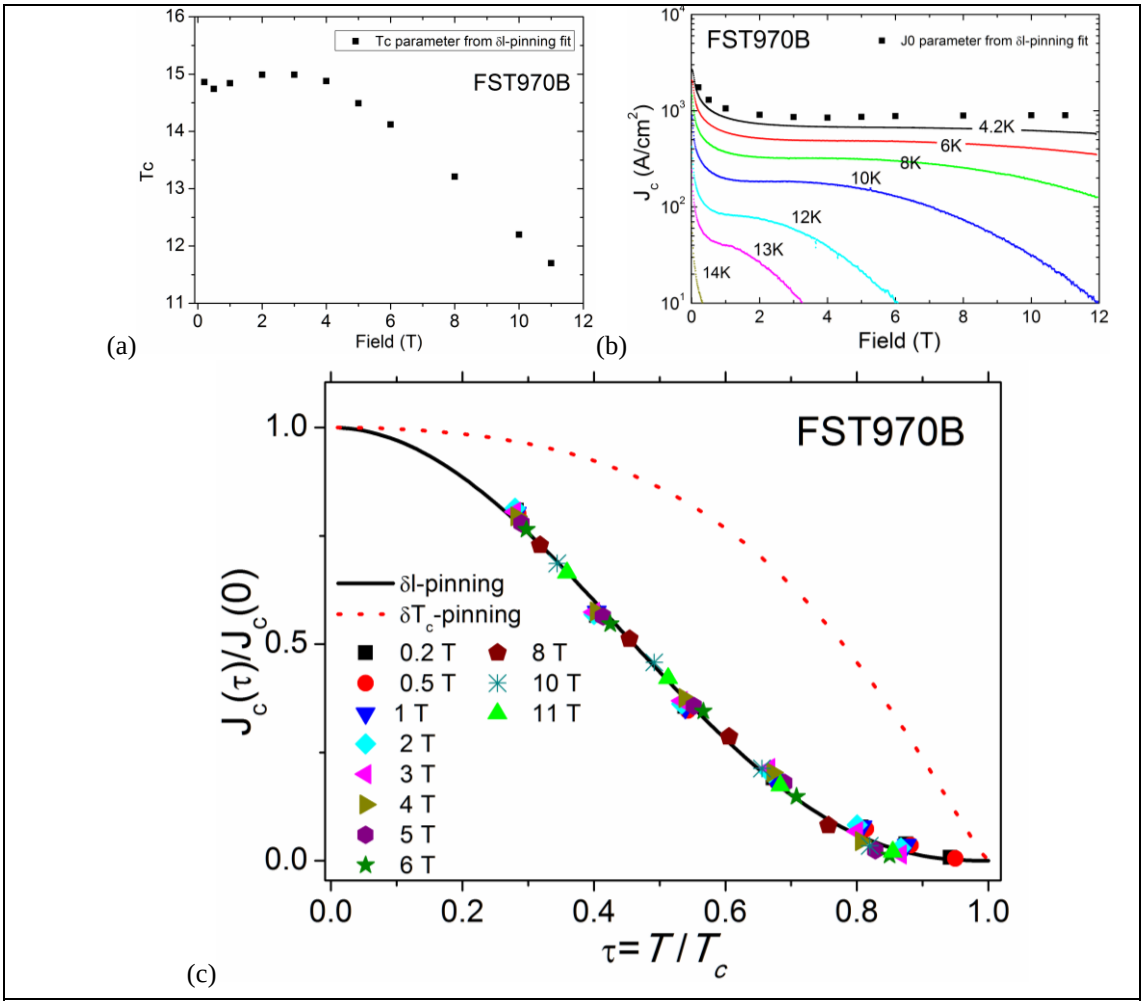


Figure 25: sample FST970B (a) $T_c(0)$ fit parameter obtained fitting the data with $\delta l$-pinning model (b) $J_0$ fit parameter obtained fitting the data with $\delta l$-pinning model together with $J_c$ measured values from 4.2 K to 14 K (c) normalized $J_c(\tau)$ data obtained from magnetization curves at several fields as a function of the reduced temperature τ. The continuous and dotted lines are the theoretical curves expected within the scenarios of $\delta l$ and $\delta T_c$ pinning models respectively.

In order to understand the nature of pinning in more detail, I followed the theoretical approach proposed by Griessen *et al.* [16],[25] and applied it to both samples FST970B and FST800. Within the Griessen framework, in the case $\delta l$-type weak pinning in the single-vortex regime it is expected that the critical current density

variation with respect to the reduced temperature ($\tau=T/T_0$, $T_0=T_c(0)$) is described by the following expression: $J_c(\tau)/J_c(0)=(1-\tau^2)^{5/2}(1+\tau^2)^{-1/2}$. For $\delta T_c$ pinning it is: $J_c(\tau)/J_c(0)=(1-\tau^2)^{7/6}(1+\tau^2)^{5/6}$. In Figure 25(c) the normalized $J_c(\tau)$ data obtained from magnetization curves at several fields for samples FST970B are plotted, along with the theoretical curves expected within the scenarios of $\delta l$ and $\delta T_c$ pinning. Data are normalized using the $J_c(0)=J_0$ values obtained from the fit to the expression for $\delta l$-pinning that are shown in black squares in Figure 25(b). The corresponding $T_c(0)$ values obtained fitting with the same model are presented in Figure 25(a). The amazing accordance of data measured for sample FST970B to $\delta l$-pinning model, together with the convincing values obtained for the fit parameters at all considered fields, are in agreement with the analysis of the $f_p$ curves within the Dew-Hughes model. It is possible to conclude that pinning in sample FST970B is strongly correlated with spatial variations in charge carrier mean free path *l*.

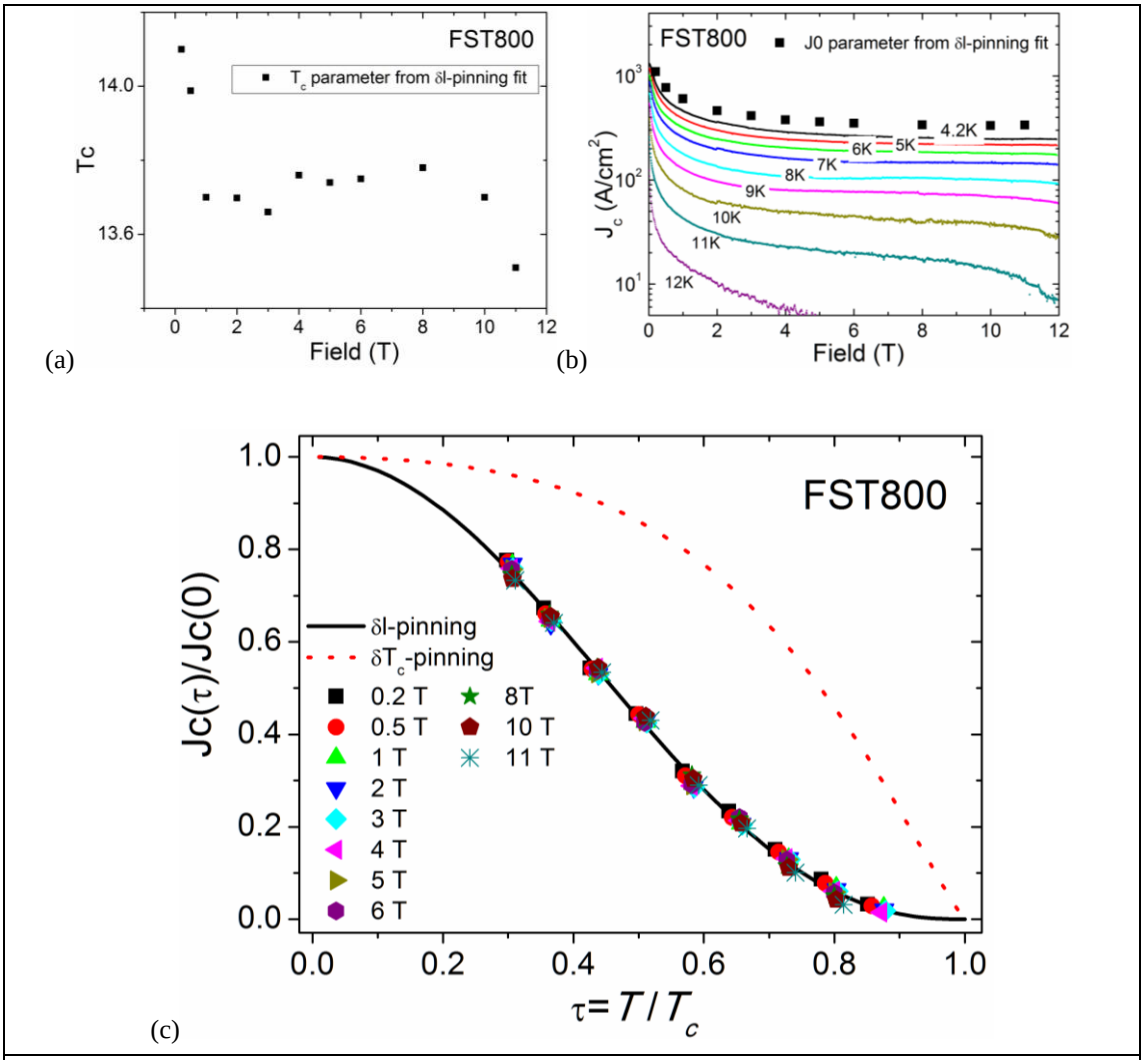


Figure 26: sample FST800 (a) $T_c(0)$ fit parameter obtained fitting the data with $\delta l$-pinning model (b) *J0* fit parameter obtained fitting the data with $\delta l$-pinning model together with $J_c$ measured values from 4.2 K to 12 K (c) normalized $J_c(\tau)$ data obtained from magnetization curves at several fields as a function of the reduced temperature τ. The continuous and dotted lines are the theoretical curves expected within the scenarios of $\delta l$ and $\delta T_c$ pinning models respectively.

The same approach within the Griessen framework has been applied to measurements on sample FST800 and the corresponding results are shown in Figure 26. Also in this case we find a perfect agreement of data to $\delta l$-pinning model in Figure 26(c) and convincing $J_c(0)=J_0$ and $T_c(0)$ parameters values in Figure 26(b) and Figure 26(a) respectively. Regarding $T_c(0)$ values, it is tempting to interpret their trend versus magnetic field as an index of sample granularity and thus of weak links that are demolished as the field is increased, and after all this is in agreement with the structural analysis performed on the sample. Contrarily to what found for samples FST970B, in sample FST800 the accordance of data with $\delta l$-pinning model is not in agreement with the Dew-Hughes analysis of the $f_p$ curves. It is important to note that in Figure 24(b) only curves at 10 K and 11 K are shown, as it was not possible to extrapolate $H_{irr}$ values at lower temperatures for this sample. The different morphology between the samples and, in particular, the presence of several impurities along the grain boundaries of the FST800 may contribute to a different behaviour of the $f_p(h)$ dependence. Of course nothing can be said on sample FST800 regarding the shapes of the normalized pinning curves at lower temperatures, and the presence of a non-scaling and thus of different pinning mechanisms acting at different temperatures [26]-[28] is plausible.

It is important to underline that in the $f_p$ curves of both samples, and especially of sample FST800, the $\delta l$ and $\delta T_c$ contributions, respectively, are probably not sufficient to describe the overall pinning individually, and it would be necessary to take into account a more complex variety of pinning landscapes and/or more than one pinning component [10].

It is interesting to underline that the Dew-Hughes model has been developed in the frame of the single-vortex regime, i.e. neglecting the inter-vortex interactions [19],[16]. The validity of this approximation seems to be fulfilled by the quite good fit of $f_p$ obtained for sample FST970B, and this result is confirmed in the magnetic relaxation study reported in the next section. Regarding sample FST800, as the values obtained for the $p$ and $q$ parameters do not correspond to any of the standard configurations foreseen in the Dew-Hughes model, it seems that this model, or at least its basic single component version, is not adequate to describe pinning inside this sample, where there are probably present different and not-independent pinning mechanisms.

#### 4.3.1.4 Relaxation magnetization

Beyond the magnetization curves, a useful approach for investigating the vortex dynamics is the study of the relaxation processes of the magnetization. The critical state in the vortex lattice, which determines the hysteresis of the magnetization in type-II superconductors, is a metastable state. It follows that vortices tend to hop out of their pinning potential well in order to reach the configuration of absolute minimum energy. Such motion usually arises from thermal activation, but it can arise form quantum tunnelling (at low temperature) or can be stimulated by external perturbations, such as microwave shaking of the vortex lattice [29]. Magnetization relaxation processes have been observed in various low-temperature superconductors, and the subject has become of even greater interest after the discovery of high-$T_c$ superconductors, because of the higher operating temperature and of the small

activation energies related to the short coherence length and the large anisotropy [30].

The concept of thermally induced hopping of the flux lines has been first treated by Anderson and Kim [31]. In the framework of their model a logarithmic dependence of the magnetization M on the time *t* is expected and this behaviour has been verified in various superconductors, both low-$T_c$ and high-$T_c$. This result is based on two basic assumptions: (i) the pinning potential energy barrier height decreases linearly with the current density: $U=U_0(1-J/J_c)$, where $U_0$ is the barrier height in the absence of a driving force; (ii) $U_0/k_BT \gg 1$, which allows hypothesis that the thermal induced hopping rate is proportional to the Arrhenius factor $\exp(-U_0/k_BT)$.

However, in many experiments, deviations from the logarithmic dependence of *M* (and thus of the linear dependence of *U* on *J*) have been observed, indicating that is just a first-order approximation whose validity has been demonstrated to fail many times [30]. In general *U*(*J*) is a non-linear function.

Maley *et al.* [32] proposed a technique for an experimental determination of *U*(*J*), based on the analysis of the flux creep measurements. From the rate equation for thermally activated flux motion [33] they showed that $U=AT- k_BT \ln|dM/dt|$, where A is a time independent constant. Both $k_BT\ln|dM/dt|$ and $M_{irr}\sim J$ can be experimentally determined. In fact, it is possible to measure the magnetic relaxation curves $k_BT\ln|dM/dt|$ versus $M_{irr}$ at different temperatures, where the principal effect of increasing temperature is to produce monotonically decreasing initial values of *M*. As *M* decreases, the slope *dU*/*dM* becomes progressively steeper. A constant value A multiplied by *T*, added to each of these data set will produce values equal to $U/k_B$ for each temperature, so, up to an additive constant A*T*, all magnetic relaxation curves will all fall on the same *U*(*M*) curve. The explicit temperature dependence of *U*(*M*) over the measurement temperatures range should be insignificant compared with the variations brought about by changes in the range of *M* values sampled at each temperature, which means that the temperature dependence of *U*(*M*) should be weak [32].

In this section the study of the vortex dynamics in sample FST970B performed by relaxation magnetization measurements over a period of time up to 7200 s is reported. Measurements at 5 T and 0 T have been performed in the trapped flux configuration, by ramping the field at 6 T (1 T) after zero field cooling (1 T/min), then slowly decreasing the field down to 5 T (0 T) (0.05 T/min), and collecting the measurements as soon as the target field had been reached. As a general trend, a logarithmically decay of moment versus time (for times greater than 100 s), at both 0 T and 5 T, was observed.

Assuming a thermal activation process over the flux creep activation barrier *U*(*M*), the dynamical equation for *M* can be solved with logarithmic accuracy, yielding $U(M) = k_BT\ln(t/t_0)$. Following the procedure proposed by Maley *et al.* [32] the plots of $k_BT[\ln|dM/dT|-A]$ vs. *M* at different temperatures can be used to reconstruct the dependence of the activation barrier *U* upon *J*. It is here assumed the Tinkham approximation [34], where the *U*(*T*,*H*) function can be factored into two contributions: $U(T,H) = U_0(H)g(t)$, where $g(t) = (1-t^2)(1-t^4)^{1/2}$, (with $t= T/T_c$ ). The results are reported in Figure 27 for sample FST970B, scaled considering A = 20 for

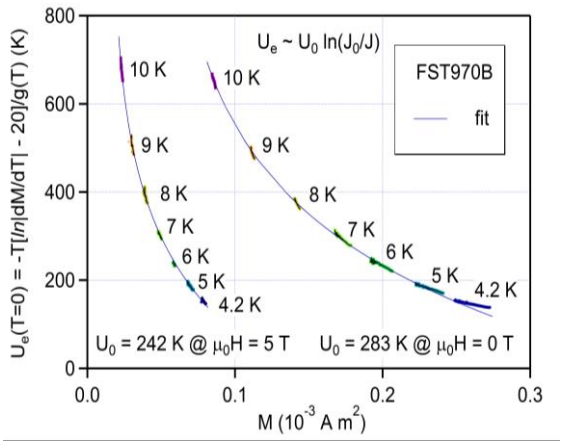


Figure 27: Dependence of the thermally activated barrier $U_0$ upon magnetization, calculated in the framework of the Maley model, scaling the data at different temperatures for sample FST 970B.

both zero field and $\mu_0 H$ = 5 T cases. As it can be clearly seen, the activation barrier is a monotonic function of $M$, in agreement with the logarithm dependence proposed by Zeldov *et al.* [35]. Data in Figure 27 have been fitted supposing $U = U_0 \ln(M_0/(M-\alpha))$. In the zero applied field case, we found $U_0$ = 283.6 K, $M_0$ =0.34 emu and $\alpha$ = 0.052 emu, whereas in the presence of a field of 5 T we found $U_0$ = 242.5 K, $M_0$ = 0.12 emu and $\alpha$ = 0.016 emu.

The logarithmic dependence of $U$ upon $M$, extrapolated from magnetic relaxation measurements, is a good approximation for the creep activation barrier in the single vortex creep regime [36]. Therefore our results indicate that in the FST970B the motion of flux lines develops in the single-vortex pinning limit even in magnetic fields up to 5 T, which means that intervortex interactions, typical of collective pinning theories, can be neglected. This is in agreement with the fit results obtained in the previous paragraph for this sample in the framework of the Dew-Hughes model. A similar behaviour has been evidenced on films of the same material [37], but it cannot be neglected that a very important role regarding films is played by the substrate, which is able to introduce a strain during the material growth with a related defect structure. Moreover analogous results were observed on single-crystals of the same iron-chalcogenide compound with a slightly different stoichiometry [16]. In our case the simple bulk FeSeTe sample (FST970B) appears to be in the single vortex pinning regime up to 5 T, and this confirms that this material has high potential application , and if optimized, it would be able to carry high $J_c$ up to high magnetic fields. See for example the coated conductors case presented in ref. [38].

### 4.3.2 Sample FST970

This paragraph presents the properties of a $FeSe_{0.5}Te_{0.5}$ polycrystalline sample manufactured by a steps solid state reaction route as described in Chapter 2. The dependence of the magnetic moment $m$ on the applied magnetic field $H$ (up to 18 T), the temperature $T$ and the relaxation time $t$ was investigated. The resistance as a function of $T$ and the specific heat versus $T$ up to 16 T were measured. The experimental results are discussed with particular attention to the pinning properties of the sample with the aim to correlate the fabrication process with the pinning landscape and/or with the vortex dynamics.

### 4.3.2.1 Structural characterization and compositional analysis

In order to recognize the phases' formation inside the sample, following its evolution due to HTs, X-ray diffraction patterns of the material after each HT were recorded at room temperature.

In Figure 28 XRD measurements obtained on pellets after each HT are shown, together with the indication of the phases corresponding to the revealed peaks. The indexes of the FeSeTe reflections correspond to the tetragonal space group P4/nmm and few impurities and spurious phase are still present after the first HT, such as iron oxide and hexagonal phase. After melting, the sample grew with a preferential orientation along the *c*-axis, as can be deduced from the fact that the (00l) peaks are more intense than the off axis peaks, in contrast to what happens with random powder or polycrystalline samples [4]-[6],[8],[9]. Only some residuals of the polycrystalline phase are detectable in the pattern and the sample is likely to be composed of few epitaxial crystalline domains aligned along the *c*-axis.

SEM imaging of the pellet surface after second HT are shown in figure 29(a) and (b) at two different magnifications and are coherent with the XRD results. The first micrograph shows the terraces typical of the layered structures with some defects and residuals of the fused phase. Grains size are around 250 μm x 150 μm. In Figure 29(b) an higher magnification of the sample is presented, in which a very flat surface is

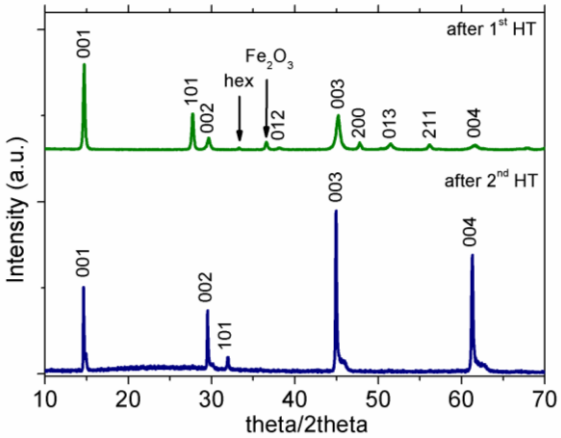


Figure 28: XRD patterns of FST970 sample after the first and the second HT. Intensities are normalized to the peak (001) and shifted for an easy comparison.

revealed. The chemical composition of the sample has been determined by EDX analysis, averaging on areas of about 1.4 mm x 1 mm and normalizing to the sum Se+Te. On average, the refined composition is $Fe_{1.07}Se_{0.37}Te_{0.63}$ indicating an excess of iron which is coherent with the $T_c$ values that will be reported in the following. It has been shown that reducing the Fe excess fosters the occurrence of superconductivity and weakens the antiferromagnetic order [11],[12],[16] even if according to the phase diagram of the compound [39], a little Fe excess is needed to stabilize the structure. Moreover some authors [24] have hypothesized that the iron excess, introducing defects into the crystal structure, promote higher pinning potential into the system. Both the effect of reducing the Fe excess and increasing the Se content prevent Fe to occupy the additional site and result in shrinking and reshaping the $FeTe_4$ tetrahedra [12]. In this case, starting from the nominal composition $FeSe_{0.5}Te_{0.5}$, with a Fe:(Se,Te) ratio of 1:1, the system found its equilibrium lowering the Se content, which is coherent with the measured Fe excess.

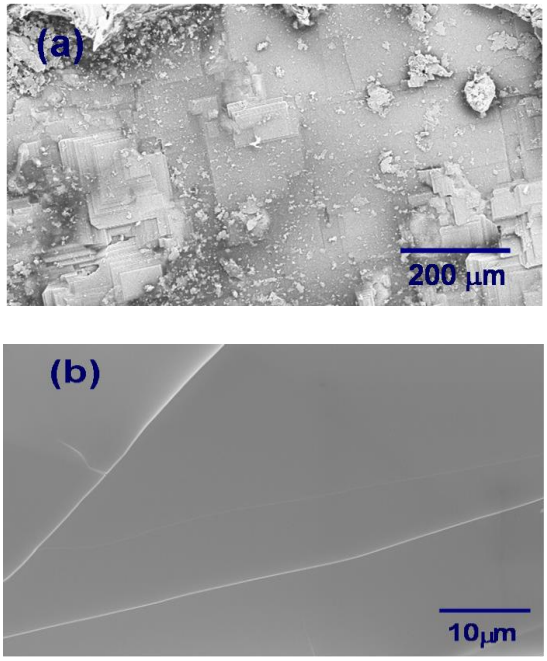


Figure 29: SEM images at two magnifications of FST970 sample surface after second HT. Measurements system HR-FEG-SEM Leo 1525. In-lens secondary electron, aperture size 60 µm.

#### 4.3.2.2 Magnetic, transport and calorimetric measurements

Measured FST970 sample has dimensions 3 x 3.35 x 0.14 $mm^3$ and measurements where carried out with magnetic field perpendicular to the sample surface and parallel to the *c*-axis.

The relaxation of magnetization was studied over periods of time up to 7200 s, for fixed values of temperatures. As for sample FST970B, two configurations were considered: zero field, and 5 T background magnetic field in the trapped field configuration. In order to collect data in the trapped field configuration at 5 T, the sample was first cooled in zero field conditions; then, the background field was increased from zero to 6 T with a field ramp of 0.5 T/min; finally, the field was slowly decreased (0.1 T/min) to 5 T, with recording of data soon after the 5 T target field was reached. To collect data in the trapped field configuration at zero field, an analogous procedure was applied, increasing the field to 1 T and decreasing successively to zero T.

The isothermal magnetization measurements were performed in the range of temperatures from 4 K to 13 K. In the range 4-9 K, the hysteresis loops were collected up to 18 T, whereas above 9 K the maximum applied field was 12 T. The magnetic field sequence was as follows: Zero Field Cooling (ZFC) → $B_{max}$ → $-B_{max}$ → 2 → 0 T, where $B_{max}$ = 18 T (4-9 K) or $B_{max}$ = 12 T (9-13 K).

The ZFC susceptibility curves at 0.001 T, 0.05 T and 1 T are shown in Figure 30. The transition temperature, at each field, is determined as the value of the temperature corresponding to the onset of the ZFC moment drop. In particular, the curve at 0.001 T shows a diamagnetic onset at about 14 K, while the transition width corresponds to $\Delta T_c \equiv$ T(90%)-T(10%) $\approx$ 1.3 K. It is observed that, at $T>T_c$, the behaviour of the curve measured at 1 T is compatible with a small ferromagnetic response; this is coherent with the ferromagnetic background that has been found for

this sample by means of hysteresis cycles above the transition temperature. The results for the hysteresis cycle measurements at different temperatures are shown in Figure 31. The very small tilt of the loops at superconducting temperatures is due to the ferromagnetic background at $T>T_c$, measured and shown in the inset of Figure 31. Increasing the temperature, the pinning becomes weaker and consequently the width of the loops decreases.

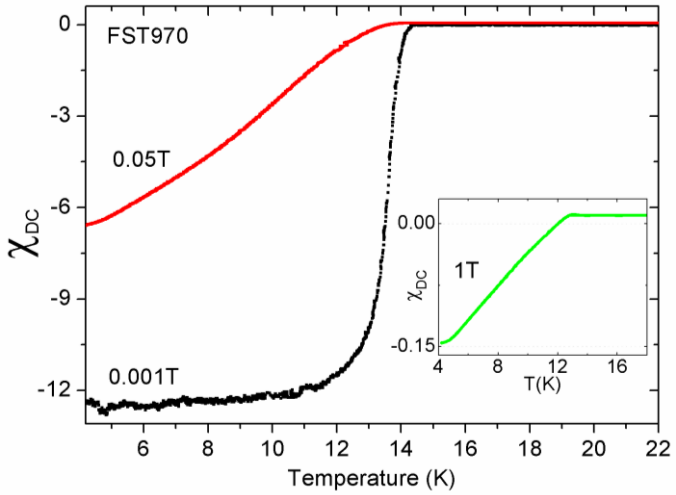


Figure 30: Temperature dependence of the ZFC DC volume susceptibility (without demagnetization correction) obtained for sample FST970 at 0.001 T and 0.05 T. In the inset the result obtained at 1 T is shown.

A second peak in the $m(H)$ curves is clearly observed up to temperatures close to $T_c$. It is worth to underline that this result is not altered by the eventual presence of a paramagnetic like background arising from the experimental setup, and rely only on the separation between the positive and the negative branches of the magnetic-moment loop. Hysteresis cycles from 4.2 K to 9 K have been in fact measured with both the VSM systems obtaining the same results, including the presence and the positions of the second peaks in the $m(H)$ curves. The peak extension in the magnetization curves of this sample is quite impressive, going from low temperatures up to temperatures close to $T_c$ and reaching a large range of fields in which the $J_c$ is potentially enhanced.

Among the complex vortex phenomena, second magnetization peak (also known as fishtail) effect in the field dependent magnetization measurements is intriguing and widely observed in various kind of type II superconductors, including low-$T_c$ superconductor $Nb_3Sn$ [40], high-$T_c$ cuprates $YBa_2Cu_3O_{1-\delta}$ and $Bi_2Sr_2CaCu_2O_y$ [41]-[43] , $MgB_2$ [44] and the recently discovered high-$T_c$ iron-based superconductors [16], [23],[45]-[51]. The occurrence of peak effect shows strong system-specific feature. In cuprates, different vortex dynamical mechanisms including crossover from elastic to plastic (E-P) vortex creep [42], vortex order-disorder phase transition [52], vortex lattice structural phase transition [53], surface barriers [54], samples granularity and inhomogeneities in the oxygen content [41], were proposed in its interpretation. In iron pnictides, the peak effect has been observed in all of the four main systems, 1111-type SmFeAs(O,F) and NdFeAs(O,F) [46],[55], 122-type $(Ba,K)Fe_2As_2$, $Ba(Fe,Co)_2As_2$ and $(Ba,Na)Fe_2As_2$ [47],[50],[56], 111-type LiFeAs [51], and 11-type

$Fe_{1+x}$(Te,Se) [23],[16],[57],[58]. However, similar as cuprates, different explanations were proposed [45],[46],[51],[55]. A widely applied model is the idea of an elastic to plastic vortex creep crossover. In 111-type LiFeAs, supported by the strong temperature-dependent peak position $H_{peak}$, vortex lattice structural phase transition model was applied [51]. In the more anisotropic 1111 system, a three-dimensional (3D) ordered to 2D disordered vortex lattice transition was suggested [46],[55]. In 122-type $Ba(Fe,Co)_2As_2$, controversial models of both collective to plastic crossover and vortex lattice structural phase transition were proposed [45]. Because of the various possibilities, no general consensus or clear understanding has been yet reached about the underlying mechanism of the second peak occurrence. In comparison with cuprates, the less anisotropy $\gamma$ and larger coherence length $\xi$ in iron-bases superconductors, combined with the moderate $T_c$, jointly provide opportunities to explore vortex physics between LTS and high-$T_c$ cuprates [59].

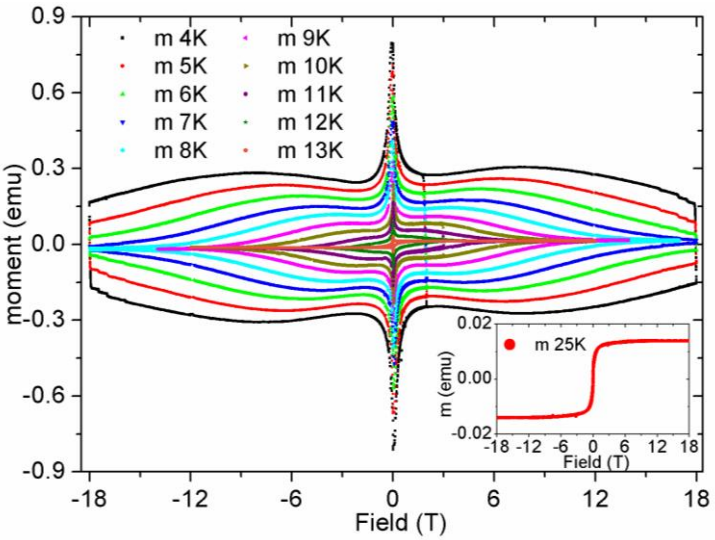


Figure 31: Magnetic moment versus external field curves obtained at different temperatures in sample FST970. In the inset the background cycle measured at 25K is shown.

From the $m(H)$ curves measured at different $T$, it is derived the temperature dependence of the magnetic field value corresponding to the second peak in the magnetization, $H_{peak}$ and also to the onset of the peak, $H_{onset}$. The results are shown in Figure 32.

It is found that, for the investigated sample, the position of the second peak shifts toward lower fields monotonically on increasing the temperature, in analogy to what was observed in the $YBa_2Cu_3O_{7-\delta}$ superconductor [60]. Indeed the black continuous line in Figure 32 is the best fit curve obtained supposing the same T dependence of $H_{peak}$ as observed for $YBa_2Cu_3O_{7-\delta}$ [41] and as already found for $FeSe_{0.3}Te_{0.7}$ up to 3 T [16]: $H_{peak}=H_{peak}(0)(1-T/T_c)^{3/2}$, where $H_{peak}(0)$ is a constant and $T_c$ is the temperature at which the peak is undetectable. The best fit parameter are $H_{peak}(0)$ =10.9±0.2 T, $T_c$ =12.5±0.2 K. This remarkable similarity between the result obtained in the $YBa_2Cu_3O_{7-\delta}$ and in FeSeTe superconductors, might suggest that the peak effect in the two systems could have an analogous origin. Klein *et al.* [41] claimed that the peak effect in untwined YBCO crystal could be due to the sample granularity, that is to the suppression of superconductivity in some regions as the field increases and to the consequent transformation of these zones into efficient pinning centres. Indeed for

the sample under investigation, the structural characterization has shown that this sample is granular. The granularity here means that the flux penetrates into different grains of the sample independently, and it leads to a reduction of the measured magnetization above $H_{peak}$. This has as a consequence that $H_{peak}$ could be related to the upper critical field of these regions. This is only one of the possible explanations of the peak effect in this sample, in agreement with the structural characterization and with the behaviour of the peak position versus $T$ in magnetic measurements shown in Figure 32.

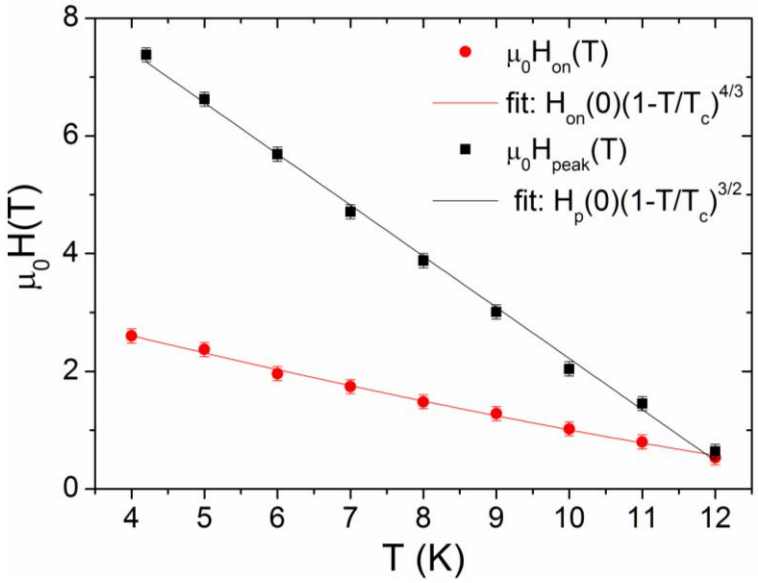


Figure 32: Temperature dependence of the magnetic field value at which the peak maximum and the peak onset occur for sample FST970. Continuous lines are the best fit curves obtained supposing the same T dependence observed in [45], [23] and $YBa_2Cu_3O_{7-8}$ [41].

Concerning the behaviour of $H_{onset}$ as a function of temperature, following Prozorov *et al.* [45] and Das *et al.* [23] a good fit was found with $H_{onset}=H_{on}(0)(1-T/T_c)^{4/3}$ with $H_{on}(0)=3.85\pm0.2$ T which is represented by the red continuous line - together with experimental data in Figure 32. As observed for the temperature dependence of $H_{peak}$ also the temperature dependence of $H_{onset}$ line is similar to the one reported for the untwined YBCO crystal in [41].

As the sample investigated is not a single crystal, it would be not appropriate to extract the $J_c$ curves from the $m(H)$ curves using the Bean critical state formulas, for the same reasons described for samples FST800 and FST970B in the previous paragraph. Anyway the symmetric magnetization curves suggest dominant bulk pinning instead of surface barriers, which guarantees the application of Bean critical state model in the $J_c$ calculation. Therefore the $\Delta M$ curves, that correspond to the differences between the positive and the negative branches of the magnetization loops at the different temperatures, are considered, which are proportional to the $J_c$ values at the same temperature. These curves are shown in Figure 33. From the $\Delta M$ profiles it is possible to study the mechanism that rule the pinning in this FeSeTe superconductor, as it will be shown in the following.

In Figure 34(a) the resistance curves $R(T)$ as a function of the temperature at magnetic fields from zero to 12 T are shown. The superconducting onset is at about 15 K, while the critical temperature ($T_c$), has been estimated with a standard 50% criterion of the normal state resistance ($R_N$). It results a $T_c$ of about 14.6 K for FST970, in good

agreement with what reported in literature [13],[14],[9]. The diamagnetic onset is consistent with the result obtained with the transport measurement, however the main difference in measured values can be ascribed to the usual imbalance coming from the intergranular and intragranular contributions of polycrystalline samples. Since in a bulk sample the distance between the voltage taps doesn't necessarily correspond to the path followed by the current, the absolute values of the critical current ($I_c$) are not relevant, and the results in Figure 34(b) were normalized to the maximum $I_c$ at the lowest temperature and $B$=0 T to observe only the trend.

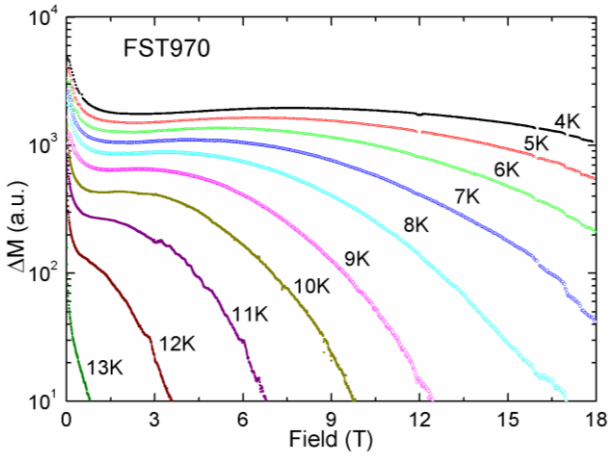


Figure 33: Field dependence of the Δ$M$ profiles at different temperatures in sample FST970.

Magneto-resistance measurements provide also the magnetic field-temperature phase diagram. The $\mu_0 H_{c2}$ has been defined by the standard 90% criterion of $R_N$, while $\mu_0 H_{irr}$ has been determined by the 10% criterion of the normal state resistance. For sample FST970 the superconducting transition width $\Delta T_c$ calculated as $T_c(90\%R_n)$-$T_c(10\%R_n)$ at 0 T is about 0.8 K and at 12 T is about 1.7 K. This results can be interpreted as a sign of the presence of some non-homogeneities inside the sample, beside the good value of the superconducting onset.

From calorimetric measurements the upper critical field was also measured and the specific heat results are presented in Figure 35. The broadness of the transitions at all fields is an index of the non perfect homogeneity of the sample, in agreement with the transport measurements results. In fact, the broadness of the transition, estimated as $\Delta T_c \equiv T_{onset}$-$T_{c0}$ gives quite the same results for the $R(T)$ and the calorimetric measurements, that is $\Delta T_c \approx 1.3$ K at zero field and $\Delta T_c \approx 1.8$ K at 12 T. In Figure 35, for each field, the temperatures at the elbows of the curves represent the thermodynamic transition temperatures from the normal to the superconducting state. Thus, the magnetic field corresponding to the temperatures at the elbows of the curves represent the upper critical fields values at each temperature.

These data, together with the irreversibility line and the upper critical field obtained from transport measurements, and the $H_{peak}$ and $H_{onset}$ versus temperature collected from isothermal magnetization measurements, are shown in the H-T phase diagram of Figure 36. Beside the perfect agreement between $H_{c2}$ obtained from transport and calorimetric measurements, from this diagram it is possible to appreciate the high upper critical field slope near $T_c$ ($dH_{c2}/dT|_{Tc}$), which results ~ 9.5, in good agreement with literature [10],[61],[62].

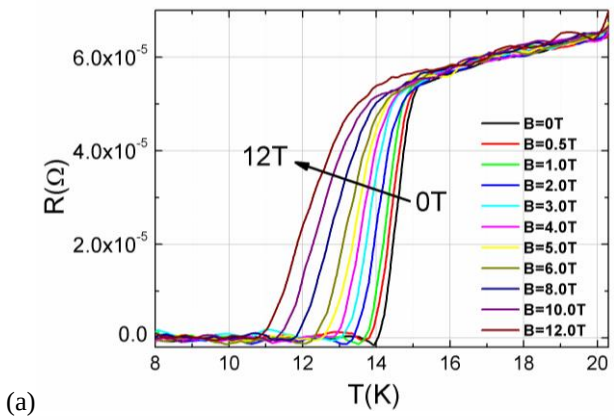


(a)

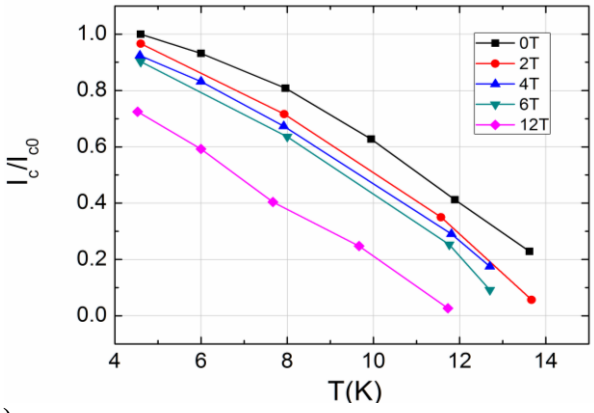


(b)

Figure 34: sample FST970 (a) Resistance as a function of the temperature curves for 0, 0.5, 1, 2, 3, 4, 5, 6, 8, 9, 10, 12 T applied magnetic field. (b) normalized critical current versus temperature estimated from resistance measurements at several currents with 1 μV/cm criterion.

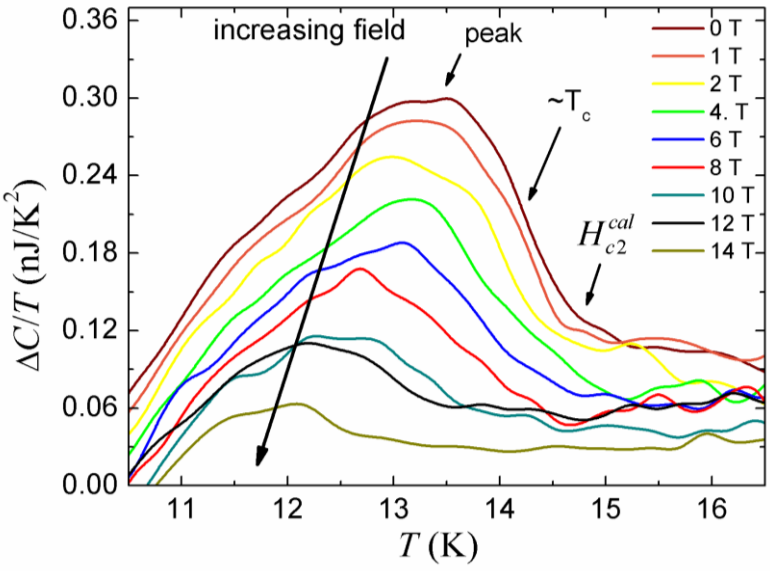


Figure 35: calorimetric measurements for sample FST970 from zero field up to 14 T.

The phase diagram in Figure 36 is coherent with the behaviour ascribed to iron based superconductors, which are materials with intermediate properties between low-$T_c$ and high-$T_c$ superconductors [63]-[65]. The ratio between the irreversibility field $H_{irr}$

and the upper critical field $H_{c2}$ is large due to thermodynamic fluctuation. The $H_{c2}$ and the irreversibility line are in fact separated as in high-$T_c$ superconductors. The concavity of $H_{c2}$ curve, similar to that of low-$T_c$ superconductors, reflects what it is expected from the s± symmetry of the order parameter [65]-[68].

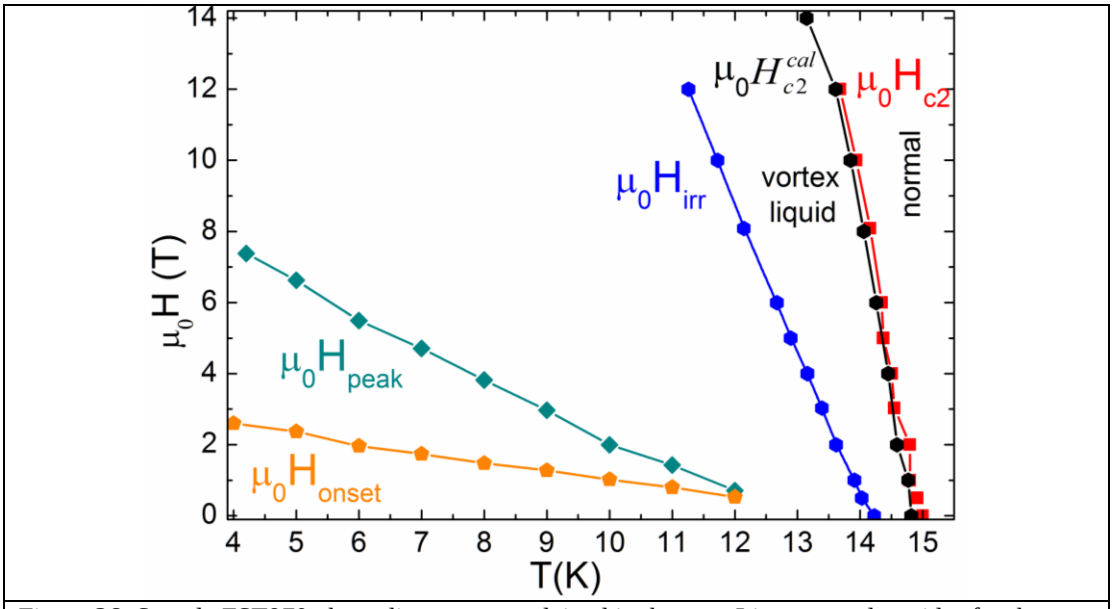


Figure 36: Sample FST970 phase diagram as explained in the text. Lines are only guides for the eye.

On the other hand, the irreversibility line shows an inverse convexity typical of high-$T_c$ superconductors. Below this line it is present a wide region in which the vortex dynamic can be investigated, and, for this sample in particular, this region is characterized by the peak effect. In Figure 36 the lines are only guides for the eye. Anyway also $H_{c2}$ and $H_{irr}$ have been fitted with the functional form $H_x=H_x(0)(1-(T/T_c)^p)^n$, finding $H_{c2}(0)=142.4$ T with $p=1$ and $n=4/3$, $H_{irr}(0)=37.7$ T with $p=2$ and $n=1.16$, in good agreement with literature [23],[45],[56].

As already underlined, the origin of the peak effect in iron-chalcogenides superconductors is still an actual and controversial issue, and there are several different interpretations that are being given in literature [16],[23],[41],[42],[52]-[54],[57]-[59] to clarify its causes. In general, if present, it is observed deeply within the mixed state and it is associated with a concomitant increase of the vortex pinning energy and hence an anomalous modulation of $J_c$ [23]. The second peak position moves up quickly as temperature decrease and quite resembles that in $YBa_2Cu_3O_{7-x}$, 122-type and other 11-type iron-based superconductors [23],[42],[48] so that it could imply an analogous origin of the peak effect. Among other interpretations, the existence of an elastic to plastic (E-L) transition in the vortex lattice regime is in fact one of the most accredited [42], and applied to iron-based superconductors very recently [59]. An explanation of why the peak effect usually takes place in layered superconductors, such as sample FST970, has been given in [59]: when the applied field is perpendicular to the surface plane of a layered superconductor, the rigidity of the single flux is dependent on the coupling between superconducting layers. If the coupling is weak and the single flux is soft, the flux line is easy to be distorted, and can translate from elastic to plastic vortices. In [59] is also pointed out that the above mentioned factors is premised on good sample crystalline quality (uniform superconductivity). Generally, for polycrystalline sample, the $T_c$ distribution is broad,

which thereby causes no observation of peak effect or only weak trace of it. This observation points toward the good quality of sample FST970, despite its polycrystalline nature.
Of course, in order to understand and discriminate if this transition in the vortex lattice could be the origin of the peak effect in sample FST970, several characterizations should be given to support this hypothesis.
Since the occurrence of the second peak in the magnetization loop is quite advantageous in view of practical application and investigation of its origin is also helpful for understanding the fundamental question underlying vortex physics, a study of vortex pinning and magnetic relaxation on this sample was also performed. Thus, some of the characterizations needed to understand the origin of the peak effect have been actually performed, and the results will be shown in paragraph 4.3.2.4, further on in this Chapter. In general, for a deeper understanding of the origin of peak effect in these materials, also further investigations employing microscopic measurements tools such as neutron scattering, scanning tunnelling microscope etc. would be necessary [56].

### 4.3.2.3 Pinning properties

The importance of studying the pinning properties of samples under analysis as been already elucidated regarding samples FST800 and FST970 in the previous paragraph. Therefore the magnetic field dependence of the pinning forces and of the normalized pinning forces densities ($f_p=F_p/F_{p,max}$) as a function of the normalized magnetic field ($h=H/H_{irr}$) at several temperatures has been investigated. Here $H_{irr}$ is defined as the $H$ value at which $J_c=0$. As in the previous paragraph, starting from the experimental $J_c(H)$ curves (or from the $\Delta M$ curves in our case), $H_{irr}$ has been determined as the extrapolated zero value in the so called Kramer plot [22], where $J^{1/2}\,H^{1/4}$ is plotted as a function of $H$. The $F_p(h)$ and the normalized $f_p(h)$ curves of FST970 sample have been extracted from magnetic measurements and the results are shown respectively in

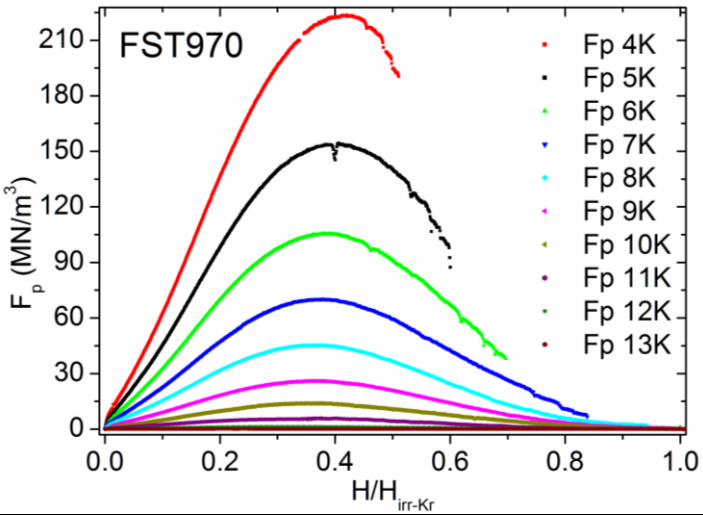


Figure 37: Pinning forces from 4 to 13 K as a function of normalized magnetic field for sample FST970.

Figure 37 and in Figure 38. In comparison with samples FST970B and FST800, whose behaviour was shown in previous paragraph in Figure 24, this sample shows slightly stronger pinning.

In contrast to the usual scaling of the $f_p$ curves at different temperatures, pinning curves of sample FST970 presented in Figure 38(a) show a very small but still non-negligible shift in their maximum toward low reduced fields while temperature is increasing from 4 K to 11 K. This anomaly in the temperature dependence reflects the presence of different pinning centres and/or mechanisms as a function of the temperature [10],[17],[69]. The function $f_p(h)$ is in fact peaked around $h$=0.4 for temperatures from 4 K to 11 K, while the peak starts moving to lower reduced fields while approaching $T_c$, and it is found around $h$=0.21 at 13 K.

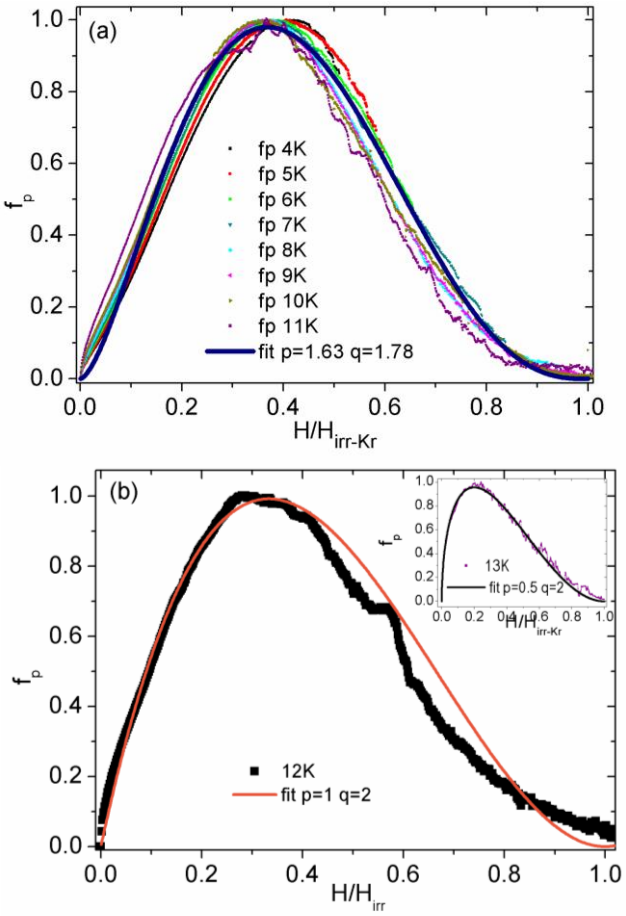


Figure 38: (a) Normalized pinning forces from 4 to 11 K as a function of normalized magnetic field for the sample FST970 shown together with the fitting line. (b) Normalized $f_p$ at 12 K and its fitting curve are shown, while in the inset the $f_p$ and the fit at 13 K are presented .

The fitting procedure of the whole set of experimental $f_p$ curves from 4 K to 11 K was done, and found as best fitting parameters $p$=1.63 and $q$=2.78. The $f_p$ curve at 12 K is shown together with the fit for $p$=1 and $q$=2 while the $f_p$ curve at 13 K is fitted well with $p$=1/2 and $q$=2. In the framework of the Dew-Hughes model [19], it seems that pinning in sample FST970 could be due to the spatial variations in the carrier mean free path $l$ ($\delta l$ pinning) and, for temperatures up to 11 K, one can talk about core interaction with normal point defects. Nevertheless as the $p$ and $q$ parameters assume values that do not correspond to any standard pinning centre in the Dew-Hughes model, it is evident that a single type of pinning centre is not sufficient to describe the overall pinning and point pins alone cannot rationalize the observed scenario [10],[17],[23],[69]. It would be necessary to take into account a more complex variety

of pinning landscapes and/or more than one pinning component. At 13 K the pinning curve is more likely to be related to surface normal pins [19].

As already evidenced in the previous paragraph about sample FST800, a similar temperature non-scaling behaviour has been already found in iron-chalcogenides samples [10],[17] and it has been ascribed to the multi-domain nature of the samples, which could be likely to result in aggregates of domains, which contribute both interdomain and intergrain critical current. Also here, it is worth mentioning that $h_{max}$ remains highly sensitive to the proper determination of $H_{irr}$.

As previously done in the paragraph regarding samples FST970B and FST800, also for this samples a comparison with the theoretical approach proposed by Griessen *et al.* [16],[25] has been done in order to understand the nature of pinning in more detail. In Figure 39 the normalized $J_c(\tau)$ data obtained from magnetization curves at several fields are plotted, along with the theoretical curves expected within the scenarios of $\delta l$ and $\delta T_c$ pinning [25]. Data are normalized using the $J_c(0)=J_0$ values obtained from the fit to the expression for $\delta l$-pinning. Despite the apparent perfect agreement of data with the theoretical curve for $\delta l$-type weak pinning shown in Figure 39 in the very broad range of magnetic fields from zero to 18 T, the values obtained with this model for the fitting parameter $T_0$ at fields below 2 T appear meaningless. This parameter should in fact correspond to the transition temperature at each field and should consequently decrease monotonically as the magnetic field increases.

Regarding FeSeTe samples, it is important to underline again the variety of opinions that can be found in literature: $\delta l$-pinning behaviour for several stoichiometries has been claimed by several authors [16],[23],[24], while others found out a prevalent $\delta T_c$-pinning [70] in their samples. Sun *et al.* [57] on the other hand proved that in their well annealed and high quality single crystals $\delta l$ and $\delta T_c$ pinning coexist. Some of these controversy could be ascribed to differences in samples quality.

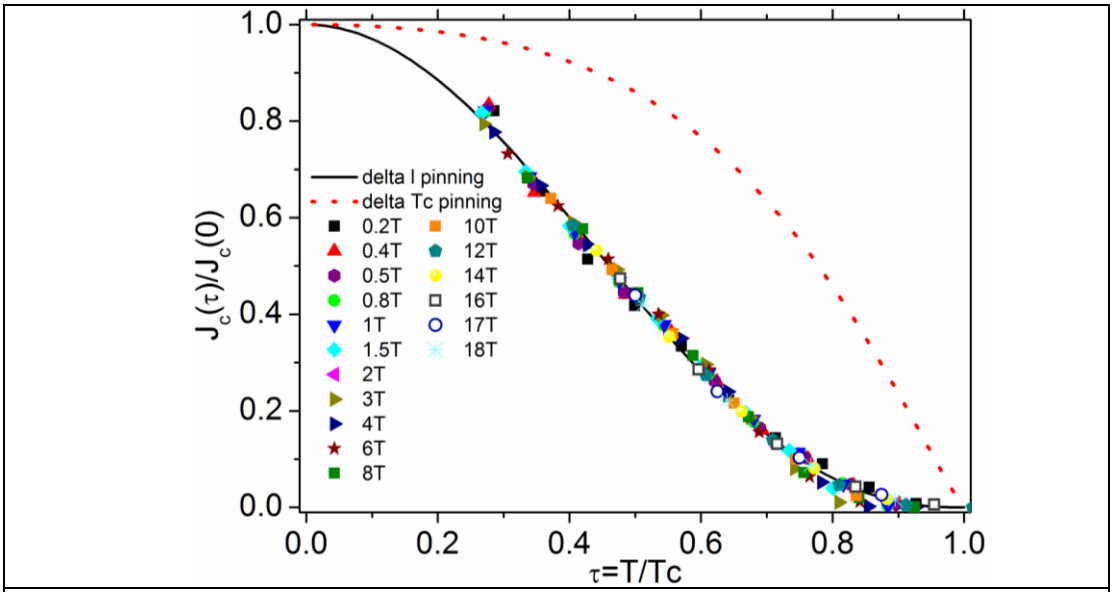


Figure 39: Normalized $J_c$ data, as a function of the reduced temperature τ, obtained at $\mu_0 H$ = 0.2, 0.4, 0.5, 0.8, 1, 1.5, 2, 3, 4, 6, 8, 10, 12, 14, 16, 17 and 18 T. The continuous and dotted lines are the theoretical curves expected respectively in case of $\delta l$ and $\delta T_c$ pinning [25].

On this basis a data fitting with other models as well has been tested. In Table IV-1 the $J_c(\tau)/J_c(0)$ vs. $\tau$ dependence is briefly described for all models under investigations, [20],[21],[25],[71]-[73].
In Figure 40(a) and 40(b) the fit parameters values obtained within the 3 models for $T_0$ and $J_0=J_c(0)$ respectively are shown. As already anticipated, the values obtained for $T_0$ within the $\delta l$-pinning model show a meaningless increase with the field up to 2 T, and the same happens in this field range for the values obtained within the *giant-flux creep* model.

| **Pinning Model** | ***δl-pinning*** | **Ginzburg-Landau** | **Giant-flux creep** |
|---|---|---|---|
| $J_c(\tau)/J_c(0)$ | $(1-\tau^2)^{5/2}/(1+\tau^2)^{1/2}$ | $(1-\tau^2)/(1+\tau^2)$ | $(1-\tau^2)^2$ |
| **description** | Within the collective pinning → vortices pinned by randomly distributed weak pinning centers, related to local variations of $l$ | Classical pinning theory – core interaction | even at $T$ far below $T_c$ → fast magnetic relaxation which proceeds nonlinearly in the time logarithm: very large creep rates, characteristic of the oxide superconductors. |

Table IV-1: pinning models sketch.

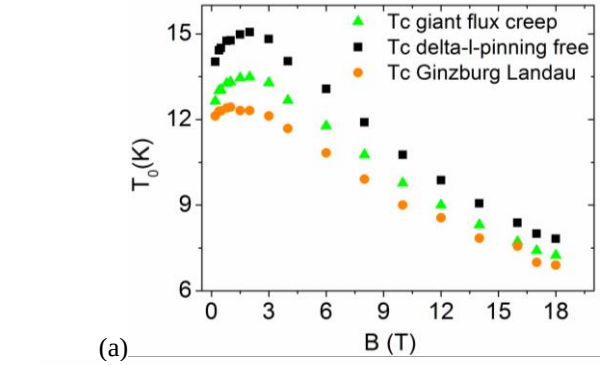


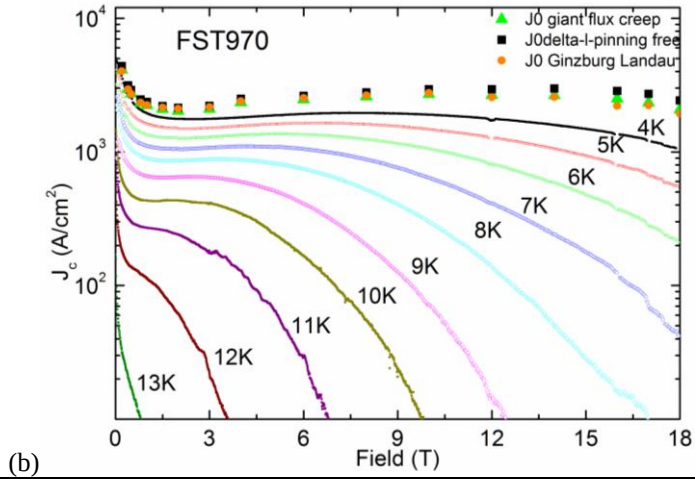


Figure 40: (a) Values obtained within each of the 3 models for the parameter $T_0$ at each investigated field. (b) Values obtained within each of the 3 models for the parameter $J_0$ at each investigated field together with the data from magnetic measurements in the range 4 - 13 K.

On the other hand, by fitting with the Ginzburg Landau model, an almost constant and reasonable trend of values for the parameter $T_0$ at low fields is obtained, and this could give an indication regarding the pinning mechanisms below 2 T. The values obtained for the parameter $J_0$ within the 3 models are in all cases compatible with experimental data. The peak effect is in fact not only recovered by the phenomenological parameters $J_0$ at 0 K, but it appears to fall in the reasonable position, considering the trend found for this sample for the $H_{peak}$ versus T (see Figure 32). This last result is not-straightforward and thus encouraging.
Far from giving a definitive explanation, from this analysis it is possible to say that a pinning regime variation is expected not only as a function of the temperature, but also as a function of the magnetic field.

### 4.3.2.4 Relaxation magnetization

In this section we report a study of the vortex dynamics in sample FST970 performed by relaxation magnetization measurements over a period of time up to 7200 s. As a general trend, we observe a logarithmically decay of moment versus time (for times greater than 100 s), at both 0 T and 5 T. In a previous paragraph, when describing the relaxation measurements on sample FST970B, it was already given a short excursus regarding magnetic relaxation, its implications and some of the models that have been developed with the aim of explaining this phenomenon. In this case it is of course possible to proceed in the same way, but the results obtained will indicate a different behaviour of the vortex dynamic with respect to the other sample.

Assuming a thermal activation process over the flux creep activation barrier $U(M)$, the dynamical equation for $M$ can be solved with logarithmic accuracy, yielding $U(M) = k_BT\ln(t/t_0)$. Following the procedure proposed by Maley *et al.* [32] the plots of $k_BT[\ln|dM/dT|\text{-A}]$ versus $M$ at different temperatures can be used to reconstruct the

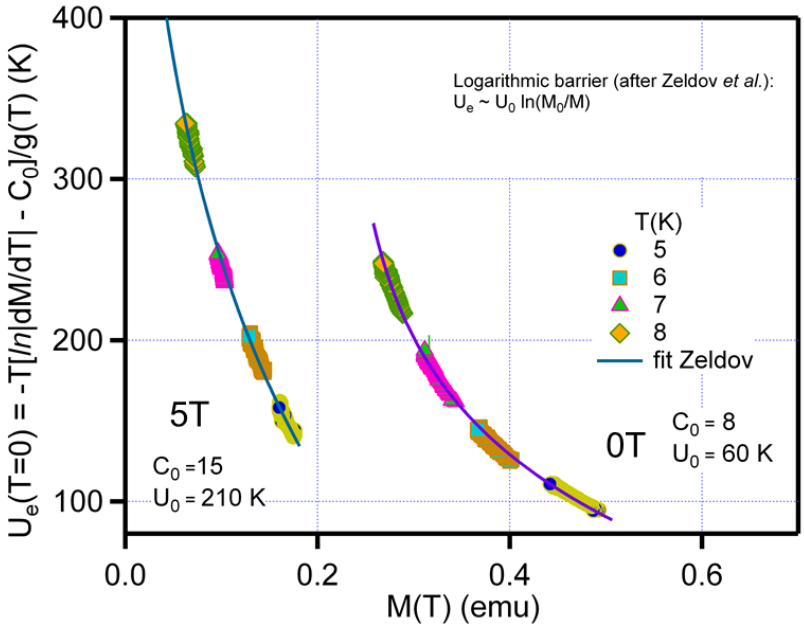


Figure 41: Magnetization dependence of the pinning potential Energy barrier height calculated in the frame of the Maley model, scaling the data at different temperatures for sample FST970. Scaled data are fitted by supposing a logarithmic dependence of the barrier upon magnetization.

dependence of the activation barrier $U$ upon $J$. We also assume the Tinkham approximation [34], where the $U(T,H)$ function can be factored into two contributions: $U(T,H) = U_0(H)g(t)$, where $g(t) = (1-t^2)(1-t^4)^{1/2}$, (with $t = T/T_c$ ). Our results are reported in Figure 41, scaled considering $C_0 = 15$ at zero field and $C_0 = 8$ at $\mu_0 H = 5$ T. The activation barrier is a monotonic function of $M$, and, as already done with data from sample FST970B, it is possible to fit these data with the logarithm dependence proposed by Zeldov *et al.* [35] both at zero field and at 5 T.

Data in Figure 41 have been fitted supposing $U = U_0 \ln(M_0/(M-\alpha))$. In the zero applied field case, we found $U_0 = 60$ K, whereas in the presence of a field of 5 T we found $U_0 = 210$ K. This result, that could seem in principle very strange, could be explained in the framework of the elastic vortex regime [30],[21], in which the interactions among vortices cannot be neglected and the energy of the activation barrier increases as the applied field increases. As anticipated in paragraph 4.3.2.2, we found that the analysis on relaxation magnetization support the existence of an elastic vortex regime below the $H_{peak}$ line in the phase diagram, and thus the vortex elastic-plastic regime transition is among the possible explanations for the peak effect in this sample [74].

## References


[1] Kubaschewski O. (1982) Iron-Binary Phase Diagrams Springer-Verlag Berlin Heidelberg GmbH.

[2] Lim E. H. H. *et al.* (2015) Synthesis of bulk $FeTe_{1-x}Se_x$ (x=0.1–0.5) at ambient pressure *J. Supercond. Nov. Mag.* 28, 2839-2845.

[3] Yeh K. W. *et al.* (2008) Tellurium substitution effect on superconductivity of the α-phase iron selenide *Europhys. Lett*. 84 37002.

[4] Fang M. H., Pham H. M., Qian B., Liu T. J., Vehstedt E. K., Liu Y., Spinu L. and Mao Z. Q. (2008) Superconductivity close to magnetic instability in $Fe(Se_{1-x}Te_x)_{0.82}$. *Phys. Rev. B* 78 224503.

[5] Mizuguchi Y., Tomioka F., Tsuda S., Yamaguchi T. and Y. Takano (2009) Enhancement of transition temperature in $Fe_xSe_{0.5}Te_{0.5}$ film via iron vacancies *J. Phys. Soc. Jpn*. 78 074712.

[6] Zhuang J. C.*et al.* (2014) Enhancement of transition temperature in $Fe_xSe_{0.5}Te_{0.5}$ film via iron vacancies *Appl. Phys. Lett*., vol. 104, 262601.

[7] Fiamozzi Zignani C. *et al.* (2017) Fabrication and physical properties of polycrystalline iron-chalcogenides superconductors, accepted for publication in *IEEE Trans. on Appl. Supercond*. 27 4.

[8] Hacisalihoglu M. Y. and Yanmaz E. (2013) Effect of substitution and heat treatment route on polycrystalline $FeSe_{0.5}Te_{0.5}$ superconductors *J. Supercond. Novel Magn.* 26, 2369–2374.

[9] Guler N. K. *et al.* (2014) The annealing effects in the iron-based superconductor $FeTe_{0.8}Se_{0.2}$ prepared by the self-flux method *J. Supercond. Nov. Magn*. 27, 2691-2697.

[10] Leo A.*et al.* (2015) Vortex pinning properties in Fe-chalcogenides *Supercond. Sci. Technol*. 28, 125001.

[11] Liu Y., Lin C. T. (2011) A comparative study of $Fe_{1+\delta}Te_{1-x}Se_x$ single crystals grown by Bridgman and self-flux techniques *J. Supercond. Nov. Magn*. 24, 183-187.

[12] Viennois A., Giannini E., van der Marel D., Cerny R. (2010) Effect of Fe excess on structural, magnetic and superconducting properties of single-crystaline $Fe_{1+x}Te_{1-y}Se_y$ *J. of Solid State Chem*. 183, 769-775.

[13] Palenzona A. *et al.* (2012) A new approach for improving global critical current density in $Fe(Se_{0.5}Te_{0.5})$ polycrystalline materials, *Supercond. Sci. Technol.* 25, Art. no. 115018.

[14] Chen N., Liu Y., Ma Z., Yu L., Li H. (2016) Improvement in structure and superconductivity of bulk $FeSe_{0.5}Te_{0.5}$ superconductors by optimizing sintering temperature *Scripta Materialia*, 112, 152-155.

[15] Bean C.S. P. (1964) Magnetization of High-Field Superconductors *Rev. Mod. Phys.* 36, 3.

[16] Bonura M., Giannini E., Viennois R., and Senatore C. (2012) Temperature and time scaling of the peak-effect vortex configuration in $FeTe_{0.7}Se_{0.3}$ *Phys. Rev. B*, 85, 134532.

[17]Galluzzi A., Polichetti M., Buchkov K., Nazarova E., Mancusi D., and Pace S. (2015) Evaluation of the intragrain critical current density in a multidomain FeSe crystal by means of dc magnetic measurements *Supercond. Sci. Technol*., 28, 115005.
[18]Onar K.and Yakinci M. E. (2015) Solid state synthesis and characterization of bulk β-FeSe superconductors *J. Alloys Compounds* 620,. 210–216.
[19]Dew-Hughes (1974) Flux pinning mechanisms in type II superconductors *Phil. Mag.* 30, 293.
[20] Huebener R.P. (1979) *Magnetic flux structures in superconductors* Springer.
[21]Blatter G., Feigel'man M.V. Geshkenbein V.B., Larkin A.I., Vinokur V.M., (1994) Vortices in high-temperature superconductors *Rev. Mod. Phys.* 66 1125.
[22]Kramer E. J. (1973) Scaling Laws for Flux Pinning in Hard Superconductors *J. of Appl. Phys.* 44(3), 1360-1370.
[23]Das P., Thakur A. D., Yadav A. K., Tomy C. V., Lees M. R., Balakrishnan G., Ramakrishan S. and Grover A. K. (2011) Magnetization hysteresis and time decay measurements in $FeSe_{0.50}Te_{0.50}$: Evidence for fluctuation in mean free path induced pinning *Phys. Rev. B* 84 214526.
[24]Shahbazi M., Wang X.L., Dou S.X., Fang H. and Lin C.T. (2013) The flux pinning mechanism, and electrical and magnetic anisotropy in $Fe_{1.04}Te_{0.6}Se_{0.4}$ superconducting single crystal *J. of Appl. Phys*. **113** 17E115.
[25]Griessen R., Hai-hu W., van Dalen A. J. J., Dam B., Rector J., Schnack H. G., Libbrecht S.., Osquiguil E, Bruynseraede (1994) Evidence for mean free path fluctuation induced pinning in $YBa_2Cu_3O_7$ and $YBa_2Cu_4O_8$ films *Phys. Rev. Lett*. **72** 1910.
[26]Küpfer H., Meier-Hirme,r R. and Reichert T. (1980) Field dependent change of the critical current density in neutron irradiated A 15 superconductors with grain boundary pinning *J. Appl. Phys.*, vol. 51, 1121.
[27]Baumgartner T., Eisterer M., Weber H. W., Flükiger R., Scheuerlein C. and Bottura L. (2014) Effects of neutron irradiation on pinning force scaling in state-of-the-art $Nb_3Sn$ wires, *Supercond. Sci. Technol.*, 27, 015005.
[28]Guarino A.*et al*. (2014) Pinning mechanism in electron-doped HTS Nd Ce CuO epitaxial films *Supercond. Sci. Technol*. 27, 124011.
[29]Mikitik G.P. and Brandt E.H. (2005) Vortex-Shaking Effect in Thin Flat Superconductors *J. Low Temp. Phys.* 139 221.
[30]Yeshurun Y., Malozemoff A.P. and Shaulov A. (1996) Magnetic relaxation in high-$T_c$ superconductors *Rev. Mod. Phys.* 68 3 911.
[31]Anderson P.W. and Kim Y.B. (1964) Hard Superconductivity: Theory of the Motion of Abrikosov Flux Lines *Rev. Mod. Phys.* 36 39.
[32]Maley M. P., and Willis J. O. (1990) Dependence of flux-creep activation energy upon current density in grain-aligned $YBa_2Cu_3O_{7-x}$, *Phys. Rew. B*, 42, no. 4.
[33]Beasley M.R., Labush R., Webb W.W. (1969) Flux Creep in Type-II Superconductors *Phys. Rev*. 181 682.
[34]Tinkham E. M. (1988) Resistive transition of High-Temperature Superconductors, *Phys. Rev. Lett.*, 61, no. 14.
[35]Zeldov *et al*. (1990) Flux-creep characteristics in high-temperature superconductors *Appl. Phys. Lett.*, vol. 56(7).
[36]Vinokur V.M., Fiegel'man M.V. and Geshkenbein V.B. (1991) Exact solution for flux creep with logarithmic *U*(*j*) dependence: Self-organized critical state in high-$T_c$ superconductors *Phys. Rev. Lett.* 67 915.
[37]Bellingeri E. *et al.* (2012) Strong vortex-pinning in $FeSe_{0.5}Te_{0.5}$ epitaxial thin film, *Appl. Phys. Lett.* 100 082601.
[38]Si W. *et al*. (2012) High current superconductivity in $FeSe_{0.5}Te_{0.5}$-coated conductors at 30 tesla, *Nat. Communicat*. 4:1347.
[39]Okamoto H. and Tanner L. E. (1990) *Binary Alloy Phase Diagrams* 2nd ed. edited by Massalski T B vol 2 (Materials Park Ohio: ASM International) pp 1781-83.
[40]Lortz R. *et al.* (2007) Origin of the magnetization peak effect in the $Nb_3Sn$ superconductor. *Phys. Rev. B* **75,** 094503.
[41]Klein L., Yacoby E. R., Yeshurun Y., Erb A., Müller-Vogt G., Breit V. and Wühl (1994) Peak effect and scaling of irreversible properties in untwinned Y-Ba-Cu-O crystals *Phys. Rev. B* **49** 6 4403.
[42]Abulafia Y. *et al.* (1996) Plastic Vortex Creep in $YBa_2Cu_3O_{7-x}$ Crystals. *Phys. Rev. Lett.* **77,** 1596.
[43]Yang, G *et al.*(1993) Competing pinning mechanisms in $Bi_2Sr_2CaCu_2O_y$ single crystals by magnetic and defect structural studies. *Phys. Rev. B* **48** 4054–4060.

[44]Pissas M. *et al.* (2002) Peak Effect in Single Crystal $MgB_2$ Superconductor for H//c-Axis. *Phys. Rev. Lett.* **89,** 097002.

[45]Prozorov R., Ni N., Tanatar M. A., Kogan V. G., Gordon R. T., Martin C, Blomberg E. C., Prommapan P., Yan J. Q., Bud'ko S. L. and Canfield P. C. (2008) Vortex phase diagram of $Ba(Fe_{0.93}Co_{0.07})_2As_2$ single crystals *Phys. Rev. B* **78** 224506.

[46]Senatore C. *et al.*(2008) Upper critical fields well above 100 T for the superconductor $SmFeAsO_{0.85}F_{0.15}$ with $T_c$ = 46 K. *Phys. Rev. B* **78,** 054514.

[47]Shen B. *et al.* (2010) Flux dynamics and vortex phase diagram in $Ba(Fe_{1-x}Co_x)_2As_2$ single crystals revealed by magnetization and its relaxation. *Phys. Rev. B* **81,** 014503.

[48]Yang H. *et al.* (2008) Fishtail effect and the vortex phase diagram of single crystal $Ba_{0.6}K_{0.4}Fe_2As_2$ *Appl. Phys. Lett.* **93,** 142506.

[49]Sun D. L. *et al.* (2009) Comparative study of upper critical field $H_{c2}$ and second magnetization peak $H_{sp}$ in hole- and electron-doped $BaFe_2As_2$ superconductor *Phys. Rev. B* **80,** 144515.

[50]Salem-Sugui, S. *et al.* (2010) Flux dynamics associated with the second magnetization peak in the iron pnictide $Ba_{1-x}K_xFe_2As_2$ *Phys. Rev. B* **82,** 054513.

[51]Pramanik A. K. *et al.* (2011) Fishtail effect and vortex dynamics in LiFeAs single crystals *Phys. Rev. B* **83,** 094502.

[52]Nishizaki T *et al.* (1998) Anomalous magnetization and field-driven disordering transition of a vortex lattice in untwinned $YBa_2Cu_3O_y$ *Phys. Rev. B* **58,** 11169.

[53]Rosenstein B. *et al.*(2005) Peak effect and square-to-rhombic vortex lattice transition in $La_{2-x}Sr_xCuO_4$ *Phys. Rev. B* **72,** 144512.

[54]Kopylov V. N. *et al.* (1990) The role of surface effects in magnetization of high-$T_c$ superconductors. *Physica C* **170,** 291.

[55]Prozorov R. *et al.* (2009) Intrinsic magnetic properties of the superconductor $NdFeAsO_{0.9}F_{0.1}$ from local and global measurements. *New J. Phys.* **11,** 035004.

[56]Pramanik A. K. et al. (2013) Flux dynamics and avalanches in the 122 pnictide superconductor $Ba_{0.65}Na_{0.35}Fe_2As_2$, *J. Phys.: Condens. Matter* 25 495701.

[57]Sun Y. *et al.* (2013) Magnetic relaxation and collective vortex creep in $FeTe_{0.6}Se_{0.4}$ single crystal EPL 103 57013 doi: 10.1209/0295-5075/103/57013.

[58]Miu D. *et al.* (2012) On the nature of the second magnetization peak in $FeSe_{1-x}Te_x$ single crystals. *Supercond. Sci. Technol*. **25,** 115009.

[59]Zhou W., Xing X., Wu W., Zhao H. and Shi Z. (2016) Second magnetization peak effect, vortex dynamics, and flux pinning in 112-type superconductor $Ca_{0.8}La_{0.2}Fe_{1-x}Co_xAs_2$ *Scientific Reports* 6:22278 *Nature* | DOI:10.1038/srep22278.

[60]Zhukov A. A., Küpfer H., Perkins G., Cohen L. F., Caplin A. D., Klestov S. A., Claus H., Voronkova V. I., Wolf T. and Wuhl H. (1995) Influence of oxygen stoichiometry on the irreversible magnetization and flux creep in $RBa_2Cu_3O_{7-\delta}$ ($R$=Y,Tm) single crystals *Phys. Rev. B* **51** 12704.

[61]Leo A. *et al.* (2014) Comparison of the pinning energy in $Fe(Se_{1-x}Te_x)$ compound between single crystals and thin films *Journal of Physics: Conference series* **507** 012029.

[62]Tanabe K. and Hosono H. (2012) Frontiers of Research on Iron-Based Superconductors toward Their Application *Japan J. Appl. Phys.* **51** 010005.

[63]Mazin I. I., Singh D. J., Johannes M. D. and Du M. H. (2008) Unconventional superconductivity with a sign reversal in the order parameter of $LaFeAsO_{1-x}F_x$. *Phys. Rev. Lett.* 101 057003.

[64]Paglione J. and Greene R. L. (2010) High-temperature superconductivity in iron-based materials. *Nature Physics* 6 645-658.

[65]Li M. *et al.* (2016) Superfluid density and microwave conductivity of FeSe superconductor: ultra-long-lived quasiparticles and extended s-wave gap energy *New J. Phys.* **18** 082001 doi:10.1088/1367-2630/18/8/082001.

[66]Hanaguri T. *et al.* (2010) Unconventional *s*-Wave Superconductivity in Fe(Se,Te) *Science* 328 474.

[67]Lin J.-Y. *et al.* (2011) Coexistence of isotropic and extended s-wave order parameters in FeSe as revealed by low temperature specific heat *Phys. Rev. B* **84** 220507(R).

[68]Bourgeois-Hope P. *et al.* (2016) Thermal conductivity of the Iron-based superconductor FeSe: Nodeless gap with a strong two-band character *Phys. Rev. Lett.* **117** 097003.

[69]Civale L., McElfresh M. W., Marwick A. D., Holtzberg F. and Field C. (1991) Scaling of the Hysterestic magnetic behavior in $YBa_2Cu_3O_7$ single crystal *Phys. Rev. B* **43** 16 13732.

[70]Liu Y., Kremer K., Liu C.T. Superconductivity and vortex pinning in $Fe_{1.04}Te_{0.60}Se_{0.40}$ single crystal (2010) *Euro. Phys. Lett.* 92 57004.
[71]Yeshurun Y. and Malozemoff A.P. (1988) Giant flux creep and irreversibility in an Y-Ba-Cu-O-Crystal: an alternative to the superconducting glass model *Phys. Rev. Lett.* **60** 21 2202.
[72]Larkin A.I and Ovchinnikov Y.N. (1979) Pinning in type II superconductors *J. of Low Temp. Phys*. **34** 3/4.
[73]Di Gioacchino D., Celani F., Tripodi P., Testa A.M. and Pace S. (1999) Nonuniversal temperature dependencies of the low-frequency ac magnetic susceptibility in high-$T_c$ superconductors *Phys. Rev. B* **59** 17 11539.
[74]Fiamozzi Zignani C. *et al.* (2017) Manufacture and characterization of polycrystalline FeSeTe with peak-effect vortex configuration, *manuscript in preparation*.

# Conclusions

Present high field applications of superconducting materials are mainly based on low-$T_c$ NbTi and $Nb_3Sn$ superconductors, limiting the maximum field to 20T. High-$T_c$ superconductors like cuprates have an enormous potential in high-field applications, but they still present significant practical drawbacks for their commercial diffusion and use. Indeed as an example for YBCO, high anisotropy, large effect of grain misorientations, brittleness lead to high costs of production. Thus there is a great interest to explore other materials suitable for high field applications. In this framework, newly discovered Fe-Based Superconductors (IBSC) are a very promising option, especially due to their intermediate critical temperature and extremely high upper critical fields.
The discovery of different classes of IBSC in 2008 offered to the scientific community the opportunity to learn more on superconductivity in high-$T_c$ materials, and renewed the enthusiasm in all the fields related to superconductivity. However, neither at the Physics Department of University of Salerno, neither at ENEA CR Frascati, IBSC sample preparation had ever been faced before.
In this framework, the efforts of this Thesis have been the starting of a new research line mainly devoted to the preparation and to the study of the superconducting properties of Fe-Chalcogenides samples (FeSe and FeSeTe). The iron-chalcogenides family has been chosen mostly because of its interesting superconducting properties and also due to its simple crystalline structure and to the lack of poisonous elements in its composition.
These efforts led to the production of several Fe-Chalcogenides samples by means of different preparation techniques. Some of these techniques gave interesting results, other deserve further optimization in the near future. As expected, pinning properties strongly depend on the preparation procedures. Structural characterizations have indeed revealed the influence of the preparation procedure on the materials properties and their superconductive behaviour.

Regarding FeSe, two methods of samples fabrication have been prepared. The work started with the development of FeSe electrochemical deposition on iron substrate at ENEA, following the route developed by D. Demura in Japan, due to the cheapness of the process which makes it promising for a large scale production. The preparation has been in principle successful, but, despite the superconducting $\beta$-phase has been obtained, the optimization of superconducting parameters of the samples synthesized with this technique is very complex. The trade-off between costs (time consuming) and advantages (in terms of process economy) is not favourable, and thus this process revealed to be not attractive anymore.
I also implemented the solid state synthesis of polycrystalline FeSe, which led to the development of superconducting samples, although not yet optimized. These samples in fact contain the superconducting tetragonal $\beta$-phase, together with the secondary hexagonal $\delta$-phase and some impurities, and show a good superconducting onset but broad transitions, interpreted as a sign of inhomogeneity due to oxygen contamination. It was verified that an important issue is the FeSe critical sensibility to perfect stoichiometry, which can be easily compromised by the presence of impurities. This route of samples preparation could be improved taking care of process cleanliness but it would imply an infrastructure investment of a glove box to

control the oxygen and the humidity contamination. The disadvantage is to prevent the eventual scalability of the process to larger scale than the laboratory one.
Concerning FeSeTe samples, the mechano-chemical synthesis and the solid state reaction, both led to the preparation of several polycrystalline samples. These routes are both interesting and promising for superconducting FeSeTe production, that deserve to be exploited and improved in view of a $T_c$ optimization. Again, samples contamination, especially due to oxygen, seems to prevent good current transport properties.
Finally, the best performing FeSeTe samples were prepared by melting process, with HT at temperatures of about 970 °C followed by a slow cooldown to about 400 °C.
It was verified that the fusion process and the cooldown to the solid state remove impurities and spurious phases between grains and promote the preferential orientation of the samples and the pinning efficiency. Among the others, this fabrication route is therefore recommended in view of applications, even if further efforts are needed to develop a material which could be ready to use for example as a target for films deposition or eventually for the preparation of strands.
Despite the undeniable polycrystalline nature of the prepared FeSeTe samples, those obtained by melting present superconducting properties that closely resemble those of single crystals, with onset temperatures of about 15 K and quite steep transitions. These samples show large magnetic hysteresis cycles well opened up to 12 T (at about 9 K) and up to 18 T (at about 7 K) with high field current density only weakly dependent on the applied field.
As expected, pinning properties strongly depend on the preparation procedures. Structural characterizations have indeed revealed the influence of the preparation procedure on the materials properties and superconductive behaviour.
In particular, the best performing samples were compared through an extensive characterization. Beside the good homogeneity and the weak dependence of $J_c$ on applied magnetic field showed by all samples, sample FST970B, $Fe_{1.05}Se_{0.44}Te_{0.56}$, presents clearly a stronger pinning and enhanced superconducting properties with respect to the sample FST800, $Fe_{1.03}Se_{0.41}Te_{0.59}$. This is probably due to the most ordered and cleaner microstructure determined by melting, as evidenced by XRD and SEM analysis. Regarding sample FST970 $Fe_{1.07}Se_{0.37}Te_{0.63}$, grown with a similar HT as sample FST970B but with a faster cooldown, it shows in principle stronger pinning forces at low fields, but presents a second peak in the magnetization loop in the mixed state. Its behaviour has been analysed in the frame of the existing literature, trying to give a possible explanation and to draw a phase diagram of the sample under investigation. It was verified that these differences among the presented samples are not just sample-to-sample variations, but are due to the different fabrication processes. The role of the Fe excess, with large magnetic moment, is still an open question, yet to be clarified, addressing the more fundamental issue of the interplay between magnetism and superconductivity.
Beside magnetic, transport and calorimetric measurements, several analysis concerning the pinning mechanisms have been performed, in the frame of the Dew-Hughes and of the Griessen models. Coherently with literature, these FeSeTe samples seem to be mainly characterized by $\delta l$-pinning, even if several considerations have been made regarding the possible presence of other mechanisms or the presence of more than one type of pinning centres. Indeed the not perfect scaling of the reduced

| Sample | Preparation route | XRD phases | SEM analysis | $T_c$ onset (K) | $J_c$ (A/cm$^2$) | Results or conclusions |
|---|---|---|---|---|---|---|
| FeSe films #1, #2, #3, #4 | Electro-chemical deposition | $\beta$-FeSe | - | - | - | - |
| FeSe 2HT | 2 steps solid state synthesis | $\beta$-FeSe, $\delta$-FeSe, impurities | Disconnected grains: 1–3 $\mu$m | ~11 | - | - |
| FeSe 3HT | 2 steps solid state synthesis | $\beta$-FeSe, $\delta$-FeSe, impurities | Most of sample is homogeneous, grains: 200–300 nm | ~12 | - | - |
| FST550 | Solid state synthesis at 550 °C | $\beta$-phase, $\delta$-phase, iron-oxides | Uneven disconnected surface | ~14 | - | Inefficient pinning |
| FST650 | steps solid state synthesis (550 °C – 650 °C) | $\beta$-phase, $\delta$-phase, iron-oxides | Uneven disconnected surface | ~13 | - | Inefficient pinning |
| FST750 | 2 steps solid state synthesis (550 °C – 750 °C) | $\beta$-phase, $\delta$-phase, iron-oxides | Uneven disconnected surface | ~15 | - | Inefficient pinning |
| HEBM10 | Mechano-chemical synthesis | $\beta$-Fe(Se,Te), $Fe_7(Se,Te)_8$ | Amorphous aspect, grains: tens nm | - | - | - |
| HEBM10-700 | Mechano-chemical synthesis + HT 700 °C | $\beta$-Fe(Se,Te), $Fe_7(Se,Te)_8$ | Disconnected grains: 1–3 $\mu$m | ~6 | - | - |
| FST800 | 2 steps solid state synthesis (550 °C – 800 °C) | $\beta$-phase, impurities $Fe_{1.03}Se_{0.41}Te_{0.59}$ preferential orientation along *c*-axis | Terraced like, grains: 70 μm x 60 μm | ~15 | ~1.3 ·10$^3$ @ 4.2 K 0 T | Pinning changing in *T*: combination of $\delta T_c$ and $\delta l$ weak pinning (point pins) |
| FST970 | 2 steps: 550 °C and melting with 30 °C/h cooldown ramp | $\beta$-phase $Fe_{1.07}Se_{0.37}Te_{0.63}$ preferential orientation along *c*-axis | Terraced like, grains: 250 μm x 150 μm | ~15 | ~5 ·10$^3$ @ 4.2 K 0 T | Pinning changing in *B* and in *T*: PEAK EFFECT and elastic regime below the $H_{peak}$ line |
| FST970B | 2 steps: 550 °C and melting with 10 °C/h cooldown ramp | $\beta$-phase $Fe_{1.05}Se_{0.44}Te_{0.56}$ preferential orientation along *c*-axis | Terraced like, grains: 250 μm x 150 μm | ~15.2 | ~2.6 ·10$^3$ @ 4.2 K 0 T | predominance of $\delta l$ weak pinning (point pins) – single vortex up to 5 T |

Table C-1: sketch of the main results obtained for each preparation route.

pinning forces $f_p(h)$ at different temperatures versus the reduced magnetic field opens a discussion on the pinning mechanisms acting in these samples. The sensitivity of the

$f_p(h)$ to microstructural variables confirms the better results given by the heat treatment at 970°C which lead to higher $J_c$ and to more efficient pinning, which moves from weak pinning, in sample FST800, to stronger pinning in sample FST970B.

Magnetic relaxation measurements have supported this analysis giving a corroborating possible interpretation of the measured peak effect in terms of a crossover from elastic to plastic regime (E-P crossover) for sample FST970. On the other hand, the logarithmic dependence of the pinning energy barrier $U$ upon $M$, extrapolated from magnetic relaxation measurements for samples FST970B, is a good approximation for the creep activation barrier in the single vortex creep regime. Therefore our results indicate that in this sample the motion of flux lines develops in the single-vortex pinning limit even in magnetic fields up to 5 T, which means that inter-vortex interactions, typical of collective pinning theories, can be neglected. This result confirms that this material has a high application potential, as, when optimized, it will be capable of carrying high current densities up to high magnetic fields.

In Table C-1 a sketch of the main results obtained for each group of samples is reported, that is for each preparation route that has been followed during this work of thesis.

In summary, the results achieved during my Ph.D. work might turn to be a step toward the simple and economic fabrication of iron-chalcogenides samples with good superconducting properties.

# Appendix 1: High Energy Ball Milling (HEBM)

The High Energy Ball Milling (HEBM) technology consists in exposing definite quantities of powders to the repeated action of hitting balls, properly launched by a milling device. The energy transfer events that occur from the balls to the trapped powder can promote different phenomena. Breaking the original grains into smaller ones reduces particles dimensions. At microscopic level particles breakdown is generally accompanied by enhanced powder reactivity. Due to the breakdown of polycrystalline particles into smaller grains, a gradual growth of the surface area occurs. Crystallite size becomes smaller and the new clean surfaces created by the milling action can interact each other. Powder particles progressively accumulates defects and germs of different phases can enucleate at grain boundaries. Chemical reactions between different reactants can be activated at the phase boundaries and new products appear at the contact interfaces between the starting compounds. Finally growth of previously enucleated products occurs and a light reduction in surface area is observed [1]. The phenomenology of the different actions induced by HEBM treatment on powder particles at different milling stages is sketched in Figure A1.

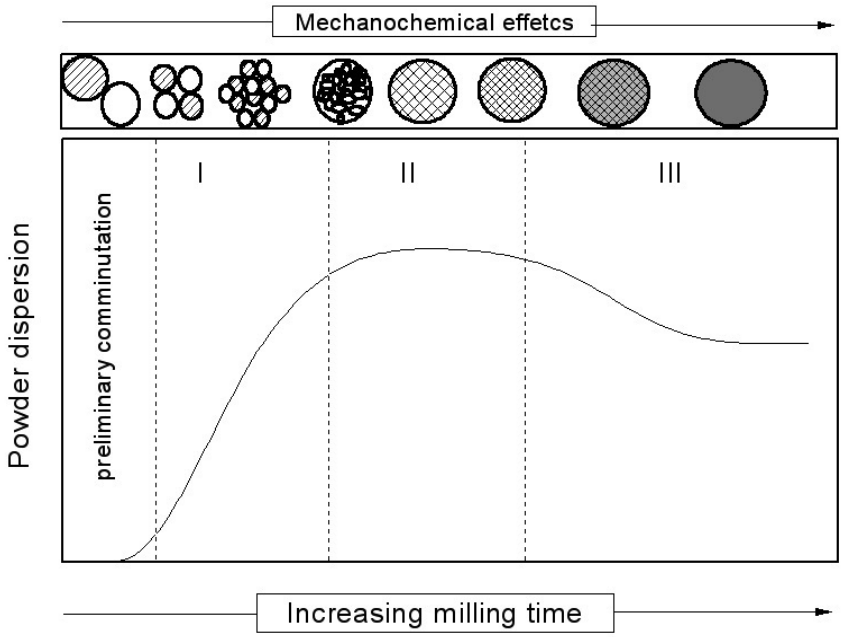


Figure A1: Different stages of powder activation during a high-energy ball milling treatment.

## References

[1] Pentimalli M., Bellusci M and Padella F. (2015) Handbook of Mechanical Nanostructuring – Chapter 28: High-Energy ball milling as a general tool for nanomaterials synthesis and processing, *Wiley-VCH Verlag GmbH &Co. KGaA.*

# Articles and conferences communications related to the work of this thesis

## Articles

C. Fiamozzi Zignani, V. Corato, A. Leo, G. De Marzi, A. Mancini, Y. Takano, A. Yamashita, M. Polichetti, A. Galluzzi, A. Rufoloni, G. Grimaldi, and S. Pace, "**Fabrication and characterization of sintered iron-chalcogenides superconductors**", *IEEE Trans. on Appl. Supercond.* vol. 26 no. 3 (2016).

C. Fiamozzi Zignani, G. De Marzi, G. Grimaldi, A. Leo, A. Guarino, A. Vannozzi, A. della Corte, and S. Pace, "**Fabrication and physical properties of polycrystalline iron-chalcogenides superconductors**", *IEEE Trans. on Appl. Supercond.* vol. 27 no. 4 (2017).

C. Fiamozzi Zignani, G. De Marzi, G. Grimaldi, V. Corato, A. Galluzzi, A. Mancini, A. Leo, A. Vannozzi, A. Guarino, A. Rufoloni, M. Polichetti, A. della Corte and S. Pace, "**Manufacture and characterization of polycrystalline FeSeTe with peak-effect vortex configuration**", in preparation.

## Conferences

**European Conference on Applied Superconductivity (EUCAS)**, 6-10 September 2015, Lione, France – Poster: "*Fabrication and characterization of sintered iron-chalcogenides superconductors"* C. Fiamozzi Zignani, V. Corato, A. Leo, G. De Marzi, A. Mancini, Y. Takano, A. Yamashita, P. Manfrinetti, A. Provino, A. Sala, M. Polichetti, A. Galluzzi, A. Rufoloni, G. Grimaldi, and S. Pace.

**Applied Superconductivity Conference (ASC)**, 4-9 September 2016, Denver, Colorado Convention Center, US. – Poster: *"Fabrication and physical properties of polycrystalline iron-chalcogenides superconductors"* C. Fiamozzi Zignani, G. De Marzi, G. Grimaldi, A. Leo, A. Guarino, A. Vannozzi, A. della Corte, and S. Pace.

**Third Conference on Superconductivity and Functional Oxides (SuperFOx)** 19-21 September, 2016, Torino, Italy – Oral Presentation: *"Mechanochemical assisted synthesis of* $FeSe_xTe_{1-x}$ *material: a structural and thermoanalytical study"* A. Masi, C. Alvani, M. Carlini, G. Celentano, G. De Marzi, A. La Barbera, F. Fabbri, F. Padella, M. Pentimalli, A. Vannozzi, C. Fiamozzi Zignani.

# Acknowledgments

I would like to acknowledge first of all my supervisors, Dr. Gaia Grimaldi and Prof. Sandro Pace for stimulating my interest during these years, for their confident and positive attitude and for transmitting me part of their skills with useful discussions regarding several measurements and analysis on superconducting aspects of the prepared samples. Beside them, I acknowledge Prof. Massimiliano Polichetti, Dr. Antonio Leo, Dr. Anita Guarino and Armando Galluzzi for their collaboration in measurements activities related to this work at Salerno University.

Of course I acknowledge my boss at ENEA Superconductivity Laboratories, Ing. Antonio della Corte, for supporting me when needed especially supplying the necessary instrumentations and facilities and leaving me the freedom to organize my research and my work.

I acknowledge my colleagues from the Superconductivity Laboratories, and in particular Gianluca De Marzi e Valentina Corato for their collaboration in the measurements activities related to this work and for the useful discussions that come out during the research activities.

I also thank the colleagues from ENEA C.R. Casaccia, in particular Andrea Masi, Franco Padella, Aurelio La Barbera , Fabio Fabbri and Carlo Alvani for their support in the part of the work related to the mechano-chemical synthesis of FeSeTe compounds.

I acknowledge my family, that gave me sustain and support during these years and all my friends which showed patience and encouraged me all the times. Finally I acknowledge my partner, Giuseppe, that sustained me since the very beginning of this adventure and furthermore is now bringing me into another adventure: without him all this would not have been possible.